UNIVERSITY OF WEST ATTICA

FACULTY OF ENGINEERING

DEPARTMENT OF ELECTRICAL & ELECTRONICS ENGINEERING

Diploma Thesis

"Monitoring the strains on cadaveric femoral bones with titanium alloy prosthetic stems"

Student : MANDAKAKIS ARTEMIOS

Registration number: 18387260

Supervisor

Konstantinos Kalkanis

Assistant Professor

ATHENS-EGALEO, JULY, 2024

ΠΑΝΕΠΙΣΤΗΜΙΟ ΔΥΤΙΚΗΣ ΑΤΤΙΚΗΣ

ΣΧΟΛΗ ΜΗΧΑΝΙΚΩΝ

ΤΜΗΜΑ ΗΛΕΚΤΡΟΛΟΓΩΝ & ΗΛΕΚΤΡΟΝΙΚΩΝ ΜΗΧΑΝΙΚΩΝ

Διπλωματική Εργασία

«Παρακολούθηση Καταπονήσεων σε Πτωματικά Μηριαία Οστα με Προσθετικά Στελέχη από Κράματα Τιτανίου»

Φοιτητής : ΜΑΝΔΑΚΑΚΗΣ ΑΡΤΕΜΙΟΣ

ΑΜ : 18387260

Επιβλέπων Καθηγητής

Κωνσταντίνος Καλκάνης

Επίκουρος Καθηγητής

ΑΘΗΝΑ ΑΙΓΑΛΕΩ, ΙΟΥΛΙΟΣ , 2024

The Diploma Thesis was accepted and graded by the following three-member committee :

Kalkanis Konstantinos, Assistant Professor	Stavrakas Ilias, Professor	Ioannidis Georgios, Professor
(Signature)	(Signature)	(Signature)

AUTHORS STATEMENT

The undersigned Mandakakis Artemios, with registration number 18387260, student of the University of West Attica, Department of Electrical and Electronics Engineering,
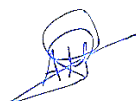
I declare responsibly that :

"I am the author of this Diploma Thesis and any help I have had in preparing it is fully recognized and refers to the thesis. Also, any sources from which I used data, ideas, or words, whether exactly or paraphrased, are listed in their entirety, with full reference to the authors, publishing house, or magazine, including any sources that may have been used from the internet. I also confirm that this work has been written by me exclusively and is the intellectual property of both myself and the Foundation.

Violation of my above academic responsibility is an essential reason for the revocation of my diploma.

I wish to deny access to the full text of my work until ………………….. and upon my application to the Library and the approval of the supervising professor.

The Declarant

Mandakakis Artemios

(signature)

ΔΗΛΩΣΗ ΣΥΓΓΡΑΦΕΑ ΔΙΠΛΩΜΑΤΙΚΗΣ ΕΡΓΑΣΙΑΣ

Ο κάτωθι υπογεγραμμένος Μανδακάκης Αρτέμιος του Στυλιανού, με αριθμό μητρώου 18387260 φοιτητής του Πανεπιστημίου Δυτικής Αττικής της Σχολής ΜΗΧΑΝΙΚΩΝ του Τμήματος ΗΛΕΚΤΡΟΛΟΓΩΝ ΚΑΙ ΗΛΕΚΤΡΟΝΙΚΩΝ ΜΗΧΑΝΙΚΩΝ,

δηλώνω υπεύθυνα ότι:

«Είμαι συγγραφέας αυτής της διπλωματικής εργασίας και ότι κάθε βοήθεια την οποία είχα για την προετοιμασία της είναι πλήρως αναγνωρισμένη και αναφέρεται στην εργασία. Επίσης, οι όποιες πηγές από τις οποίες έκανα χρήση δεδομένων, ιδεών ή λέξεων, είτε ακριβώς είτε παραφρασμένες, αναφέρονται στο σύνολό τους, με πλήρη αναφορά στους συγγραφείς, τον εκδοτικό οίκο ή το περιοδικό, συμπεριλαμβανομένων και των πηγών που ενδεχομένως χρησιμοποιήθηκαν από το διαδίκτυο. Επίσης, βεβαιώνω ότι αυτή η εργασία έχει συγγραφεί από μένα αποκλειστικά και αποτελεί προϊόν πνευματικής ιδιοκτησίας τόσο δικής μου, όσο και του Ιδρύματος.

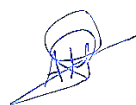Παράβαση της ανωτέρω ακαδημαϊκής μου ευθύνης αποτελεί ουσιώδη λόγο για την ανάκληση του διπλώματός μου.

Επιθυμώ την απαγόρευση πρόσβασης στο πλήρες κείμενο της εργασίας μου μέχρι ……………………… και έπειτα από αίτησή μου στη Βιβλιοθήκη και έγκριση του επιβλέποντος/ουσας καθηγητή/ήτριας.»

<div align="center">

Ο/Η Δηλών/ούσα

(Ονοματεπώνυμο φοιτητή/ήτριας)

Μανδακάκης Αρτέμιος

(Υπογραφή φοιτητή/ήτριας)

</div>

<u>Acknowledgements</u>

At this point, I would like to warmly thank the people who supported me in this great effort to complete this research. First, I want to special thank my parents, who raised and ma cared for me with love, allowing me to reach this important point in my life. What they have offered me and continue to offer me cannot be described in words and certainly, without them, I would not been able to reach my goal. A big thank you is also due to my fellow students, who were always by my side in all difficult and good times. Finally, I would like to express my appreciation to the professors and external collaborators of my university, 3Ψ and Akmelogi S.m.p.c., who guided me and equipped me with the necessary equipment for the successful completion of my dissertation. My goal for the near future is to continue this path and make the aforementioned individuals proud.

ΕΥΧΑΡΙΣΤΙΕΣ

Σε αυτό το σημείο θα ήθελα να ευχαριστήσω θερμά τα άτομα που με στήριξαν στη μεγάλη αυτή προσπάθεια για την ολοκλήρωση της παρούσας έρευνας. Αρχικά, θέλω να ευχαριστήσω τους γονείς μου, οι οποίο με μεγάλωσαν και με φρόντισαν με αγάπη, επιτρέποντάς μου να φτάσω σε αυτό το σημαντικό σημείο της ζωής μου. Αυτά που μου έχουν προσφέρει και συνεχίζουν να μου προσφέρουν δεν μπορούν να περιγραφούν με λόγια και σίγουρα χωρίς αυτά δεν θα είχα καταφέρει να φτάσω στο στόχο μου. Ένα μεγάλο ευχαριστώ αξίζει και στους συμφοιτητές μου, οι οποίοι ήταν πάντα δίπλα μου σε όλες τις δύσκολες και καλές στιγμές. Τέλος, θα ήθελα να εκφράσω την εκτίμησή μου στους καθηγητές και τους εξωτερικούς συνεργάτες του πανεπιστημίου μου, την 3Ψ και την Akmelogi S.m.p.c., οι οποίοι με καθοδήγησαν και με εξόπλισαν με τον απαραίτητο εξοπλισμό για την επιτυχή ολοκλήρωση της διπλωματικής μου εργασίας. Στόχος μου για κοντινό μέλλον είναι να συνεχίσω αυτήν την πορεία και να κάνω υπερήφανα τα προαναφερθέντα άτομα.

ABSTRACT

The present work involved the mechanical properties evaluation of cadaveric specimens with titanium prosthetic stems by monitoring the strains in a realistic simulated environment of human joint forces. The results of this work can be used to understand the behavior of bone tissue and improve the design of the hip implants, enhancing quality of life for patients suffering from diseases and injuries. The literature survey part of the research referenced multiple scientific fields crucial for its completion, including the historical context of THA, the evolution of contemporary THA, hip biomechanics, the mechanical properties and the behavior of bone tissue and biomaterials, additive manufacturing techniques for the construction of patient-specific implants, and the biomechanical sensors and optical techniques that provide strain distribution and displacement data for the implant-bone system. The experimental phase was divided into two main parts: designing and constructing a mechanical system capable of accurately replicating the forces acting on the hip joint, and the mechanical evaluation of two cadaver human femurs, one intact and one implanted with a titanium alloy prosthetic stem. A Digital Image Correlation (DIC) system was used to capture the strains of the cadaver specimens in two different planes. The intact femur reached the maximum load in all five attempts, exhibiting a linear behavior. The DIC results indicated that the highest strain concentrations are in the medial diaphysis and in the femoral neck. These results were consistent with other studies referenced in the theoretical part of this work. The implanted femur did not reach the maximum load because it was damaged by the polymerization of PMMA at the great trochanter. With only limited data collected, the implant-bone system showed linear behavior during the loading, a similar behavior that was detected for the intact femur, however, this data is insufficient to evaluate implant integrity. Future research should focus on improving both experimental design and methodology utilising the challenges and limitations encountered in this work.

KEYWORDS

ΠΕΡΙΛΗΨΗ

Η παρούσα εργασία περιλαμβάνει την αξιολόγηση των μηχανικών ιδιοτήτων πτωματικών μηριαίων οστών με προσθετικά στελέχη από κράματα τιτανίου παρακολουθώντας τις παραμορφώσεις τους υπο πίεση/μηχανική τάση σε ένα ρεαλιστικό περιβάλλον προσομοιώσης των δυνάμεων που ασκούνται στο ισχίο. Τα αποτελέσματα της παρούσας δουλειάς μπορούν να χρησιμοποιηθούν για την κατανόηση της συμπεριφοράς του οστικού ιστού και τη βελτίωση του σχεδιασμού των εμφυτευμάτων ισχίου, βελτιώνοντας παράλληλα την ποιότητα ζωής των ασθενών που πάσχουν από ασθένειες και τραυματισμούς στο ισχίο. Το θεωρητικό μέρος της έρευνας αφορά πολλαπλά επιστημονικά πεδία κρίσιμα για την ολοκλήρωσή της. Συγκεκριμένα γίνεται αναφορά στο ιστορικό πλαίσιο και στην εξέλιξη της σύγχρονης ολικής αρθροπλαστικής ισχίου, στην εμβιομηχανική του ισχίου, στις μηχανικών ιδιότητες και την συμπεριφορά του οστικού ιστού και των σύγχρονων βιοϋλικών, στους τρόπους κατασκευής των ειδικά προσαρμοσμένων εμφυτευμάτων για τον ασθενή και στους εμβιομηχανικούς αισθητήρες και οπτικών τεχνικών που παρέχουν δεδομένα για τις κατανομές των παραμορφώσεων και των μετατοπίσεων του οστού και εμφυτεύματος. Η πειραματική φάση χωρίστηκε σε δύο κύρια μέρη: το σχεδιασμό και την κατασκευή ενός μηχανικού συστήματος ικανού να αναπαράγει με ακρίβει τις δυνάμεις που δρουν στην άρθρωση του ισχίου και τη μηχανική αξιολόγηση δύο πτωματικών ανθρώπινων μηριαίων οστών, ενός άθικτου και ενός εμφυτευμένου. Χρησιμοποιώντας ένα σύστημα Ψηφιακής Συσχέτισης Εικόνας καταγράφηκαν οι παραμορφώσεις των δοκιμίων σε δύο διαφορετικά επίπεδα. Το άθικτο μηριαίο οστό έφτασε στο μέγιστο φορτίο και στις πέντε προσπάθειες, δείχνοντας γραμμική συμπεριφορά κατά τη φόρτιση. Τα αποτελέσματα του συστήματος ψηφιακής συσχέτισης εικόνας έδειξαν ότι οι υψηλότερες συγκεντρώσεις καταπόνησης ήταν στην έσω διάφυση και στον αυχένα του μηριαίου οστού. Αυτά τα αποτελέσματα ήταν σύμφωνα με άλλες μελέτες που αναφέρονται στο θεωρητικό μέρος αυτής της εργασίας. Το εμφυτευμένο μηριαίο οστό δεν έφτασε στο μέγιστο φορτίο επειδή υπέστη ζημιά από τον πολυμερισμό του ιατρικού τσιμέντου στον μείζονα τροχαντήρα. Με τα περιορισμένα μόνο δεδομένα που συλλέχθηκαν, το σύστημα οστό-εμφύτευμα επέδειξε γραμμική συμπεριφορά κατά τη φόρτωση. Ωστόσο, αυτά τα δεδομένα είναι ανεπαρκή για την αξιολόγηση της ακεραιότητας του εμφυτεύματος. Μελλοντικές έρευνες πάνω σε αυτό το κομμάτι θα πρέπει να επικεντρωθούν στη βελτίωση του πειραματικού σχεδιασμού και της

μεθοδολογίας, αντιμετωπίζοντας τις προκλήσεις και τους περιορισμούς που συναντήθηκαν σε αυτό το έργο.

ΛΕΞΕΙΣ ΚΛΕΙΔΙΑ

Παραμορφώσεις, Πτωματικά Μηριαία Οστά, Στελέχη από Κράματα Τιτανίου, Σύστημα Μεταφοράς Φορτίων, Σύστημα Ψηφιακής Συσχέτισης Εικόνας, Εμβιομηχανικοί Αισθητήρες.

Περιεχόμενα

LIST OF TABLES

LIST OF IMAGES

INTRODUCTION

Monitoring the strains on cadaveric femurs with titanium alloys prosthetic stems is a highly complex and demanding process. It requires intense focus, thorough preparation, knowledge from various scientific fields, and correct implementation of the proper equipment. The insights gained from this process are necessary for understanding the mechanical properties of both bone tissue and implants, leading to the design and production of improved implants. Additionally, it aids in developing new surgical techniques that are faster and more reliable. The advancement of implants and surgical methods enhances the success rate of total hip arthroplasty, improving the quality of life for individuals suffering from conditions like osteoarthritis or hip injuries.

Subject and Purpose

In this study, the strains of two cadaveric specimens - one intact and one implanted - will be monitored by creating a realistic environment that includes the main forces acting on a two-dimensional front plane of the hip. These forces are the body force, the abductor force, and the joint reaction force. The simulation of the forces will be accomplished by constructing a mechanical system capable of replicating them with high precision. A DIC system will be used to capture the displacements of the femur and produce the strain fields. These strain fields will help identify the mechanical properties of the bone tissue and evaluate implant integrity .

Methodology and Structure

The present study is divided into two parts. In the first part, which is also the theoretical part of the present work, some scientific fields will be addressed, which are important to understand for the correct conduct of the experimental part. The theoretical part includes four chapters that focus on total hip arthroplasty, the biomechanics of the human hip, the design and manufacture of suitable implants with good mechanical properties, and the analysis of biomechanical sensors and optical methods for biomechanical applications. Once these foundation topics are comprehended, the experimental process begins. Initially, the design, construction, and performance testing of a mechanical system capable of accurately simulating the main forces that develop in the hip joint will be carried out. Subsequently, cadaveric specimens will be prepared and subjected to loads to record developing strains. Finally, the measurements captured will be compared with other studies to evaluate the constructed system, assess the implant, and understand the behavior of the bone tissue.

1. TOTAL HIP ARTHROPLASTY

Total hip arthroplasty (THA) or total hip replacement (THR) is an operating procedure in which a prosthetic implant is used to replace the hip joint due to its dysfunction caused by various factors such as diseases and injuries (osteoarthritis, avascular necrosis of the femoral head, fractures of the femoral, etc). It has been developed to relieve patients from pain, improve their mobility and quality of life, and restore the functionality of worn-out joints [1],[2]. To put it another way, total hip arthroplasty attempts to give the patient a joint that works normally, resists dislocation, retains as much bone, and lasts as long as possible [1]. It is also considered to be one of the most successful and popular operative techniques in orthopedic surgery [2], [3], [4]. However, despite the benefits that follow the THA surgery, it is not always the first option in case of a dysfunctional hip joint, it is typically performed after other therapeutic options have failed to produce the intended results [1]. An example of the outcome of this operation is shown in Figure 1, where the right hip (left of image) has been replaced with a prosthetic implant.

*Figure 1: **Postoperative radiograph showing the replacement of the right hip (left of image) with a prosthetic implant. This X-ray was taken after correcting the vertical cup positioning [5].***

1.1 Chronology

The objectives and methods for implementing total hip arthroplasty began to take shape hundreds of years ago and they keep changing and evolving even today. Many historical events narrate the first attempts at improving the quality of life of patients who had a non-functional hip joint using primary techniques of THA. In the following paragraphs, the primary techniques of THA are presented also mentioning a number of important researchers who contributed to the success of THA nowadays. By today's standards, many people could say that their effort was a gift to humanity.

1.1.1 Early Techniques for a Dysfunctional Hip

One of the early techniques for a non-functional hip was resection arthroplasty also called excision arthroplasty. It is a type of surgery where small parts of the hip joint are removed due to painful fractures or infections. This method aims to eliminate infections and decrease pain in patients [1], [6].

In 1768 at the Westminster Hospital of London, Charles White (Figure 2) attempted a surgical excision on a patient who suffered from hip osteomyelitis by removing the femoral head. Taking into consideration the technology and the means at that time, plus the complexity of this operation, it could be said that he had exceptional medical knowledge and skills. Although his technique was primitive by today's standards, he demonstrated that hip surgery was a feasible goal, and his excision was an early attempt to produce a new hip joint in a patient, an early hip arthroplasty without implants [3].

In 1888 specific techniques that included the replacement of the femoral head and acetabulum were presented by Themistocles Gluck (Figure 3) [3]. The recorded attempts at those techniques occurred in the early 1890s in Germany and they included ivory implants and a cement made of rosin, pumice, and plaster [4], [7]. The results were presented at the 10th International Medical Conference [4]. Unfortunately, bone resorption caused these implants to fail [3]. Gluck was a remarkably innovative person for his time, even though his implants were unsuccessful, , as he contributed to other projects including nerve regeneration, artificial knee joints, and laryngeal surgery [8]. Figure 4 shows one of his drawings of an artificial knee joint that was found, which shows his scientific and creative nature. However, as a non-academic surgeon, it took him a while to receive the academic acclaim he deserved.

Interposition surgery also called interposition arthroplasty was another technique that was used in the late 19th and early 20th century for a dysfunctional hip. In this method, materials were inserted between the surfaces of the hip joints. Both organic and inorganic materials, including fascia lata, silver, gold foil, rubber, celluloid, and tanned pig bladder, were employed in the studies [1], [4].

Figure 2: Charles White 4 October 1728 – 20 February 1813 [9].

Figure 3: Themistocles Gluck 1853 – 1942 [8].
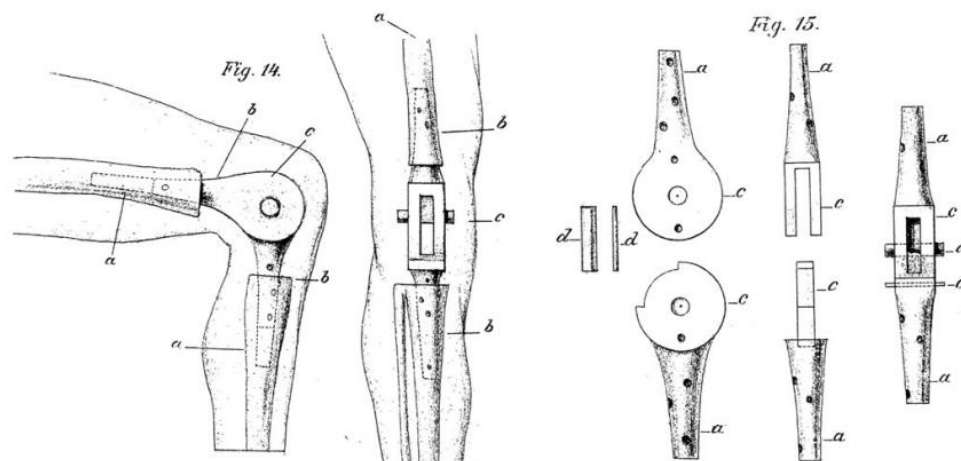
Figure 4: Artificial joint made of ivory suggested by Gluck [8].

1.1.2 Early Attempts and Techniques at Total Hip Arthroplasty

The first total hip arthroplasty was performed in 1938. The installation of stainless steel femoral and acetabular components was carried out by Philip Wiles at the Middlesex Hospital of London, and it was quite successful for a short time. His work was analyzed by Mckee, Müller, et al. Loss of fixation led to failure rates of up to 50%, hence these designs were unsuccessful [1], [3], [7]. Additionally, the majority of his records were lost during World War II [10].

Moore's work in 1940, which involved an implant with a large, typical-sized femoral head, neck, lining, and long intramedullary stem, is another outstanding example that deserves to be mentioned. This implant had a 135-degree angle to support the weight more naturally. F.R. Thomson worked with an implant at the same time that was very similar to that of Moore's [3].

After the end of World War II, in 1951 Haboush wrote about his experience using acrylic cement in total hip replacement. Moreover, he conducted some experiments with an implant made of vitallium, but due to bone stress shielding all of them were unsuccessful. After some time, Mckee, et al, used a similar implant and in time they noticed that it had better results when used with acrylic cement. Their work and implants continued to be used as a template until the late 1980s [3].

1.1.3 Later Discoveries and Methods

Professor Sir John Charnley (Figure 5), is considered the father of modern total hip arthroplasty [4]. Charnley was born in Bury, Lancashire on 29 August 1911. His education started at Bury Grammar School and his teachers noticed that he tended toward the sciences, and they urged him to pursue a career in medicine. Charnley thus enrolled at the Victoria University of Manchester's medical program in 1929 and graduated with an MB CHB in 1935 after earning a BSc in anatomy and physiology. Charnley decided to focus on the advancement of hip replacement surgery in 1958 [11]. In the beginning, he had several challenges with hip arthroplasty, including how to perfect the implants' connection to the bone and how to restore the diseased hip's mechanics [12]. He initially tried out an implant based on Teflon but unfortunately, it was unsuccessful [10]. In 1962 Charnley performed the first successful total hip replacement. His concept included the following elements: a femoral component made of stainless steel, an acetabular component made of polyethylene, and bone cement [1]. His implant is presented in Figure 6. His method was named "low-friction arthroplasty" and still gives the finest outcomes even today [2].

Figure 5: Professor Sir John Charnley (1911-1982), who shaped today's total hip arthroplasty [12].

Figure 6: *Charnley's hip implant. The femoral component is made of stainless steel and the acetabular component is made of polyethylene. It was also named "low-friction implant" and it was used in combination with bone cement* **[3]**.

In 1970 an implant that could be firmly fastened to the bone was devised and constructed by Ling (**Figure 7**) and Lee at the public research university in Exeter, United Kingdom. In combination with acrylic bone cement, the stem could maintain a strong bond with the skeleton for a long time. The implant was named the "Exeter hip" (**Figure 8**) and it became a gold standard at the time [3].

Figure 7: Robin Ling (1927 – 2017) one of the two creators of the "Exeter hip" **[3]**.

Figure 8: The "Exeter hip" femoral stem invented by Ling and Lee. It became a standard during the 1970s [3].

In 1997 Derek McMinn introduced "Hip Resurfacing Arthroplasty". This method involved the insertion of the first modern metal-on-metal resurfacing hip implant, called the "Birmingham Hip" (Figure 9). Because this technique uses a smaller implant, it results in less damage to the soft tissues during surgery [13].

Figure 9: Birmingham Hip invented by Derek McMinn in 1997 [13].

1.2 Total Hip Arthroplasty Nowadays And In The Future

In today's era, total hip arthroplasty is characterized as the most frequent and effective surgery, and rightly so, because in recent years there have been great advances in the manufacture of prosthetic implants, in surgical techniques, and in the primary stability of the hip implants [14], [15]. The advances that have been made in primary stability are especially important because the restoration of native hip biomechanics

and attaining precise implant positioning are crucial factors for positive long-term outcomes [2], [16]. Total hip replacement surgery has a well-documented 90% success rate in 10 years after the operation [17].

All these advances are contributing to the rapid increase in the use of THA and it is estimated that there will be approximately 572,000 cases per year by 2030 only in the United States [18]. It is also estimated that from 2018 to 2030 the number of THAs in Japan for men aged 40-64 years old will be increased by 103%, for men aged 65-74, by 147%, and for men aged equal to or above 75 years old, by 119% (Σφάλμα! Το αρχείο προέλευσης της αναφοράς δεν βρέθηκε.) [19].

Prediction about the increased use of THA by the year 2030 was also observed in Australia after a survey conducted in 2019 based on two scenarios. In the first scenario, the estimations about the number of THAs annually were based on the steady rate of surgery starting in 2013 (**Figure 10**), and in the second scenario were based on the continued increase in surgery rates based on growth from 2003 to 2013 (**Figure 11**) [20].

Table 1: Projected numbers of total hip arthroplasties from 2020 – 2030 in Japan [19].

	YEAR	MEN		
		40-64	65-74	≥75
Hip arthroplasty	2020	4935	4297	3068
	2021	5252	4743	3222
	2022	5597	5008	3529
	2023	5959	5267	3869
	2024	6335	5544	4225
	2025	6734	5888	4554
	2026	7150	6298	4864
	2027	7585	6793	5159
	2028	8029	7399	5439
	2029	8484	8132	5702
	2030	8936	9005	5972
Increase rate (2018 - 2030)		**103%**	**147%**	**119%**
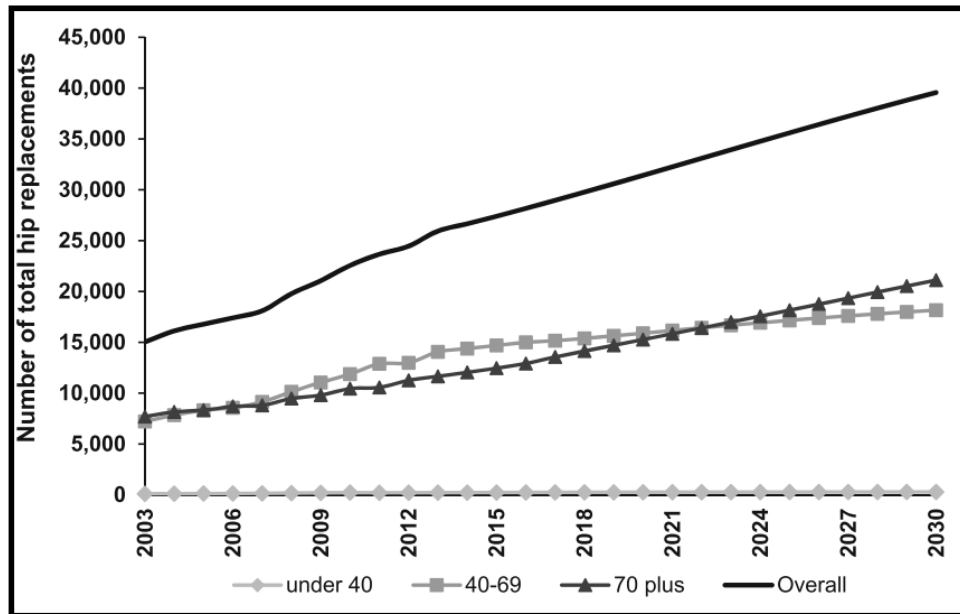
***Figure 10**: Increase in total hip replacements from 2003 to 2030 in Australia according to Scenario 1 [20].*
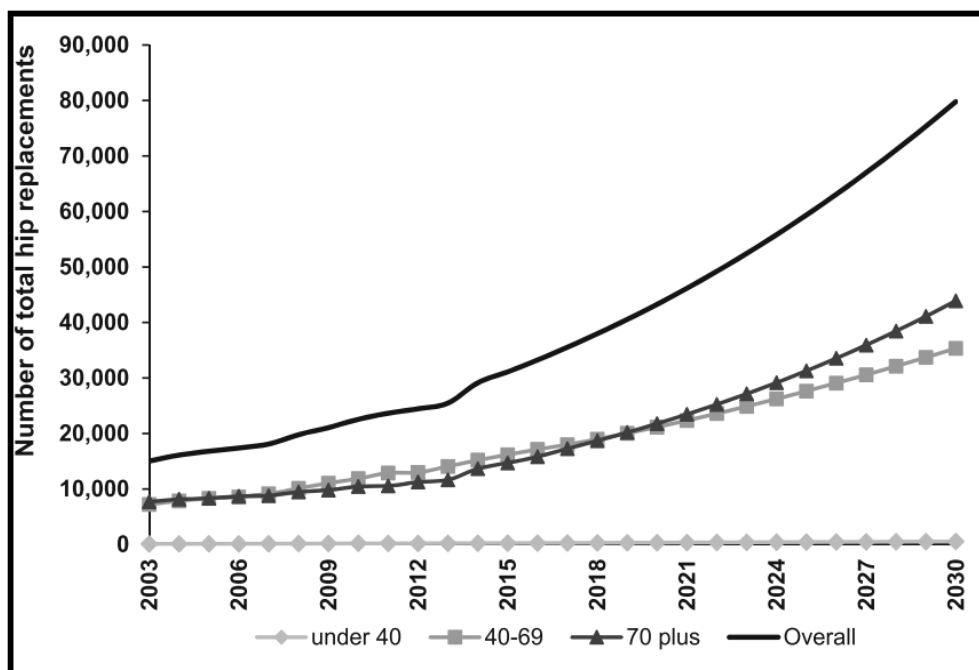
***Figure 11**: Increase in total hip replacements from 2003 to 2030 in Australia according to Scenario 2 [20].*

1.2.1 The Impact of Technological Evolution on Total Hip Arthroplasty

In recent decades, there have been tremendous advances in medical technology, specifically in the field of orthopedics, which have improved the care and quality of life of patients [21]. An example of how quickly technology is evolving in orthopedics is the number of orthopedic devices approved by the US Food and Drug Administration, which increased by 400% from 2002 to 2012 [22].

In total hip arthroplasty, extended reality (XR), 3D - printing, and robot-assisted surgery (RAS), have a significant impact on surgical education, gathering pre-operative information that helps orthopedists have a better view of the problem, and achieve better precision for the implantable stems during surgeries [23].

1.2.1.1 Virtual Reality (VR)

To enhance their skills and obtain knowledge, future surgeons usually operate on cadavers. However cadaver training is quite difficult and dangerous because it needs to be done under certain conditions, it is very costly, it takes a long time to prepare, and above all, there is a possibility that trainees may be exposed to infections [2].

Virtual reality eliminates these difficulties and makes training easier. It offers many advantages such as:

- It requires only special glasses and a pair of controllers connected to a computer.
- It can create an environment that looks exactly like the operating room; thus, the trainees are acclimatized to the space.
- The trainees can have unlimited tries and time to practice.
- With a computer, anyone can have access and train from anywhere.
- Learning surgical techniques and maneuvers leads to fewer potential mistakes upon execution.
- Trainee performance can be evaluated at any time.
- Multiple people can practice simultaneously in the same simulation; thus, teamwork and cooperation can be improved.

Virtual reality opens up a lot of possibilities for total joint arthroplasty. It is a means by which new surgical techniques and equipment can be tested, observed, and evaluated [2]. It has been demonstrated in the past that training using virtual reality simulators enhances surgeons' performance. However, the current literature does not make it clear if virtual reality offers realistic training for pin/screw placement, which is essential in orthopedic procedures [24]. Figure 12 shows a surgery that is been conducted via virtual reality simulation.
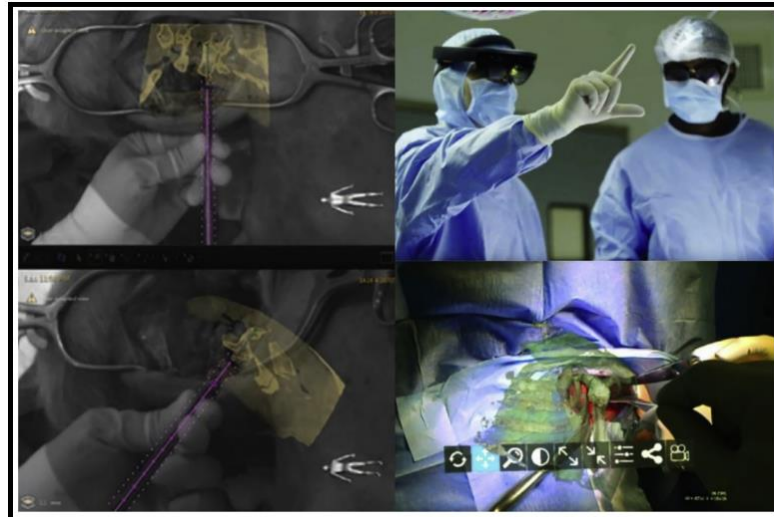
Figure 12: On the top right, two operative staff members wearing special glasses, and their visual environment is being entirely replaced by a virtual one. The rest are moments from the surgery during the simulation [25].

1.2.1.2 Contribution of 3D Printing

Three-dimensional printing (3DP), also known as additive manufacturing (AM), is a very popular procedure in medicine. It is used to create objects such as medical implants, and equipment using various materials including metals and alloys. The printing procedure is very simple; a three-dimensional design is first created using a development software on a computer (the software may be different depending on the manufacturer and model of the 3D printer) and then it is sent to a printer that produces it layer-by-layer exactly as in the design.

The contribution of 3D printing to total joint replacement has brought many advantages over the years in both implant manufacturing and surgical planning. The use of three-dimensional printing enables production of parts/implants, that were impossible to create before as well as the enhancement of already existent parts, which raises the success of many surgical procedures. Better implant manufacturing means easier application and better precision, which lead to positive long-term results. Usually, the cost of the parts/implants depends on the manufacturer, the size and cost of the machine, and the quality of the material that is used. As for surgical planning, 3DP can produce anatomical designs, assisted by CT, MR, plain radiography, and echo imagery that will help the surgeons evaluate and observe the problem from a better view before the surgery. After evaluating the problem surgeons can also produce a sequence of steps (navigation plan) that will follow during the surgery, which results in less operating time, muscle fatigue (for doctors), and expenses [26], [27].

The above-mentioned advantages of this technology are the reason why 3DP has revolutionized the industry and orthopedics and it certainly affected Total Hip Arthroplasty too. However, the applications of 3DP are still limited (generally in orthopedics) due to the processing time that is required to produce an implant of the desired quality and the price associated with extensive manufacturing [2].

1.2.1.3 Robotic Total Hip Arthroplasty

The rapid development of technology has also provided medicine with robots that assist in the surgical procedure. The robots began to associate with total hip arthroplasty in the USA and Germany in the 1990s and they were used for femoral osteotomy and implant positioning [28]. One of the first robots was ROBODOC (Figure 13), it was made by THINK SURGICAL, and in 1992 the ROBODOC team received the "Computerworld Smithsonian" award for innovation in the Arts and Sciences [29].

Nowadays, the robots used in total hip arthroplasty procedures are divided into two groups. The first group includes the semi-active robots, where the surgeon carries out the surgical act by controlling the robot's movements (robotic-arm-assisted technology). In this case, the robot prevents the surgeon from performing a movement that will cause an unfafourable situation. An example of a semi-active robot is the MAKO (Stryker, Figure 14). The second group includes the fully-active robots, which perform all the surgical procedures based on a pre-operative plan. An example of a fully-active robot is the TSolution One (THINK SURGICAL, Figure 15). Robotic total hip arthroplasty offers better precision in resection arthroplasty, for example in removing infected or damaged parts, without causing additional soft tissue damage. It provides more accurate implant positioning for the acetabular cup and femoral implant which is a crucial factor for positive long-term results. A pre-operative plan is required in robotic THA. The pre-operative plan includes creation of a three-dimensional model of the pelvis and the femur with the help of imaging tools such as computed tomography (CT) scans. The 3D model is analyzed by the robot's software and plans the position of the implant, taking into consideration the acetabular geometry and its center of rotation, the femoral torsion (femoral neck anteversion), etc. This analysis can be done by the surgeon and engineers and upload the required information into the robot's software. Some robots can choose the required implant for the surgery as well. The robot then uses this information to perform the surgery, always under the supervision of an expert [2], [28], [30], [31], [32].
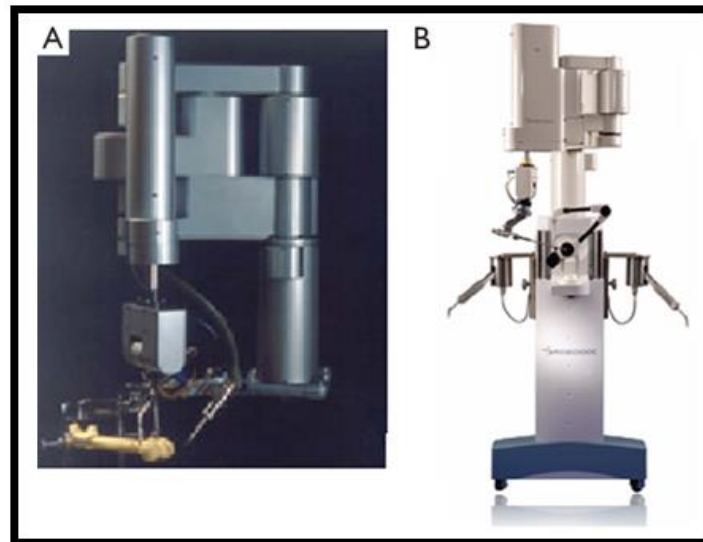
Figure 13: *ROBODOC, the first FDA-approved robot that assisted a surgeon in a THA in 1992. (A) Early prototype; (B) latest model* **[33]**.

Figure 14: *MAKO, a robotic-arm-assisted technology that helps surgeons provide patients with a personalized surgical experience* **[34]**.

Figure 15: *TSolution One, a fully-active robotic system* **[35].**

However, according to many studies, robotic THA has not provided much better results than conventional surgeries and many skeptical surgeons do not prefer to use it. Robotic THA has also high installation costs, cost of services (updating software, etc.) and it takes a long time for the surgeon to learn to operate the robot. Besides that, most contemporary robots cannot operate with various types of implants but only with specific types. There have also been recorded cases of fully-active robotic THA systems that caused soft tissue injuries and femoral fractures during the operation [2], [28], [30], [31], [32].

Taking into consideration all of the above, robotic total hip arthroplasty can certainly provide more accuracy during the operation and better post-operative results. However, several investigations still need to be done regarding its cost-effectiveness and reliability.

1.2.2 Hip Conditions that Require Total Hip Arthroplasty

The reasons that can lead a dysfunctional hip to a total replacement are varied nowadays and include diseases and injuries. The most common are Primary Osteoarthritis (POA), Avascular Necrosis of the Femoral Head (ANFH), Ankylosing Spondylitis (AS), and Rheumatoid Arthritis (RA). ANFH can occur due to many factors

such as femoral head and neck fractures, hip dislocation, slipped capital femora epiphysis as well as radiation and smoking. **Σφάλμα! Το αρχείο προέλευσης της αναφοράς δεν βρέθηκε.** presents some of the factors related to ANFH in more detail.

Table 2: *Risk factors of avascular necrosis of the femoral head* **[36], [37], [38].**

A/A	RISK FACTORS FOR AVASCULAR OF THE FEMORAL HEAD NECROSIS
1	Femoral Head and Neck Fractures
2	Hip Dislocation
3	Hematologic Diseases
4	Metabolic Diseases
5	Alimentary System Diseases
6	Intake of Steroids
7	Alcoholism
8	Smoking
9	Radiation
10	Autoimmune diseases

In total hip arthroplasty, it is very important to know the cause of the problem because different causes create different biomechanics [39]. Different biomechanics lead to different implementation techniques for doctors as well as for engineers. In the engineering part, it concerns the manufacture of an implant depending on the cause, and the creation of the appropriate tools and systems.

2. BIOMECHANICS OF THE HIP

The analysis of forces exerted on the hip joint and the distribution of strains on the femur plays a crucial role in acquiring the necessary knowledge for the experimental

phase presented later. This understanding is essential for accurately interpreting and comparing the experimental results with other studies that are going to be mentioned here. Including cadaver studies, composite studies, and even numerical simulations.

2.1 Hip Joint Forces

The hip joint is a very complex mechanism in the human body, which is responsible for supporting body weight, movement, and stability of the body. Many forces are applied to the hip joint during daily activities, such as body weight, ground reaction force, muscle force, and ligament force.

Studies that have been conducted to analyze the forces in the complex hip joint have helped to create simpler and more understandable diagrams that describe the most dominant forces in the hip joint. In **Figure 16**, the loading of the hip joint is shown, during a single-leg stance, using a simplified, two-dimensional analysis in the frontal plane.

Before proceeding with the single-leg stance in **Figure 16**, the stance on both legs should first be analyzed. When the body is supported by both legs, the center of gravity is centered between the two hips and its force is evenly distributed over both hips. Under these circumstances, the femoral heads bear an equal amount of the body's weight less the weight of both legs, and the resultant vectors of the forces are vertical [40].
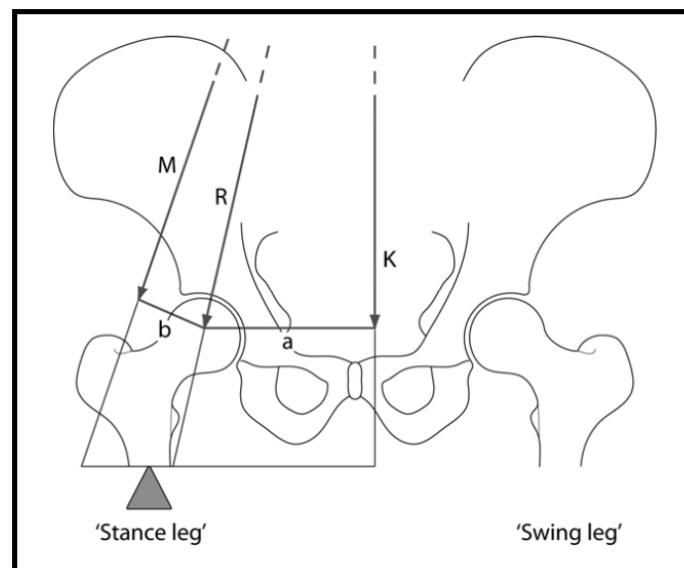
Figure 16: *A two-dimensional analysis of the hip joint in a single-leg stance. Where K is the body weight (without the weight-bearing leg), M is the abductor muscle force, R is the joint reaction force, b is the abductor muscle moment arm, and a is the body weight moment arm* **[40].**

The effective center of gravity shifts away from the supporting leg when standing on one leg because the non-supporting leg is now included in the body mass acting upon

the weight-bearing hip. The body weight (K) and its moment arm (a), produce a downward force that causes the femoral head to spin. The abductor muscles work to resist/counteract this turning motion, offering stability. The abductor muscles achieve this stability by also producing a torque on the femoral head. But because the moment arm for the abductor muscles is shorter compared to the moment arm for the body weight, the abductor muscles need to exert greater force, multiple of the body weight, to counterbalance the body weight's turning moment [40].

The moment arm ratio has a significant impact on the magnitude of the forces. The moment arm ratio is a comparison between the two moment arms a and b. It provides a measure of the mechanical advantage or disadvantage of the abductor muscles in countering the moment created by the body weight force at the hip joint. When the moment arm ratio is increased, it means that the moment arm for the abductor muscles is shortened relative to the moment arm of the body weight force. As a result, an increase in the moment arm ratio increases the force required from the abductor muscles. This also means that the force acting on the head of the femur increases as the abductor muscles work harder to stabilize the hip joint. **Figure 17** depicts how the moment arm ratio affects the force acting on the hip joint [40].
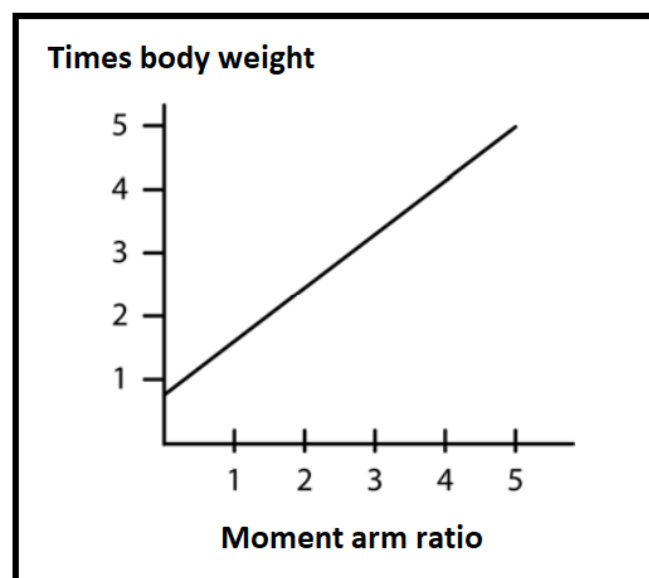
Figure 17: *Influence of moment arm ratio on the force acting on the hip joint* **[40].**

The following equation can be used to determine the abductor force (M) given the individual's weight (K), the moment arm for body weight (a), and the moment arm for the abductor muscles (b):

$$M = \frac{\frac{5}{6} \times K \times a}{b}$$

Equation 1: *Equation for calculating the abductor force on the hip joint* **[41] (edited).**

2.2 Strain Distribution of the Femur Using Cadaveric Specimens

A very valuable way to analyze the distribution of strains on the femur is by using cadaveric specimens. The use of cadaveric samples provides many advantages such as:

- **Realistic Biomechanical Depiction** – In comparison to simplified composite models, cadaveric bones offer a more accurate depiction of the mechanical characteristics and behavior of human bones.
- **Accurate Boundary Conditions** – Applying precise and patient-specific boundary conditions is possible using cadaveric bones. Engineers can more accurately simulate in vivo conditions by anchoring the bone in suitable stress equipment. This enables a better comprehension of the femur's stress distribution and reaction in a particular physiological condition.
- **Validation of Simulation Models** – It is possible to validate and enhance finite element models by using cadaveric bones. Engineers can evaluate the precision and dependability of their computational models by comparing experimental data from cadaveric testing with numerical simulations.

There are other benefits as well, such as surgical planning and ethical considerations, the analysis of which is beyond the scope of this study. Nevertheless, from an engineer's perspective, the focus is on the three mentioned above.

An excellent study of the analysis of strain distribution on the femur using cadaveric specimens has been conducted by Yekutiel Katz et al. In this study, five fresh frozen femurs were included. A three-dimensional DIC , and 17 stain gauges were used to map the strains on the femurs.

Figure 18 shows the femurs and the strain gauge locations. PMMA was used to embed the femurs inside a steel cylinder. Femurs were installed in a custom-made jig with little lateral friction and loaded up to 1.500N in stance position at 0,5 mm/min under a 7-degree tilt (**Figure 19**). The specimen FFB3L had strain gauges attached only at the diaphysis, and the rest of the specimens had strain gauges attached on the

diaphysis as well as on the neck. Specimen FFI1L had no strain gauge attached to its superior neck due to an osteophyte.

Figure 18: *The five femurs embedded in a steel cylinder and the strain gauges' locations on the femurs* **[42]**.
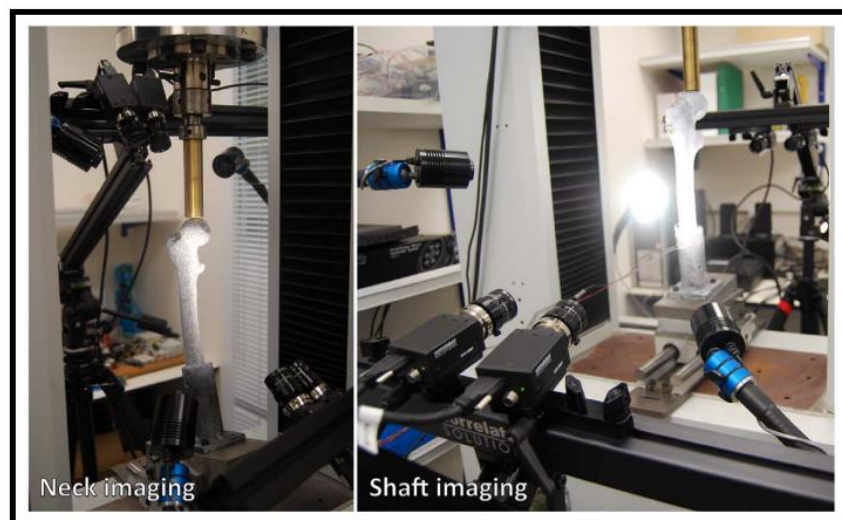
Figure 19: *Two three-dimensional DIC systems (one for the diaphysis and one for the neck) and the loading set-up* **[42]** *(edited).*

The following graphs (Figure 20, Figure 21, Figure 22, Figure 23, and Figure 24) present the strains on the bone as a function of the force applied to the femurs. The value RMSE in the graphs stands for "Root Mean Square Error" and it is a commonly used metric to evaluate the accuracy of a model or the agreement between measured data and predicted values. In the following graphs, the RMSE is used as a measure of the discrepancy between the two measurement techniques.
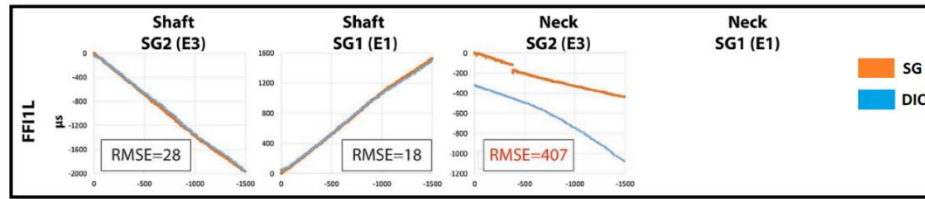
Figure 20: *Strain measurements for the specimen FFI1L* [42] *(edited).*
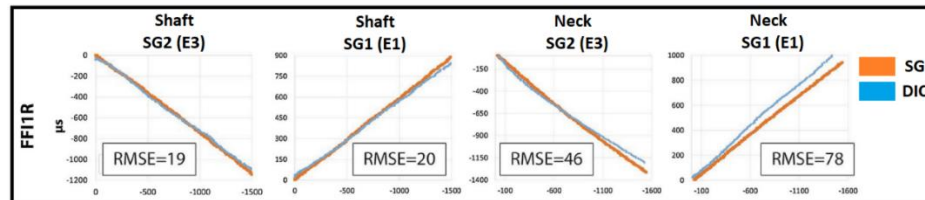
Figure 21: *Strain measurements for the specimen FFI1R* [42] *(edited).*
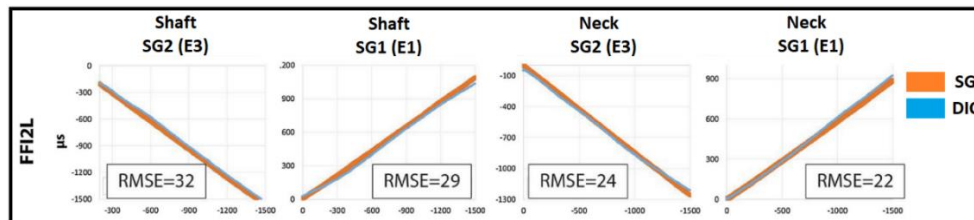
Figure 22: *Strain measurements for the specimen FFI2L* [42] *(edited).*
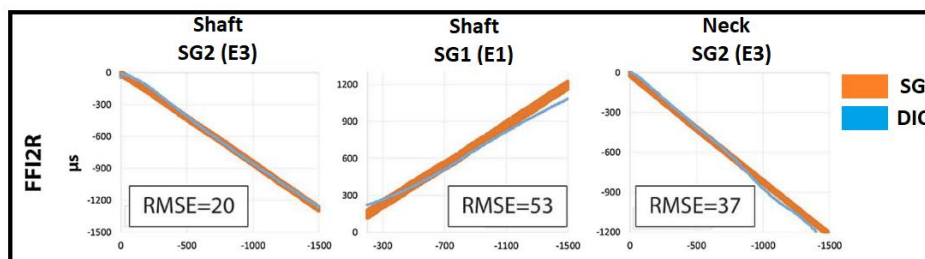
Figure 23: *Strain measurements for the specimen FFI2R* [42] *(edited). The strain gauge SG1 on the neck was damaged during the experiment and the measurements were not available.*
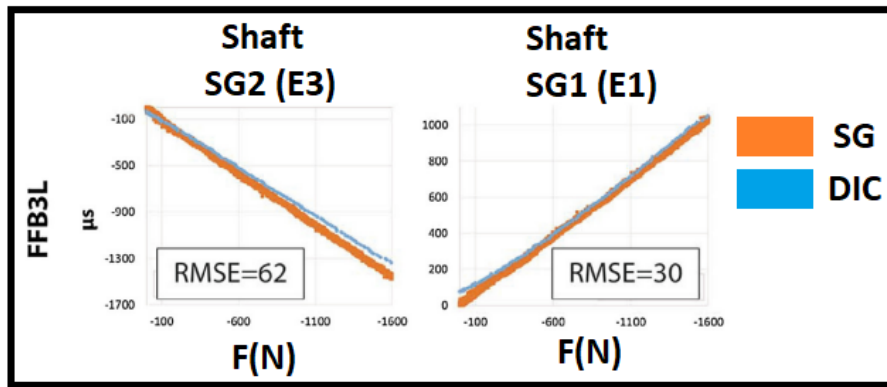
Figure 24: *Strain measurements for the specimen FFB3L* **[42]** *(edited).*

According to the above graphs, the RMSE between DIC and SG is below 50 μs in most cases, which shows that the measurements from DIC and SG are approximately the same. The only poor measurements were those of strain gauge SG2 at the neck of the specimen FFI1L. The authors explained that this happened due to the proximity of this strain gauge to the edge of the DIC analysis region, there was significant noise in the DIC strains. Additionally, in the same graph, it is noticeable a "jump" that leads one to infer debonding.

A comparison of the strain fields derived from DIC measurements and FE predictions was performed using the Robust Linear Regression statistical method, as it appears in the following graphs (**Figure 25**, **Figure 26**, **Figure 27**, **Figure 28**, **Figure 29**).
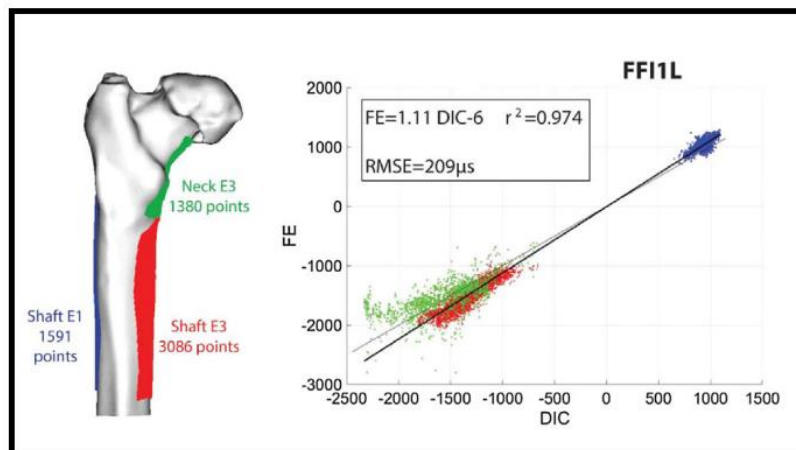
Figure 25: *Comparison of the strain fields obtained from DIC measurements to FE predictions for specimen FFI1L* **[42]** *(edited).*
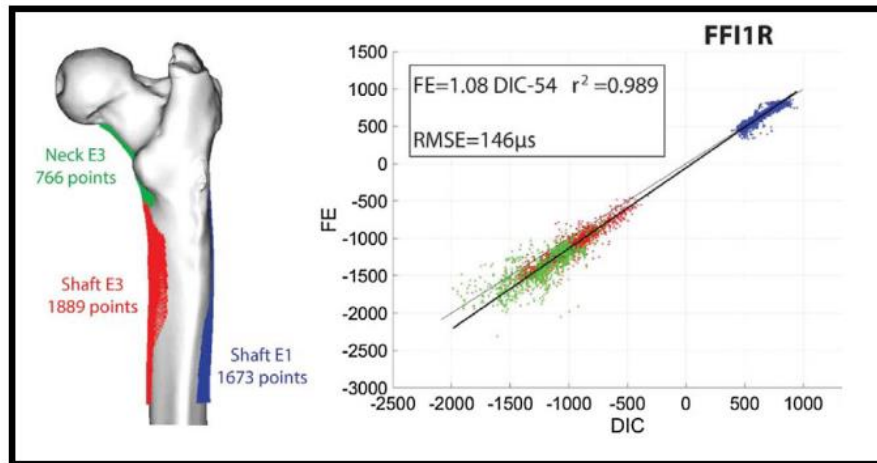
Figure 26: *Comparison of the strain fields obtained from DIC measurements to FE predictions for specimen FFI1R [42] (edited).*
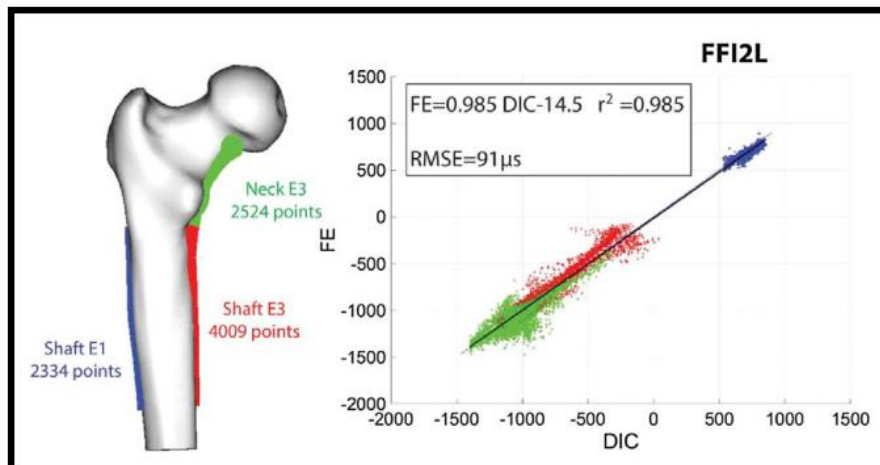
Figure 27: *Comparison of the strain fields obtained from DIC measurements to FE predictions for specimen FFI2L [42] (edited).*
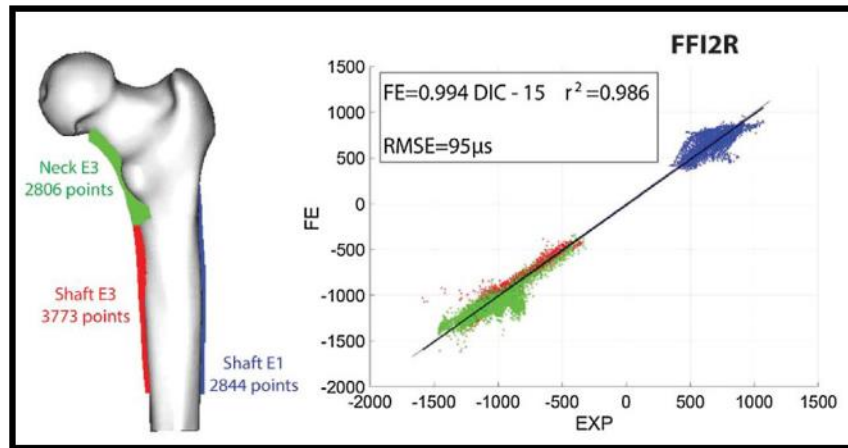
Figure 28: *Comparison of the strain fields obtained from DIC measurements to FE predictions for specimen FFI2R* **[42]** *(edited).*
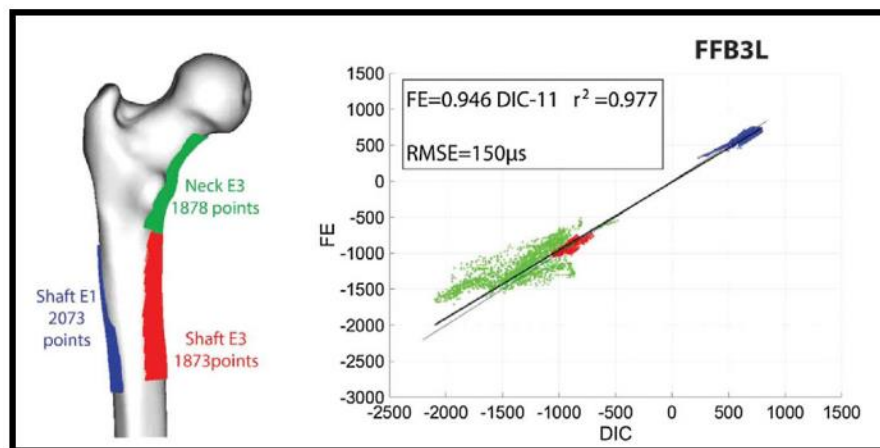
Figure 29: *Comparison of the strain fields obtained from DIC measurements to FE predictions for specimen FFB3L* **[42]** *(edited).*

Strain measures the deformation or elongation of a material relative to its original length or shape. It quantifies how much a material has been stretched or compressed. In the graphs, positive values indicate tensile strains, while negative values indicate compressive strains. According to the authors, the medial diaphysis and the neck have the largest strain fields, which means they experience the most deformations when pressure is applied to the femur. Thus, The whole experiment was conclusively conducted for these regions.

For the superior neck surfaces the strain distribution for each cadaveric specimen is shown in **Figure 30**, **Figure 31**, **Figure 32**, and **Figure 33**(except for the specimen FFI1L due to osteophyte), deformations can be seen throughout the superior neck, with the largest being at its edges (the point where the superior neck connects with the

femoral head and the point where the superior neck connects with the greater trochanter).
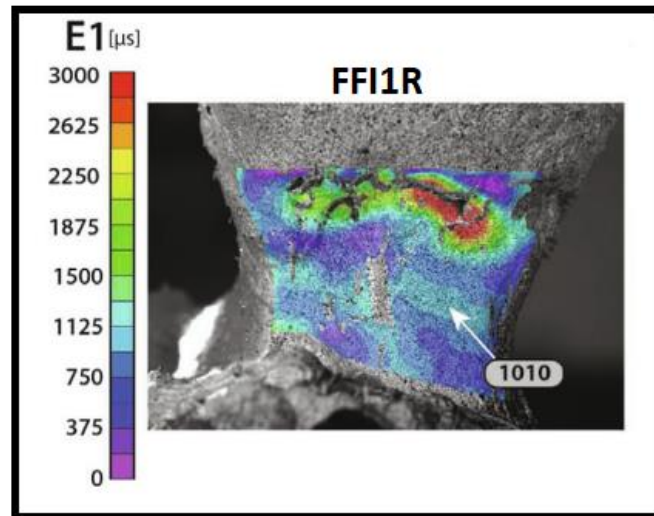
Figure 30: *Strain distribution at the superior neck of the specimen FFI1R* **[42]** *(edited).*
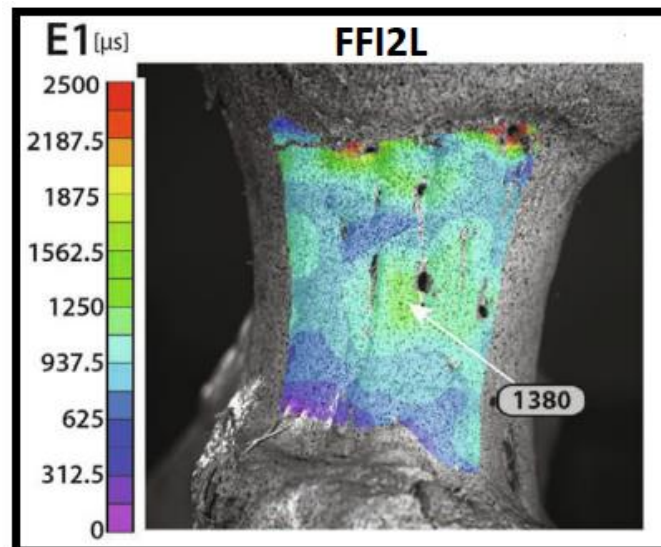
Figure 31: *Strain distribution at the superior neck of the specimen FFI2L* **[42]** *(edited).*
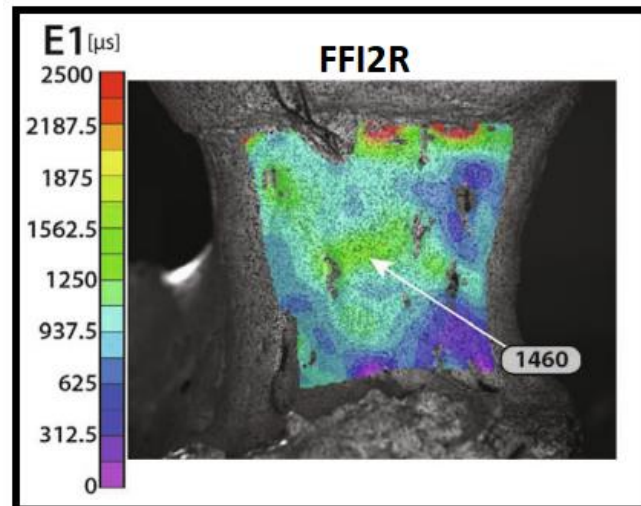
Figure 32: *Strain distribution at the superior neck of the specimen FFI2R* **[42]** *(edited).*
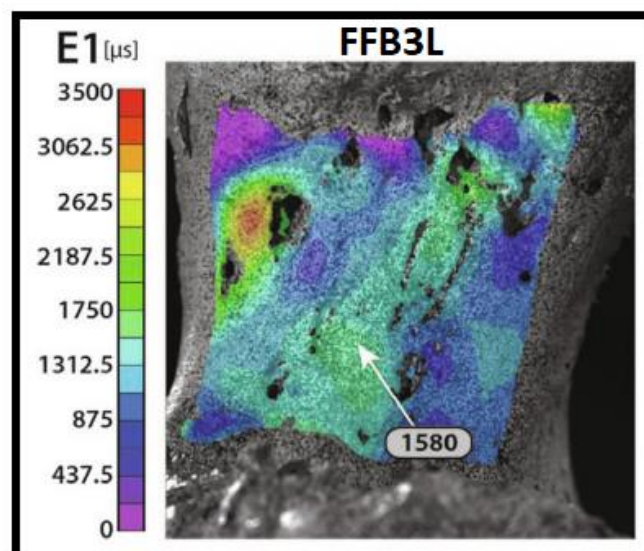
Figure 33: *Strain distribution at the superior neck of the specimen FFB3L* **[42]** *(edited).*

2.3 Strain Distribution of the Femur Using Numerical Simulations

Another valuable way to analyze the distribution of strains on the femur is by using numerical simulations such as Finite Element Analysis (FEA). This technique involves many advantages in comparison with the studies that use cadaveric or composite specimens. Here are some of the advantages that FEA offers:

- **Cost-Effectiveness** – It can be costly and time-consuming to make composite bones or conduct tests on cadaveric bones. FEA offers a more

economical method because it does not require physical prototypes or specimens, saving money on testing and material costs.

- **Detailed Information –** The distribution of strain and stress in the femur may be precisely determined using FEA. Engineers can identify key areas, analyze stress concentrations, and assess the impacts of various loading scenarios. Due to physical measurements' potential limitations or understandable issues, this degree of detail is difficult to attain using only experimental techniques.

- **Infinite Design Customizations –** Engineers can quickly adapt and enhance their designs in response to FEA analysis findings. It is possible to discover potential design flaws, make the necessary corrections, and then assess the effects of these modifications on the stress distribution by iteratively improving the model. This iterative technique can produce designs for femurs that are more effective and reliable.

In a FEA of the human that was conducted by A. Latif Aghili, et al, the three-dimensional human femur was constructed using the reverse engineering modeling method. The geometry and shape of the femur were captured by a 3D-Laser scanner DS-3040 (Laser Design Inc., CMM, US) [43].

The 3D model was then tested under three different forces, as shown in Figure 34, and the strain distribution for each case is shown in Figure 35, Figure 36, and Figure 37 below.

(a) Single force. (b) Full distributed vertical force. (c) Partial distributed vertical force.
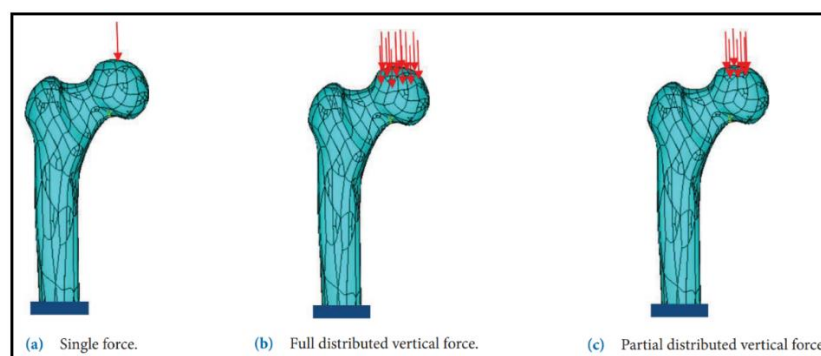
Figure 34: *The three different forces that the model was tested* **with [43]** *(edited).*
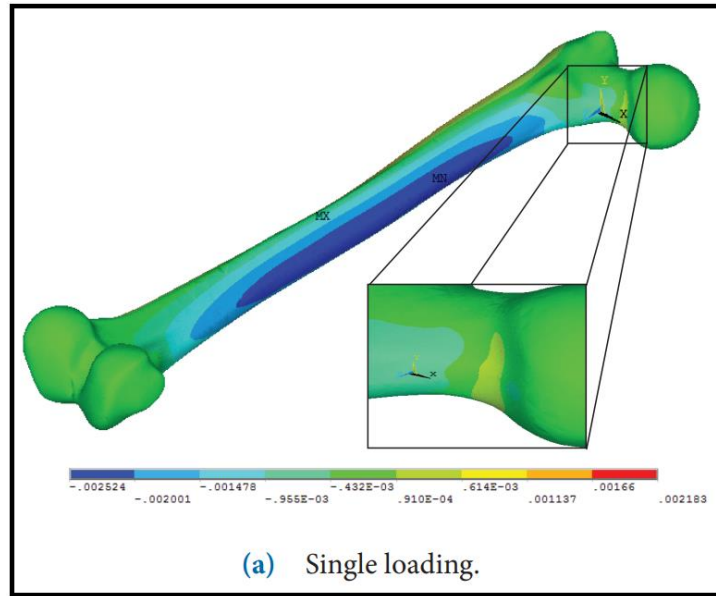
(a)   Single loading.

Figure 35: *Strains distribution during single force under loading of a 2500 N* [43] *(edited)*.
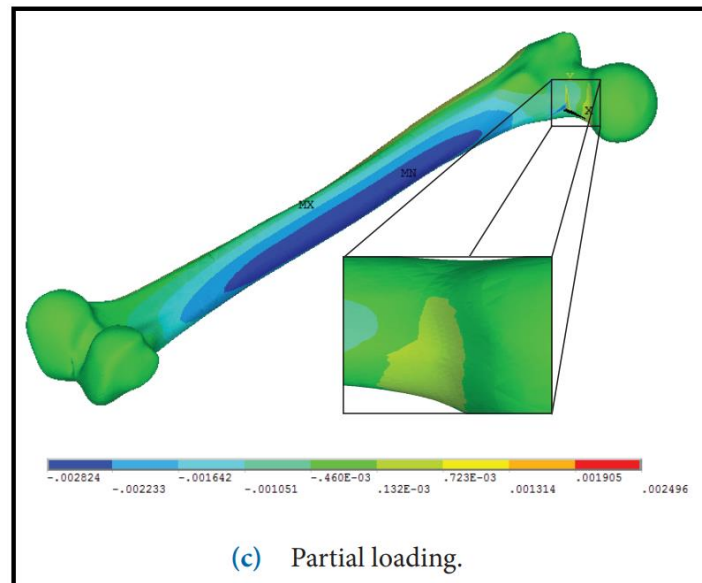
(c)   Partial loading.

Figure 36: *Strains distribution during partial force under loading of a 2500 N* [43] *(edited)*.

(b) Full loading.
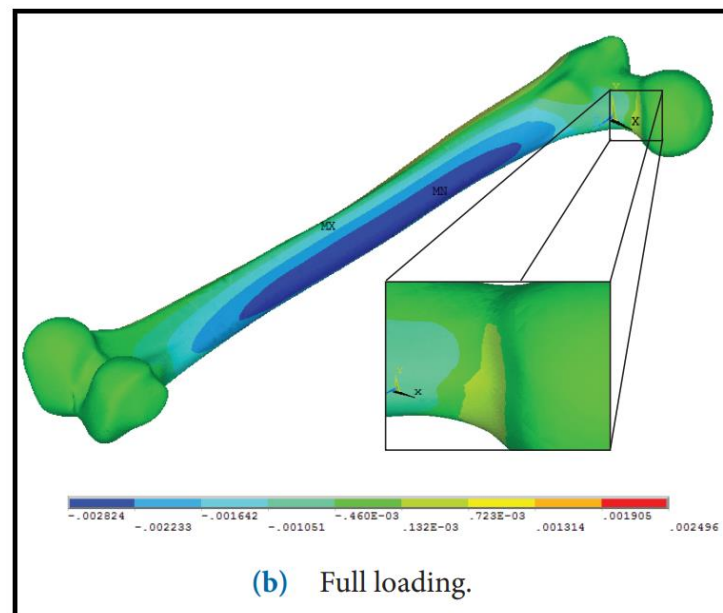
Figure 37: *Strains distribution during full force under loading of a 2500 N* **[43]** *(edited).*

According to the strain distributions above, the inferior neck and the medial diaphysis experience the biggest deformations during the loadings. Taking into consideration the results from the cadaveric study that was analyzed in subsection 2.2.2, the three-dimensional model that was created and the simulation were successful.

2.4 Strain Distribution of the Femur Using Composite Femur Models

A third valuable way to monitor the strains on the human femur is by using composite femur models. The first composite bone models appeared in the late 1980s. An epoxy-reinforced, braided glass sleeve encircled a stiff polyurethane foam core in the first-generation models, which served as the first composite bone that was biomechanically meaningful [44]. Other materials are used to manufacture composite bones such as epoxy resin, carbon fiber, etc.

In experimental studies, the use of composite bones offers many advantages:

- **Cost-Effectiveness** – Compared to cadaveric specimens, composite femur models are typically less expensive to make and get. The acquisition, preservation, and storage of cadaveric specimens are necessary but can be expensive and difficult.

- **Durability** – Comparatively to cadaveric specimens, which over time experience natural tissue decomposition, composite femur models are more resilient and less prone to degeneration. Composite models are long-term used

for research because they may be preserved for long periods without experiencing major changes in their mechanical characteristics.

- **Flexibility in experimental design** - Researchers can alter the geometry and material characteristics of composite femur models to suit particular experimental needs. This adaptability allows for the analysis of a variety of situations, such as changing bone density, surgical procedures, or the assessment of novel implant designs.

However, it is very important to evaluate the measurements obtained from experiments with composite bone, comparing the results with those of cadaveric studies, to be sure that the composite bone correctly represents the mechanical properties of human bone.

An excellent study of mechanical validation of whole bone composite femur models has been conducted by Luca Christofolini, Marco Viceconti, et al. In this study, the mechanical behavior of composite femur models (Pacific Research Labs) was compared to human fresh-frozen and dried-rehydrated specimens under different loading conditions. The study included several tests such as the deflection under axial load, the strain distribution under axial load, bending, and torsional stiffness [45].

The research demonstrated that they are identical to the population of human femurs in terms of their axial bending and torsional stiffnesses, as well as the strain distributions under load. Therefore, it is safe to conclude that the composite femur model represents one human specimen [46].

In a more recent study that was conducted by Semi P. Väänänen, et al, six fourth-generation medium-sized composite femurs for Sawbones (Pacific Research Laboratories, Inc., Vashon Island, WA, USA) were tested. The proximal components were positioned in the center of a 50mm high, 50mm in diameter inside, and 3mm thick aluminum cylinder. Epoxy was used to fill the cylinders and secure the shafts. The bones were mechanically tested under axial compression until they broke. Using a DIC system, the displacements and the surface strains were captured [47]. In **Figure 38**, it is presented the loading setup.

For five of the bones (B2-B6), the fractures occurred at the point where the neck connects with the great trochanter (Figure 39), while the fracture of the sixth bone (B1) occurred below the great trochanter (Figure 40).

Figure 41 displays the load-displacement curves for all six composite bones in axial compression. Except for bone B4, which exhibited a higher stiffness and ultimate

strength than the other bones, the load-displacement curves for the majority of the bones displayed comparable behavior in the linear region. According to the graph, the load at fracture ranged between 4954 (N) to 6747 (N).

Figure 42 presents the von Mises strains for all six bones at equal forces close to the moment of fracture. The von Mises strains imply the combined effect of axial and shear strains. According to the graphs, the biggest deformations occur in the neck and in the diaphysis, which is the same as those of the cadaveric study and the finite element analysis presented in subsections 2.2.2 and 2.2.3.
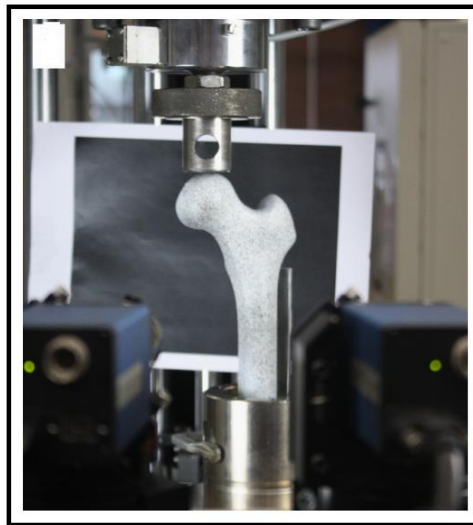
Figure 38: *The loading set-up of the experiment* [47] *(edited).*

Figure 39: *Fracture locations of composite bones B2-B6* [47] *(edited).*

Figure 40: *Fracture locations of composite bone B1* **[47]** *(edited).*
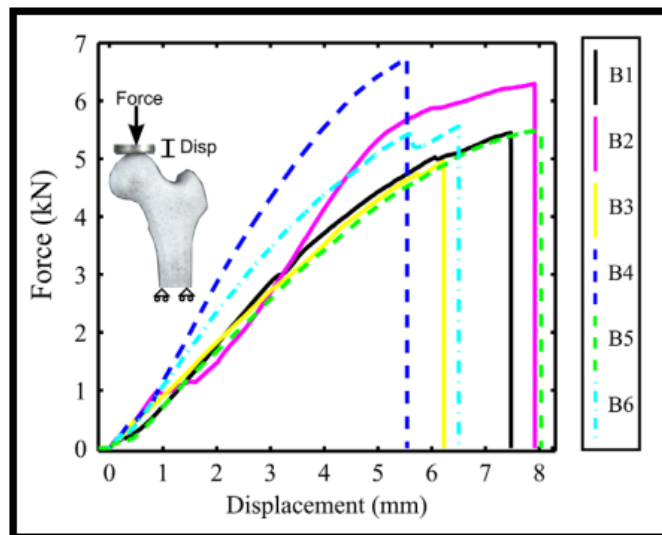
Figure 41: *Load-displacement curves for all six composite bones in axial compression* **[47]** *(edited).*
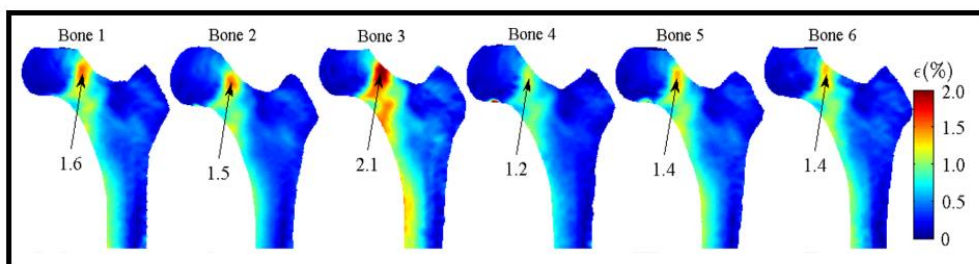
Figure 42: *Von Mises strains for all six bones at equal forces close to the moment of fracture* **[47]** *(edited).*

3. HIP IMPLANTS

Orthopedics has made great strides over the years, particularly in the area of hip implants. The hip joint is a fundamental part of the musculoskeletal system and is essential for both movement and stability. Hip implants are required to restore function and improve patients' quality of life because aging, trauma, and degenerative diseases can all cause this vital joint to deteriorate.

This chapter explores the complex world of hip implants, highlighting various elements that affect their mechanical performance, materials used in their manufacture, manufacturing processes used, and evaluation tests carried out to guarantee their dependability and longevity. Engineers and researchers working on the creation and use of hip implants must have a thorough awareness of these crucial aspects.

In the first section of this chapter, are presented the mechanical characteristics of the human femoral bone. For implants to accurately match the hip joint's natural biomechanics and provide optimal load distribution and long-term stability, it is essential to understand the structural properties of the cortical and trabecular bone.

The components used to make hip implants are the subject of the next section. Each material has unique qualities that affect the implant's longevity, biocompatibility, and resistance to wear, ranging from conventional metals like titanium and stainless steel to cutting-edge materials like cobalt-chromium alloys and ceramic composites.

Following that, the manufacturing processes used to create hip implants are investigated. Every technology, from traditional casting and machining methods to more contemporary innovations such as additive manufacturing, poses specific benefits and drawbacks. Engineers may design and create implants with exact geometry and enhanced functionality by having a thorough understanding of these production processes.

The last section focuses on the evaluation tests used to evaluate the mechanical performance and dependability of hip implants. To ensure that the implant can endure the rigors of everyday activities and prolonged use, stress testing, in particular, plays a significant role in imitating the real-world circumstances faced by the implant within the human body.

3.1 Mechanical Properties of Human Femoral Bone

The bone tissue in the femur is divided into cortical and trabecular tissue. The diaphysis of the femur consists of cortical tissue, while the metaphysis and epiphysis (upper and lower parts) are mainly trabecular. The cortical tissue has a different porosity and molecular structure than cancellous tissue. This indicates that each tissue has different mechanical properties.

3.1.1 Cortical Bone

The porosity of cortical bone ranges from 5% to 15%, and it refers to the amount of empty spaces or pores within the tissue. The cortical bone also presents anisotropic material behavior, which means that its mechanical properties vary depending on the direction in which the force is applied. In simpler words, the response of cortical bone to external loads is not the same in all directions.

Σφάλμα! Το αρχείο προέλευσης της αναφοράς δεν βρέθηκε. presents the elastic, yield, and ultimate properties of human femoral cortical bone in longitudinal and transverse directions, where it is observed that cortical bone has greater strength and tensile/compressive moduli along its longitudinal direction than its radial and circumferential directions [48].

Cortical bone displays a bilinear stress-strain response when force (tension or compression) is applied along the longitudinal direction. **Figure 43** presents the stress-strain curve for cortical bone along the longitudinal direction. The graph presents the yield and ultimate point as well. The pink area represents the elastic region whereas the area in blue represents the plastic region.

When a material is subjected to increasing levels of stress, it initially deforms elastically, meaning that it returns to its original shape once stresses are removed. However, as the stress continues to increase, the material eventually reaches a point where it starts to undergo plastic deformation. At this point the material experiences permanent and non-reversible deformation. The point where the elastic changes to plastic deformation is called the yield point. The ultimate point represents the highest stress point on the stress-strain curve where the material fractures.

When the stress applied to cortical bone exceeds its yield point, the material properties start to degrade (**Figure 44**). This means that the bone undergoes damage, leading to changes in its mechanical properties. Cortical bone damage has also been defined in terms of degeneration in the tissue's microstructure and/or nanostructure, commonly known as microdamage. These microdamages can contribute to bone

fragility because they weaken the overall structure of the bone. However, interestingly, they can also act as a strengthening mechanism . This means that the presence of microdamages can enhance the bone's ability to resist further damage. In vitro, studies have shown that the presence of microdamage, especially in the form of linear microcracks, can enhance the bone's resistance to further crack growth [48].

Table 3: *Elastic, yield and ultimate properties of human femoral cortical bone [48] (edited). The values listed are from mechanical tests done on specimens with a typical size of the order of one centimeter.*

The indicators placed at the end of the values indicate the following:

[B] ⇨ From Reference [49], [C] ⇨ From Reference [50],

[D] ⇨ Circumferential Direction

[E] ⇨ Radial Direction

[F] ⇨ Calculated using 0.2% offset

Longitudinal Direction	
Elastic modulus (MPa)	17,900 ± 3,900 [B]
	18,160 ± 1,880 [C]
Poisson's ratio	0.62 ± 0.26 [B]
Tensile yield stress (MPa)	71.56 ± 10.19 [C, F]
Tensile yield strain (%)	0.67 ± 0.04 [C, F]
Tensile ultimate stress (MPa)	135 ± 15.6 [B]
	92.95 ± 10.07 [C]
Tensile ultimate strain (%)	1.9 ± 0.6 [C]
Compressive yield stress (MPa)	115.06 ± 16.36 [C, F]
Compressive yield strain (%)	0.98 ± 0.09 [C, F]
Compressive ultimate stress (MPa)	205 ± 17.3 [B]
	153.59 ± 21.63 [C]
Compressive ultimate strain (%)	1.3 ± 0.3 [C]
Shear modulus (MPa)	3,300 ± 400 [C]
	6,070 ± 570 [C]
Shear yield stress (MPa)	40.95 ± 5.16 [C, F]
Shear yield strain (%)	0.87 ± 0.04 [C, F]

Shear ultimate stress (MPa)	65 ± 4.0 [B]
	46.31 ± 5.82 [C]
Transverse Direction	
Elastic modulus (MPa)	10,100 ± 2,400 [B]
	5,650 ± 1,610 [D]
	6,490 ± 3,220 [E]
Poisson's ratio	0.62 ± 0.26 [B]
Tensile ultimate stress (MPa)	53 ± 10.7 [B]
Compressive yield stress (Mpa)	41.8 ± 19.4 [D]
	44.1 ± 21.1 [E]
Compressive yield strain (%)	0.83 ± 0.42 [D]
	0.84 ± 0.23 [E]
Compressive ultimate stress (Mpa)	131 ± 20.7 [B]
	65.2 ± 13.8 [D]
	63.1 ± 20.7 [E]
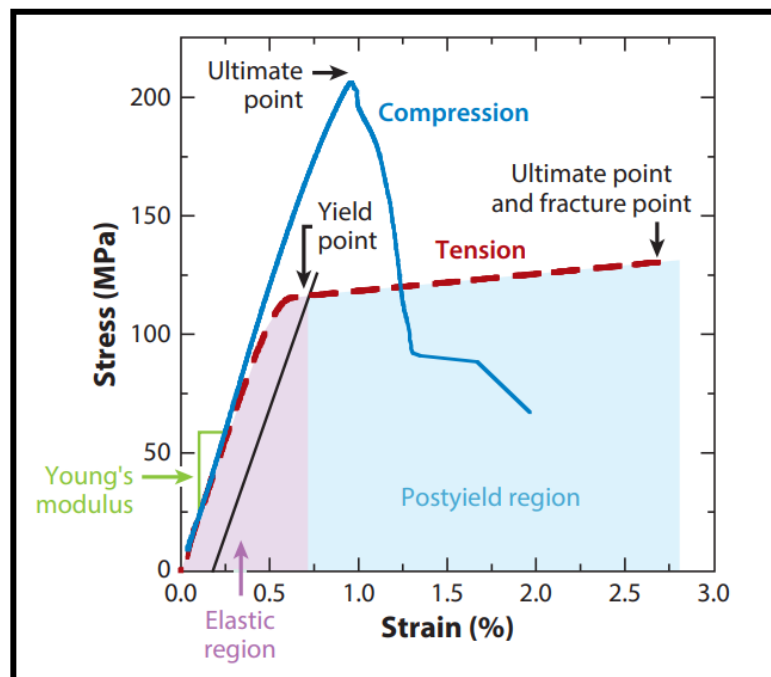
Figure 43: *Stress-strain curve for cortical bone tested along the longitudinal direction* [48] *(edited)*.
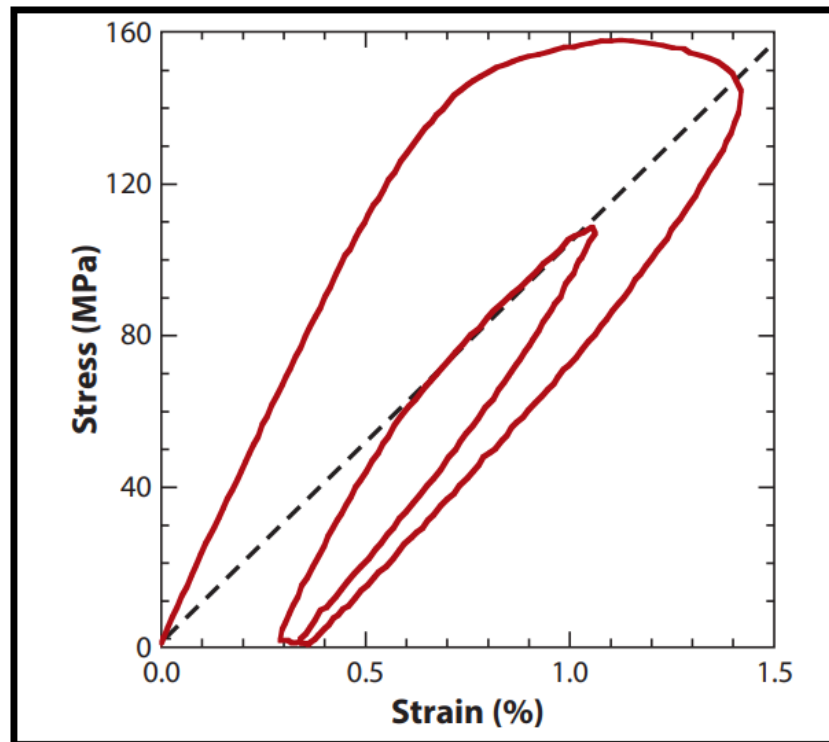
Figure 44: *Stress-strain curve for cortical bone along the longitudinal direction. A load-unload-reload test. The dashed lines indicate the perfect damage modulus, which is the secant modulus at the point at which the initial loading ramp is reversed to begin unloading* [48] *(edited).*

Examples of how microdamages look in cortical bone are shown in Figure 45, Figure 46, Figure 47, and Figure 48. The first two figures (Figure 45, Figure 46) present linear microcracks in the human vertebrae that were acquired using bright-field microscopy and laser scanning confocal microscopy, respectively, and the other two figures (Figure 47, **Figure 48**) present diffuse damage in human vertebrae that were acquired using bright-field microscopy and laser scanning confocal microscopy, respectively [48].

Cortical bone can fracture due to repetitive or excessive loads. The fracture toughness of cortical bone is anisotropic and influenced by intrinsic and extrinsic toughening mechanisms. The preferential alignment of osteons (the structural units of cortical bone) contributes to the anisotropic fracture toughness, with crack bridging being an important toughening mechanism (**Figure 49**, **Figure 50**). Cortical bone also shows better resistance to fatigue failure in compression compared to tension [48].
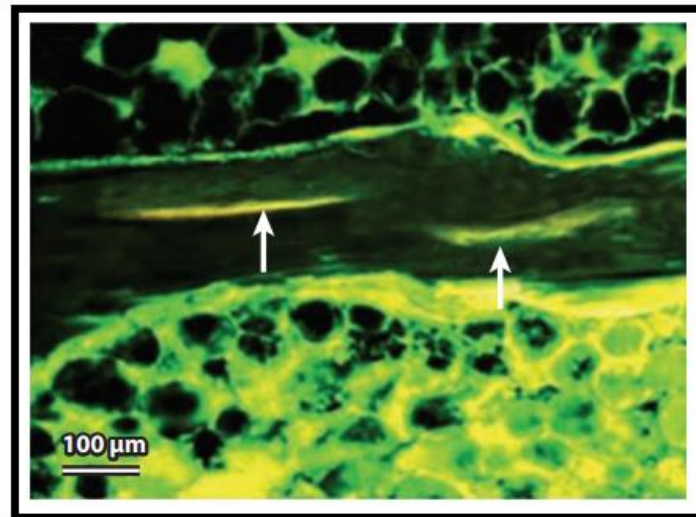
Figure 45: *Linear Microcrack – Bright Field Microscopy* **[48]** *(edited).*
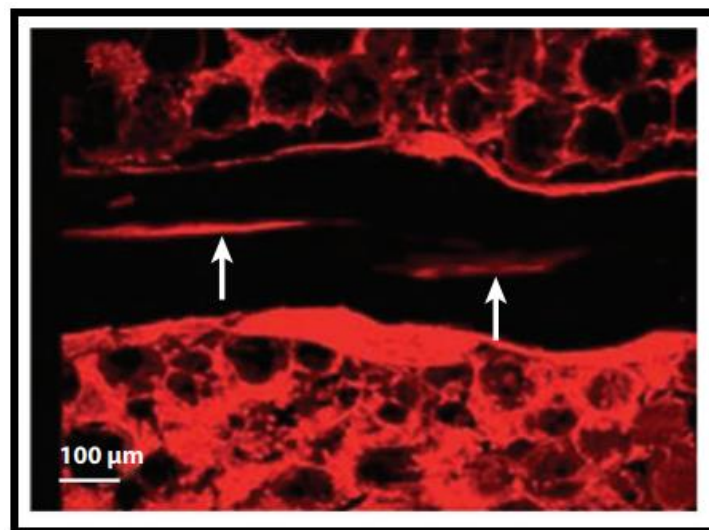
Figure 46: *Linear Microcrack –Laser Scanning Confocal Microscopy* **[48]** *(edited).*
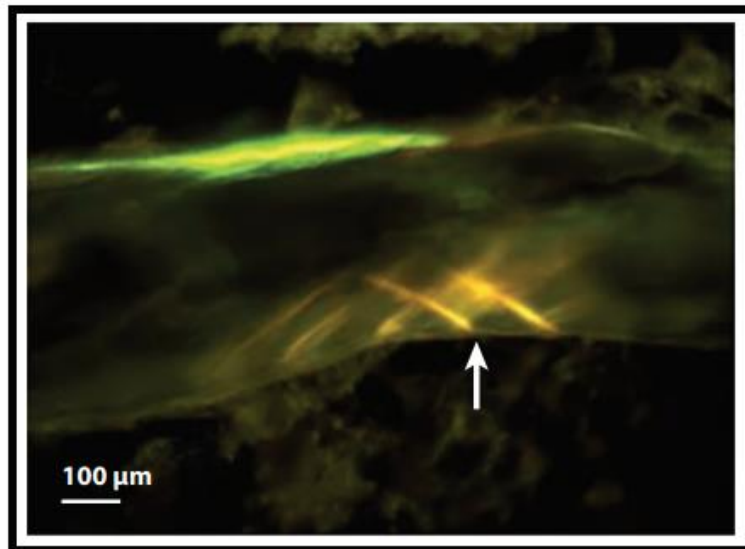
Figure 47: *Diffuse Damage – Bright Field Microscopy* **[48]** *(edited)*.
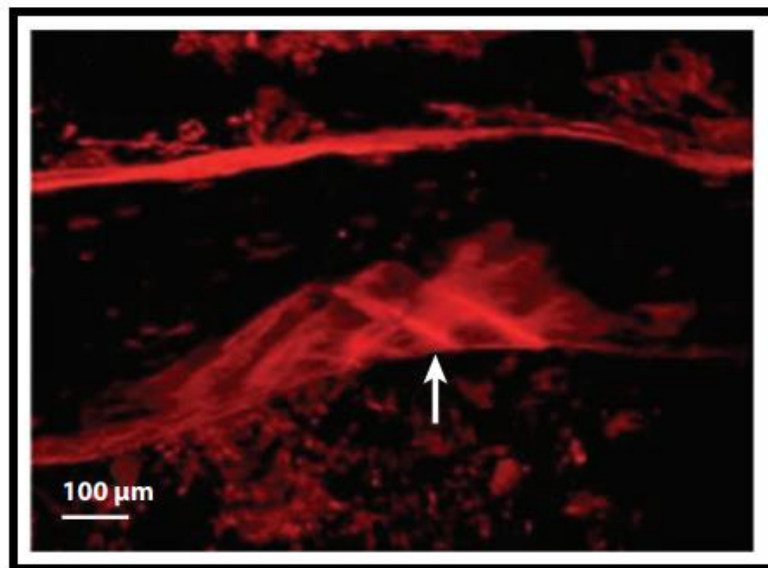
Figure 48: *Diffuse Damage – Laser Scanning Confocal Microscopy* **[48]** *(edited)*.
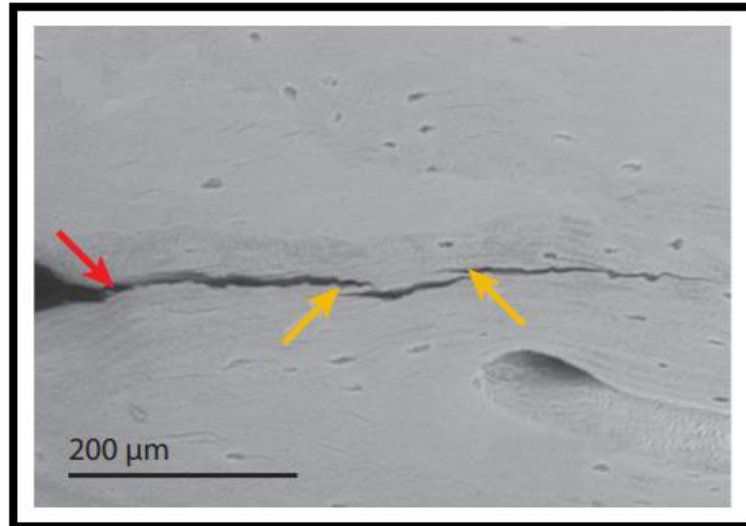
Figure 49: *Crack propagation starting from a notch indicated by the red arrow. The yellow arrows represent the uncracked ligament bridging which is one of the processes used in cortical bone to strengthen it* **[48]** *(edited).*
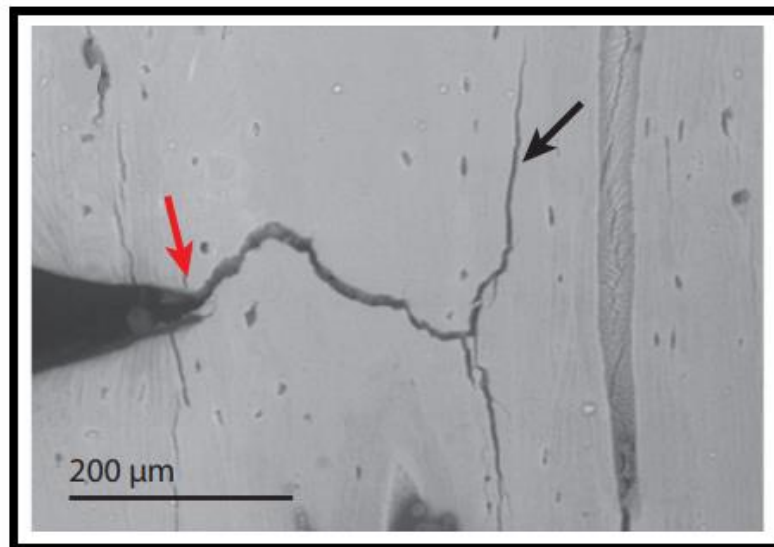
Figure 50: *Crack propagation starting from a notch indicated by the red arrow. The black arrow shows the crack deflection which is one of the cortical bone's toughening mechanisms* **[48]** *(edited).*

3.1.2 Trabecular Bone

The trabecular bone has anisotropic mechanical properties and is a highly porous material (40% to 95% porosity). The apparent-level mechanical characteristics of trabecular bone are principally influenced by its increased porosity compared to cortical bone.

Similar to cortical bone, trabecular bone is stronger in compression than tension and weakest in shear, however, these distinctions become less significant as apparent density decreases. The stress-strain curve of trabecular bone does not show a well-defined yield point (Figure 51) as in cortical bone. Trabecular bone is often treated as a linear elastic material. This means that it is assumed to exhibit linear stress-strain behavior within a certain strain range, as **Figure 51** shows. To determine the elastic modulus of trabecular bone, a linear or polynomial function is fitted in the low-strain region, where the material also behaves approximately linearly. The slope of this curve represents the elastic modulus of the trabecular bone.
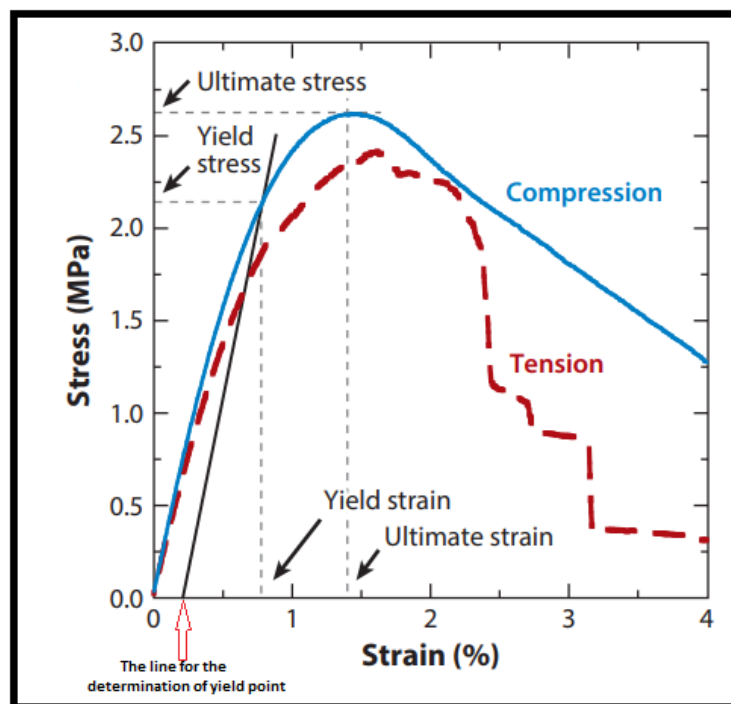
Figure 51: *Stress-strain curve for trabecular bone tested along the principal direction* **[48]** *(edited).*

The 0.2% offset method is used to determine the yield point, which indicates the onset of permanent deformation, as was explained in the previous section for the cortical bone. Specifically, a line is drawn parallel to the linear, elastic region of the stress-strain curve, but displaced horizontally by a distance equal to 0.2% of the strain. The point at which this line intersects the stress-strain curve is considered the

approximate yield point. **Figure 52**, also shows the load-unload-reload test for trabecular bone.
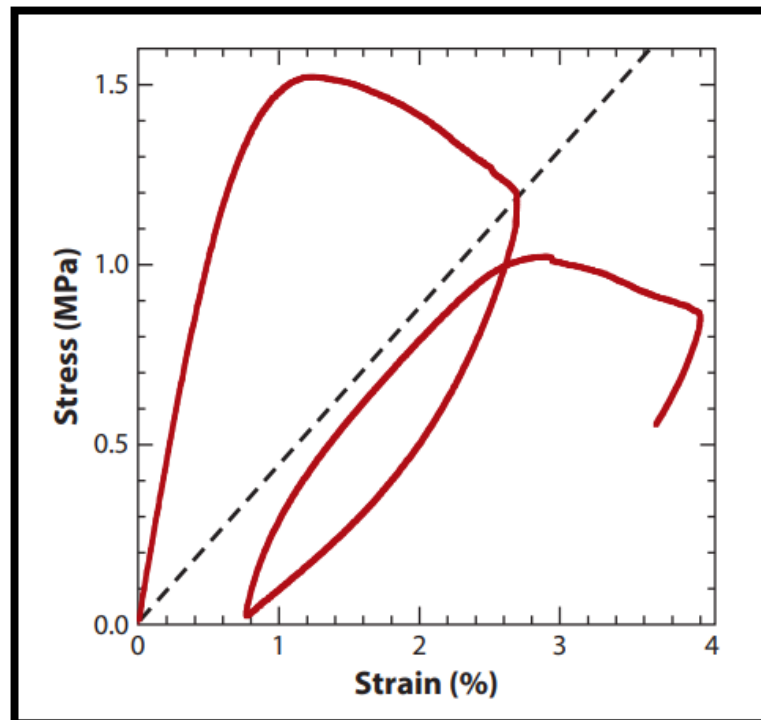
Figure 52: *Stress-strain curve for trabecular bone along the principal direction. A load-unload-reload test. The dashed lines indicate the perfect damage modulus, which is the secant modulus at the point at which the initial loading ramp is reversed to begin unloading* **[48]** *(edited).*

Overloading of trabecular bone causes microcracking and damage to the trabeculae. The orientation and local thickness of trabeculae play a part in the propagation of damage and yielding, which are both impacted by the anisotropic nature of the trabecular bone. **Figure 53**, presents the crack propagation in the trabecular bone.
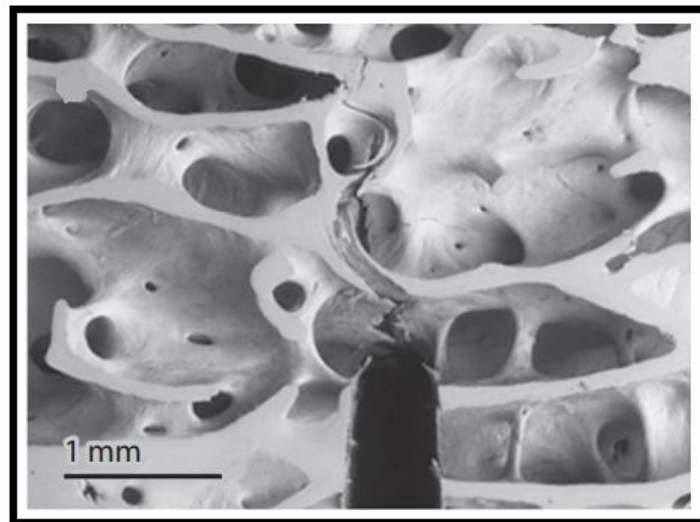
Figure 53*: Crack propagation in trabecular bone* **[48]** *(edited)*.

3.1.3 Insights and Concluding Remarks

Based on the previous subsections, the overall behavior of the bone's material is anisotropic. This means that the bone exhibits different mechanical properties depending on the direction in which the forces are applied. Its ability to resist cracking and further damage was also demonstrated, which is very impressive.

It is the complex behavior and properties of bone that make it suitable for absorbing cyclic loads during activities of daily living, such as walking, running, and other weight-bearing movements (speaking specifically about the human femur).

At the same time, this is a challenge in terms of producing and manufacturing materials and implants that represent these exact mechanical properties. Nevertheless, in the modern era, the field of biomaterials and artificial implants is considered very advanced, regarding the representation of the mechanical properties of the bone, providing a long-term and quality life to the patients.

The development of the production of implants is certainly based on conducting experiments that evaluate their quality and reliability, using biomechanical sensors and optical methods. This requires knowledge of the mechanical properties of bone, to conduct complete and correct experimental procedures.

3.2 Biomaterials

Orthopedic biomaterials are incredibly effective at giving millions of people each year their mobility and quality of life back. Orthopedic biomaterials have been a

resounding success on the global market, with sales of these materials reaching over 24 billion dollars in 2007 and expected annual growth rates of 7-9%. Spending on biomaterials for knee and hip joint replacements totaled 10 billion dollars in 2007.

In general, only materials that can sustain cyclic load-bearing applications are suitable for use as orthopedic biomaterials. Even though metals, polymers, and ceramics are used in orthopedics, metals have remained the only material type that has consistently provided the right material properties over time, including high strength, ductility, fracture toughness, hardness, corrosion resistance, formability, and biocompatibility, which are essential for the majority of loadbearing roles in total joint arthroplasty [51].

3.2.1 Polymers

Polymers are most frequently employed as the articulating bearing surfaces of joint replacements and as an interpositional cement between the implant surface and bone.

When they are used as articulated surfaces, they must have a low coefficient of friction, and low wear rates when they come into contact with the opposing surface, which is often constructed of metal. Figure 54, presents an articulated surface implant made of a polymer, which is placed between the acetabular cup and the head of the femoral stem (**Figure 55**).

Polymers have specific mechanical properties and are capable of being shaped and hardened inside the body. For this reason, they can be used as a means of connecting the implant component and the bone tissue. The first polymer used for this purpose was called polymethylmethacrylate (PMMA), which was borrowed from the field of dentistry. PMMA became popular thanks to the work of Charnley.

In general, when it comes to polymers used in orthopedics, certain mechanical properties are crucial. These properties include yield stress (the point where deformation sets in), creep resistance (ability to withstand long-term stress), and wear rate (how much it wears down over time). These properties are influenced by factors like the structure of the polymer's molecular chains, the molecular weight, and whether chains are branched or linear [51].

Figure 54: *Articulated surface implant component made of a polymer. Its purpose is to create good adhesion between the acetabular cup and the head of the femoral stem* **[51]** *(edited).*

Figure 55*: Examples of three types of bearing couples used in modern total hip arthroplasty. 1) metal-on-polymer. 2) ceramic-on-ceramic 3) metal-on-metal* **[51]** *(edited).*

3.2.2 Ceramics

Ceramics have become more and more significant in implants during the past few years. They are largely biocompatible due to their chemical stability and ionic connections. In 2003, the FDA granted its initial approval for the first ceramic-on-ceramic hip implant. Although ceramic implants have been used for a long time ago. The greater wear resistance of ceramics is one of the benefits over metal-metal and meta-polymer implants. They also have enhanced properties like high rigidity, reduced friction, and resistance to further oxidation.

Additionally, the two main bulk parameters governing the mechanical properties of ceramics are the tiny grain size and density. Any voids in the body of ceramic will raise stress and deteriorate its mechanical properties. The extent of the internal strains brought on by cooling-induced thermal contractions is determined by grain size. Such thermal contraction stresses are crucial in ceramics because they cannot be eliminated through plastic deformation as they can in ductile materials.

Orthopedic THA has been using alumina and zirconia ceramics for many years. Pierre Boutin implanted the first couple (alumina-alumina) in 1970 [51]. The second implant (2) in **Figure 55** presents a ceramic-on-ceramic implant.

3.2.3 Metals

Modern total hip arthroplasties continue to use metals as their primary material. Metals offer the right material properties, including high strength, ductility, fracture toughness, hardness, corrosion resistance, formability, and biocompatibility required for usage in load-bearing roles required in total joint arthroplasties. The metals are much stronger and stiffer than bone tissue. However, in some cases, fatigue failures occurred due to size and design limitations [51].

In orthopedics, and especially in total joint replacement, there are three main metal alloys:

1) Titanium-based alloys
2) Cobalt-based alloys
3) Iron-(stainless steel) based alloys

The choice of alloy for a specific application or implant component is usually based on its strength, flexibility, and hardness. However, the primary reason for the widespread use of all three alloys as load-bearing implant materials is their excellent corrosion resistance [51].

Stainless Steel Alloys

In orthopedics, the first metals utilized were stainless steel in 1926. Iron and carbon are the two main components of steels, and they occasionally also include chromium, nickel, and molybdenum. There are additional traces of manganese, phosphorus, sulfur, and silicon. Through modifications to the steel's microstructure, carbon, and the other alloying elements influence the material's mechanical properties. Stainless steels do have greater ductility, as evidenced quantitatively by a three-fold greater "percentage of elongation at fracture" when compared to other implant metals, despite having mechanical properties that are generally less desirable than those of the other implant alloys (lower strength and corrosion resistance).

Cobalt-Chromium Alloys

Out of the many available Cobalt-Chromium alloys, there are two mainly used as implant materials:

1) Cobalt-Chromium-Molybdenum (CoCrMo)
2) Cobalt-Nickel-Chromium-Molybdenum (CoNiCrMo)

There are also other cobalt alloys approved for implants, including one that contains tungsten (CoCrNiW) and another with iron (CoNiCrMoWFe). Cobalt-Nickel-Chromium-Molybdenum alloys, with high nickel content (25-37%) promise improved corrosion resistance, but they also raise questions about potential nickel release toxicity and/or immunogenic reactivity. Because cobalt alloys are prone to work-hardening at room temperature, they are often cast into their final shape [51].

Titanium Alloys

In the mid-1940s, titanium alloys were developed for the aviation industry and were later used in orthopedics. While commercially pure titanium (CPTi) has better corrosion resistance and ductility than titanium alloys, joint replacement components are made of Ti alloys (specifically Ti-6Al-4V) due to their superior mechanical properties. Ti alloys are especially suitable for hip replacement components because they have higher corrosion resistance compared to stainless steel and Co-Cr-Mo. Generally, Ti-6Al-4V surpasses stainless steel in mechanical properties, with a lower flexural rigidity, and is closer to the bone in terms of torsional and axial stiffness. This

means that Ti alloys theoretically cause less stress shielding than cobalt and steel alloys. However, titanium alloys are particularly sensitive to certain geometric factors, especially notch sensitivity. This reduces the effective strength of a component by making it more prone to cracks initiating and spreading throughout the material. Therefore, both the design geometry and fabrication of Ti alloy components need to be carefully considered.

One significant drawback of Ti alloys is their relative softness compared to Co-Cr-Mo alloys, along with their poorer wear and frictional properties. Ti-6Al-4V is over 15% softer than Co-Cr-Mo alloy and tends to experience more wear when used in applications involving articulation, such as total knee arthroplasty or hip replacement femoral heads. As a result, Ti alloys are rarely used in situations where hardness or resistance to wear is the primary concern [51].

3.2.4 Synopsis of Orthopedic Biomaterials' Mechanical Properties

In the previous subsections, they presented in short brief the three most dominant biomaterials in the market. These materials have different mechanical properties and for this reason, they are used in different cases. The following table (Table 5: *The mechanical properties of the most dominant biomaterials in the market compared to those of cortical bone. The mechanical properties of cortical bone are generalized due to its anisotropic material behavior, as was analyzed in subsection 3.1.1. ASTM stands for American Society for Testing and Materials. Where* (C) *and* (T) *compression and tension respectively* [51] *(edited).*) shows the most common uses of these materials in orthopedics.

Table 6, contains the mechanical properties of all the categories of materials that were analyzed in the previous subsections. The main purpose of the long bones in the lower body is to support weight as load-bearing structures, meaning they are constantly subjected to loads [51]. It is observed that the metals have higher hardness, fatigue strength, and yield strength, compared to the ceramics and polymers, therefore they are suitable to be used as total joint replacement components, according to Table 6.

The very low friction of ceramics makes them suitable for use as load-bearing surfaces in total joint arthroplasty (Table 5: *The mechanical properties of the most dominant biomaterials in the market compared to those of cortical bone. The mechanical properties of cortical bone are generalized due to its anisotropic material behavior, as was analyzed in subsection 3.1.1. ASTM stands for American Society for*

Testing and Materials. Where (C) *and* (T) *compression and tension respectively* [51] *(edited).*), for example, acetabular cups and femoral heads.

The polymers can be shaped and hardened inside the body, thus they can be used as low friction inserts for bearing surfaces in total joint arthroplasty, as it was presented in subsection 3.2.1, or as bone cement for the connection of implant and the bone tissue (**Table 5**: *The mechanical properties of the most dominant biomaterials in the market compared to those of cortical bone. The mechanical properties of cortical bone are generalized due to its anisotropic material behavior, as was analyzed in subsection 3.1.1. ASTM stands for American Society for Testing and Materials. Where* (C) *and* (T) *compression and tension respectively* [51] *(edited).*).

Table 4: *Primary use of the most dominant biomaterials in the market* [51] *(edited).*

MATERIAL	PRIMARY USE
Metals	
Ti alloy (Ti-6%Al-4%V)	Plates, screws, TJA components (non-bearing surface)
Co-Cr-Mo alloy	TJA components
Stainless steel	TJA components, screws, plates, cabling
Polymers	
Polymethylmethacrylate (PMMA)	Bone cement
Ultra-high molecular weight polyethylene (UHMWPE)	Low friction inserts for bearing surfaces in TJA
Ceramics	
Alumina (Al_2O_3)	Bearing surface TJA components
Zirconia (ZrO_2)	Bearing surface TJA components

Table 5: *The mechanical properties of the most dominant biomaterials in the market compared to those of cortical bone. The mechanical properties of cortical bone are generalized due to its anisotropic material behavior, as was analyzed in subsection 3.1.1. ASTM stands for American Society for Testing and Materials. Where (C) and (T) compression and tension respectively [51] (edited).*

Orthopedic Biomaterial	ASTM Designation	Elastic Modulus (Gpa)	Yield Strength (Gpa)	Ultimate Strength (Gpa)	Fatigue Strength (Mpa)
Cortical Bone					
Low Strain	-	15.2	114 (T)	150 (C) / 90 (T)	30-45
High Strain	-	40.8	-	400 (C) / 270 (T)	-
Polymers					
UHMWPE	-	0.5-1.3	20-30	30-40 (T)	13-20
PMMA	-	1.8-3.3	35-70	38-80 (T)	19-39
Metals					
Stainless Steel	ASTM F138	190	792	930 (T)	241-820
Co-Cr Alloys					
	ASTM F75	210-253	448-841	655-1277 (T)	207-950
	ASTM F90	210	448-1606	1896 (T)	586-1220
	ASTM F562	200-230	300-2000	800-2068 (T)	340-520
	ASTM 1537	200-300	960	1300 (T)	200-300
Ti Alloys					
CPTi	ASTM F67	110	485	760 (T)	300
Ti-6Al-4V	ASTM 136	116	897-1034	965-1103 (T)	310

3.3 Design Requirements for Hip Implants

The implant design process is extremely important to the success of total hip arthroplasty and includes various requirements for the geometry, the physical dimensions, and the material of the implant. For example, studies have shown that the geometry and the length of the femoral stem's neck affect the fatigue strength of the implant [52]. Also, the length of the implant affects the load transfer and the shape of the implant changes the distribution of strains [46], [53], [54].

At the same time, great attention should be paid to the material that will be used for the construction of the implant, because it is a very important factor in determining the stress-shielding [46], [54]. Stress shielding can have positive and negative effects at the same time. On the one hand, the implant's material usually is stiffer than the bone tissue, thus a large fraction of the load is carried by the implant decreasing the amount of pressure that is transferred to the bone tissue. As a result, the bone tissue is protected in the presence of excessive loads. On the other hand, because the bone receives less stress, atrophy, and weakening of the bone tissue can occur, resulting in implant failure due to loosening.

More specific requirements about hip implant design are:

1) The materials that are used to manufacture hip implants, need to have high biocompatibility with tissues and bone, sufficient mechanical strength, low friction and high wear resistance, and fracture toughness [55].

2) The design of the implants needs to have a sufficient range of motion to cover patients' daily movements, such as standing/sitting, etc. [55].

3) The hip implant must have the ability to withstand multiple and complex stresses that occur during movements (climbing stairs, etc.) [55].

4) The most important requirement for hip implants is their evaluation. All implants designed and manufactured, no matter how well adapted to the above requirements are, should always be evaluated using various tests, before being used. Such tests may include monitoring their strains under load using biomechanical sensors (strain gauges, Fiber Bragg Grating Sensors, etc.), optical methods (digital image correlation), and/or even numerical simulations.

3.4 Manufacturing Techniques of Hip Implants

Hip implants as well as some certain artificial parts for biomedical applications have a significant impact on the quality of life of patients with hip joint diseases or injuries. Many manufacturing techniques can guarantee accuracy, longevity, and patient-specific personalization which are necessary factors for the long-term results of total hip arthroplasty.

There are several manufacturing techniques for hip implants and medical objects, which are divided into two categories, "Casting" and "Powder Metallurgy", as will be presented below. The choice of technique when it comes to the manufacture of an implant is determined according to the type and shape of the implant, the material that

is going to be used, and the desired biomechanical outcome. The "Powder Metallurgy" category is also divided into two other subcategories "Conventional Processes" and "Additive Manufacturing".

In particular, nowadays, techniques involving additive manufacturing have taken the center of attention in the implant industry as they offer more advantages than casting techniques.

In the following table (**Σφάλμα! Το αρχείο προέλευσης της αναφοράς δεν βρέθηκε.**), the techniques belonging to each of the two categories mentioned above are presented. Some of these techniques that are mentioned in the table are analyzed below with information and explanations about their procedure.

Table 6: *Manufacturing techniques for implants and medical components* **[56]** *(edited)*.

MANUFACTURING TECHNIQUES		
CASTING	**POWDER METALLURGY**	
Vacuum Arc Remelting (VAR)	**CONVENTIONAL PROCESSES**	**ADDITIVE MANUFACTURING**
Vacuum Induction Melting (VIM)	Conventional Sintering (CS)	Selective Laser Sintering (SLS)
Electron Beam Melting (EBM)	Self-propagating High Temperature Synthesis (SHS)	Selective Laser Melting (SLM)
-	Hot Isostatic Pressing (HIP)	Laser Engineered Net Shaping (LENS)
-	Spark Plasma Sintering (SPS)	Electron Beam Melting (EBM)
-	Metal Injection Molding (MIM)	-

3.4.1 Casting

The casting procedures are fundamental methods that support the production of custom components for a range of applications in the field of biomechanics. Casting procedures involve pouring molten metal into molds to create specific shapes and forms as the metal solidifies. Some of the casting techniques are VAR and VIM and they are used to process materials especially metal alloys to satisfy demanding specifications.

3.4.1.1 Vacuum Induction Melting

The procedure is carried out in a chamber under a vacuum or an inert gas atmosphere to reduce the chances of contamination. An induction coil is located inside the vacuum chamber and is typically wound around a crucible that contains the processing material. The crucible is typically made of graphite due to easy handling, inexpensiveness, and high melting point (similar to that of diamond, approximately 3600 °C). Alternating current flows through the coil when an AC power supply connects to its edges. The alternating current causes periodic changes in the magnetic field of the coil. The changing magnetic field penetrates the processing material and generates electric currents within the material. These electric currents are also called eddy currents. As they circulate inside the material, they encounter resistance and this resistance leads to the conversion of electrical energy into heat. The material is then melted and poured into the mold [56], [57], [58], [59]. Figure (**Figure 56**) shows a setup for VIM processing of NiTi (Nitinol, a shape memory alloy). However, some materials and alloys that are processed by this technique (like NiTi – a shape memory alloy) are not acceptable for medical applications and they need further processing, like hot working, surface treatments, machining, etc.
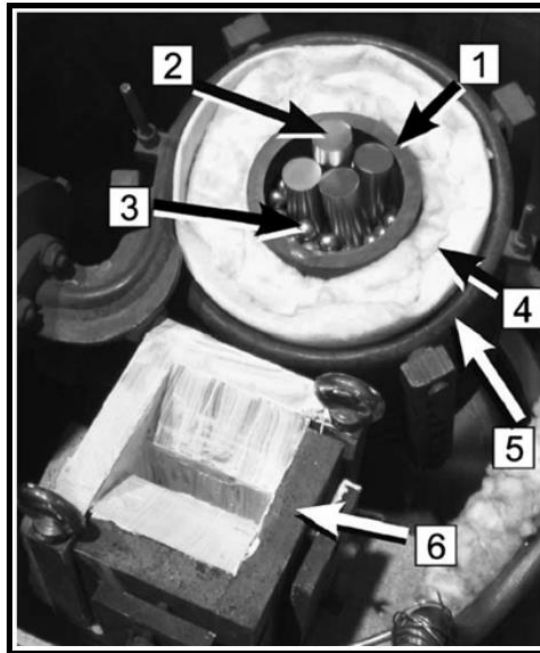
Figure 56: *Lab equipment setup for VIM processing of NiTi (Nitinol). (1) A crucible made of graphite – (2) Titanium rods – (3) Nickel pellets – (4) Isolation – (5) a coil made of copper –(6) a mold with the desirable shape of the processing material that is wanted* **[56]** *(edited).*

3.4.1.2 Vacuum Arc Remelting

The VAR technique is implemented in a vacuum chamber or an inert gas atmosphere like the VIM technique. The use of a crucible is not necessary for this process. It is divided into two categories based on the type of electrode used. The first category includes a non-consumable electrode that does not melt during the process. The second category includes a consumable electrode, which is made of the same material that is to be melted and processed. The procedure is as follows:

The materials to be processed are fitted onto a conductive hearth, which also often represents the mold (usually the hearth is made of copper). The electrode is then placed over the hearth and the materials. A high voltage is applied between the electrode tip and the conductive hearth. This voltage creates a strong electric field in the gap between the electrode and the hearth, producing an electric arc. The electric arc generates heat and the material melts. In the case where a consumable electrode is used, the electrode slowly melts over time and mixes with the rest of the material. At the end of the process, the material is turned over and the whole process is performed again from the beginning. This procedure can be repeated several times. The reason for this is that a single application of the technique does not create a homogeneous material and the process needs to be repeated [56], [60]. A schematic of a vacuum arc remelting unit is

shown in Figure (**Figure 57**) below. Materials and alloys processed by the VAR technique require further processing like the VIM technique.
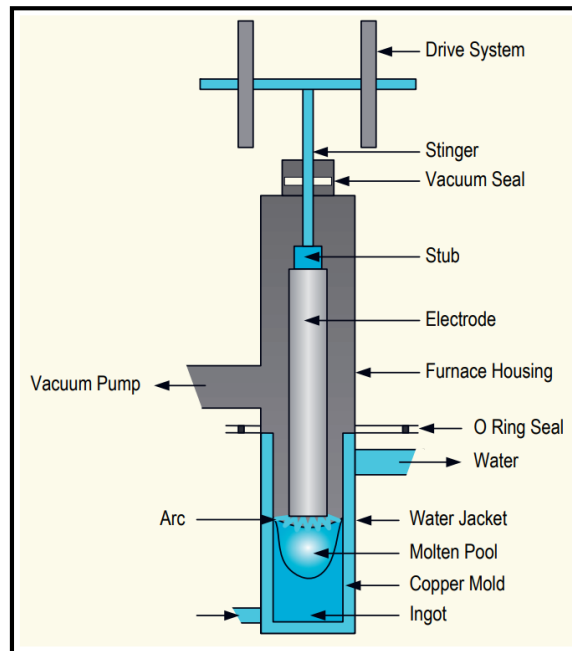
Figure 57: *Schematic of a vacuum arc remelting unit* **[61]** *(edited).*

3.4.2 Powder Metallurgy

In contrast to casting techniques, powder metallurgy involves the processing of powders from metals and alloys. The production of powders can be done by many rapid solidification (RP) techniques such as atomization (water, gas, plasma) and rotating electrodes. They can also be used different ways than rapid solidification techniques such as chemical reactions to produce metal and alloy powders. The process of powder metallurgy allows materials to attain more elevated alloy compositions without experiencing the issue of segregation [56].

A special category of powder metallurgy contains Additive Manufacturing technologies, the most advanced and widespread techniques nowadays. Additive Manufacturing (AM), also known as Rapid Prototyping (RP), is the process of creating an object layer-by-layer. They require a three-dimensional computer-aided design that describes the geometry and the exact dimensions of the object. Because of this layer-by-layer technology, AM techniques can create objects with very complex shapes and geometries without needing any other assistance (like cutting tools, etc.). They also can control the percentage of porosity within the components that are manufactured, as a result, heavy metals or alloys that have double the weight of cortical tissue (for example titanium) can be used to produce biomedical implants. The implant is necessary to

weigh approximately the same as the bone tissue that is going to be replaced, that's why the metal/alloy implants must have high percentages of porosity [56].

In general, the implants that are manufactured with AM techniques have shown superior mechanical properties than those that have been made by casting techniques. Implants can meet the desired mechanical behavior similar to that of cortical bone, eliminating the effect of stress-shielding and acquiring long-term results [56].

3.4.2.1 Conventional Sintering (CS)

In this technique, at first, mechanical pressure is used to compact metal or alloy powders into the appropriate shape. A loosely held-together arrangement of particles called a "green" compact, which resembles the ultimate shape of the object, is created during this compacting process. The term "green" in powder metallurgy declares that it "is not yet fully processed" [62]. Next, the green compact is heated to a temperature that is below the material's melting point but high enough for atomic diffusion to take place. During the heating phase, the particles start to bond together as atoms move across the particle surfaces and form interparticle bonds, resulting in a solid structure. After the bonding, the material is left to cool down.

The conventional sintering method has a downside in that it requires long periods for the heating phase to be completed. Additionally, this method has limitations when it comes to shaping the samples and controlling the size of pores within the material [56].

However, the conventional sintering technique offers many advantages. For instance, low-cost production of components can be applied to a diverse range of materials and eliminates the need for further processing [56].

3.4.2.2 Hot Isostatic Pressing (HIP)

The HIP technique is similar to that of conventional sintering with the only difference being the extra pressure that is applied during the implementation of this technique. The process is the same as conventional sintering. A green compact is first created by metal or alloy powders using mechanical pressure and then heated to a temperature that does not exceed the melting point but is high enough to cause atomic diffusion. At the same time, high pressure is applied to the compact eliminating the voids/pores within the material. This results in a denser component with good mechanical properties [56], [63].

3.4.2.3 Selective Laser Sintering (SLS)

SLS is a well-known additive manufacturing or 3D printing process that involves layer-by-layer selective sintering of powdered material, using a high-powered laser. The construction of a 3D model of the desired object is the first step in the process. CAD software is frequently used to create 3D models. The setup of SLS has two chambers. The first one contains the powder while the second one is initially empty and is called the "bed". Above the chambers, there is a component called the "roller" that spreads uniformly the powder on the "bed". There are two components at the top of the system, a laser and a computer-controlled scanning system that monitors the laser's energy. Before the process begins, both of the chambers are preheated. The first layer of powder is spread by the "roller" on the "bed", then the laser sinters the powder making all particles bond with each other, creating a solid layer. Next the "bed" descends to a predetermined depth, the "roller" spreads the next layer and the process starts over. This keeps going on until the object is fully constructed. A schematic diagram of the SLS components is presented in Figure (**Figure 58**).

Despite its fast production of very complex geometrical objects, SLS is a very expensive technique due to the high-powered laser that it uses. It is also limited to the type of material used, which must always be in powder form, and the surface of the finished material needs further processing (e.g. polished) [56], [64].
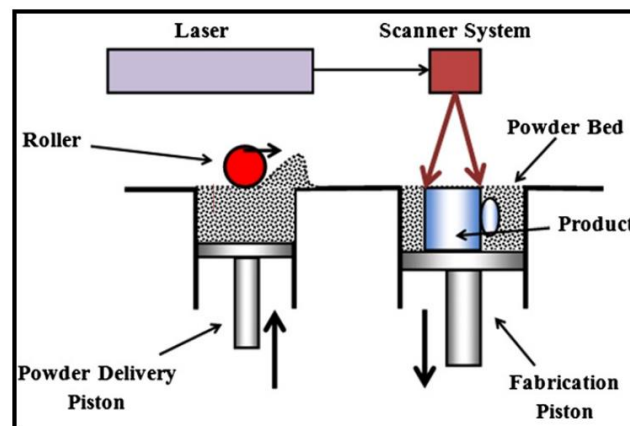
Figure 58: *Schematic diagram of the SLS system* [56] *(edited)*.

3.4.2.4 Laser Engineered Net Shaping

The LENS technique uses a laser to melt and fuse metal powders layer by layer to create metal components. The process begins with the construction of a 3D computer-aided design (CAD) as all the AM techniques do. Two nozzles at the lateral sides of the laser deliver a specific amount of powder to the build area. A thin layer of powder is

spread over the work surface and the laser beam is directed onto the powder. The heat generated by the laser melts the powder particles, causing them to fuse. The process repeats until the object is fully constructed. An inert gas is also used to shield the melting material from oxygen. It can produce components with high density with good mechanical properties. However, it is not cost-effective as it requires a lot of energy [56]. Figure (**Figure 59**) presents the schematic diagram of a LENS system.
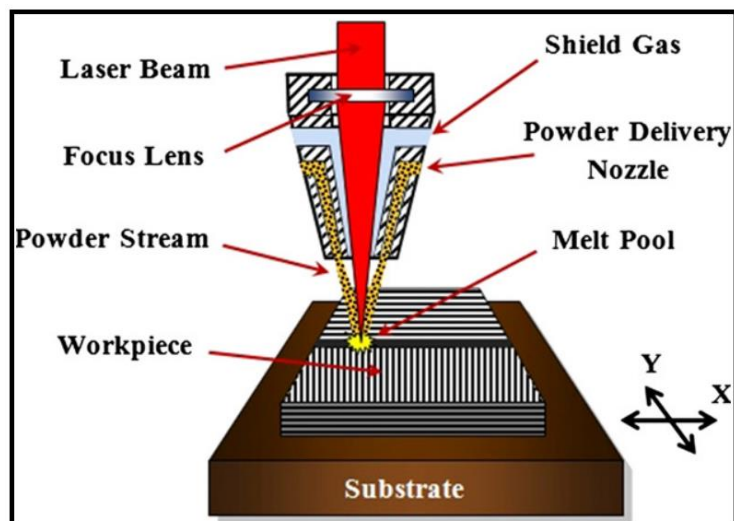
Figure 59: *Schematic diagram of a LENS system* **[56]** *(edited)*.

3.5 Stress-Shielding Effect

Bone tissue is a piezoelectric material, which generates electrical charges when mechanical pressure is applied to it. There is a special cell called osteoblast that is found in bone tissue. Osteoblasts are responsible for bone growth and remodeling [65]. The osteoblasts are stimulated by the generated electrical charges and they improve bone formation [66], [67]. Additionally, many studies have been conducted to examine the piezoelectric effect (PE), which has shown that it enhances the growth of bone tissue and at the same time reduces its resorption [68].

Stress-shielding effect (SSE) is one of the most challenging problems in total hip arthroplasty and influences the frequency of the piezoelectric effect's occurrence in bone tissue. Here is how the stress-shielding effect is connected with the PE:

As was mentioned in subsection 3.2, metals are the most commonly used materials in total hip arthroplasty, because they exhibit good mechanical properties, thus, they can sustain cyclic load-bearing applications.

However, according to Σφάλμα! Το αρχείο προέλευσης της αναφοράς δεν βρέθηκε., the metals exhibit much higher Young's modulus (stiffness) than the bone tissue. Specifically, the Young's modulus of cortical and trabecular bone ranges from 3 to 30

GPa and 0.02 to 2 GPa, respectively [69]. A key principle of solid mechanics is that when two materials join, the one with the higher stiffness carries most of the load [70], meaning that implants made of metals can cause load distribution problems in total hip arthroplasty. Therefore, because the implant receives the greatest load, not enough pressure is transferred to the bone tissue (stress-shielding) to activate the piezoelectric effect and thus the osteoblasts are not stimulated as much as they should be.

The appearance of the phenomenon of stress-shielding for a long time can cause bone atrophy, which can further lead to implant failure.

3.5.1 Factors that Promote the Stress-Shielding Phenomenon

Above, it was mentioned that the large difference in stiffness between a metal implant and bone tissue leads to the phenomenon of stress-shielding. Nevertheless, the interplay of various factors within this context can trigger the occurrence of stress-shielding, potentially giving rise to serious clinical complications. The following table provides an overview of these contributing factors, setting the stage for a subsequent analysis of the specific outcomes they can precipitate. By exploring these factors, we can gain a deeper understanding of the intricacies involved in stress-shielding and its impact on the integrity and longevity of implant-bone systems.

Table 7: *Factors Contributing to Stress-Shielding* **[70].**

STRESS-SHIELDING FACTORS	
FACTORS	**DESCRIPTION**
Implants' materials	As it was explained previously in this subsection, some materials especially metals and their alloys exhibit very high Young's modulus, affecting the load distribution in the femur and causing stress-shielding effects that lead to bone atrophy.
Metaphyseal filling and implant size	The metaphyseal filling, in the context of an implant, refers to the extent to which the implant extends into the metaphyseal region of the femur. These very long implants cover a very large area of the bone, as a result, they bear the most load leading to stress-shielding effects. In a few words,

	greater stem size leads to an escalation in bone resorption [70].
Porous coating level	Porous coating is usually applied to a small area of an implant, promoting bone ingrowth and integration, which helps to transfer loads more effectively from the implant to the bone. However, if the porous coating covers a very large surface on the implant (extensive porous coating) can alter the load distribution leading to stress-shielding effect.
The bone-implant interface	The connection between the implant and the bone is crucial. If this interface lacks stability or proper integration, it can lead to micromotions, and load distribution problems, resulting in stress-shielding effect.
Geometry of implants	The geometry of the stems plays a crucial role because it determines how forces are transmitted and distributed through the implant and into the bone. An inappropriate stem design can lead to stress-shielding effect.

Some complications and problems created by stress-shielding are:

The reduction in bone strength near the implant location elevates the likelihood of stem loosening, periprosthetic fractures and may lead to avulsion fractures of prominent bone structures such as the trochanters. Removing a firmly anchored implant from bone significantly affected by stress-shielding presents technical complexities and could potentially result in insufficient bone remaining to adequately support a replacement implant. Furthermore, stress-shielding has the potential to prompt a higher level of intracortical porosity within the bone, rendering it more vulnerable to the infiltration of tine wear particles. This infiltration, in turn, can worsen bone loss through a process known as osteolysis. Consequently, bone subjected to stress-shielding may experience reduced density and increased fragility, amplifying the risk of fractures and related complications [69], [70].

3.5.2 Managing Stress-Shielding

Based on the above, the following should be done to reduce/prevent the SSE :

1) **Manufacturing Specifications** – Addressing the problem begins at the very start of the total hip arthroplasty process, which is the manufacture of the implants. The

implants must have specific characteristics, which will prevent the appearance of the stress-shielding effect.

2) **Evaluation** – Beyond the specific characteristics of the implants, their mechanical behavior should be evaluated, through various numerical simulations and in vitro tests.

3) **Detection** – Despite the careful construction and mechanical evaluation of the implants, after their placement, the health of the surrounding bone tissue should be gradually checked to detect any problem.

3.5.2.1 Manufacturing Specifications

For the manufacture of implants, attention should be paid to their geometry, their material, their size, and their contact surface with the bone. Furthermore, if the implant is heavier than the bone tissue that was removed, it must be adjusted to ensure an equivalent weight, without of course reducing its volume. One way to achieve this objective is by controlling the percentage of porosity within the material, using additive manufacturing techniques, as mentioned in the previous section. The porosity connects with the mass (Weight) as follows:

- Porosity (p) is a measure of the amount of voids, pores, or empty spaces within a material.

- When porosity increases, it means that a significant portion of the implant's volume (v) consists of empty spaces or pores. The more spaces, the less mass (m) the material has.

In addition to weight control, the implants need to exhibit a certain elastic modulus (stiffness), so the load can be transferred properly from the implant to the bone tissue. One way to achieve this is again by controlling the porosity of the material. Many studies have been conducted to create a formula that presents the Young's modulus (stiffness) of porous materials as a function of porosity [71], [72], [73]. Some studies have concluded that the Young's modulus can be decreased by increasing the percentage of porosity [71], [74].

Considering all the above, it is possible to manufacture exceptional implants that effectively mitigate the stress-shielding phenomenon, by controlling the material's porosity.

3.5.2.2 Evaluation

After the implant manufacturing process, the next crucial step involves a comprehensive mechanical evaluation through various tests to ensure the prevention of

the stress-shielding effect. In vitro experiments represent the most common and dependable approach, enabling a comprehensive assessment of the entire implant-bone system.

In a study examining the stress-shielding phenomenon in lumbar interbody fusion devices, the suggested methodology involves subjecting the implant-bone system to a series of stress tests, encompassing compression, torsion, flexion, and lateral bending [75]. These tests provide information about the stress and the implant's stiffness. This complete evaluation offers a thorough understanding of whether the implant has the necessary mechanical properties, avoiding the stress-shielding effect.

3.5.2.3 Detection

Following the implant's production and placement, it is imperative to periodically monitor the condition of the adjacent bone tissue. A highly effective technique for assessing bone health is the use of dual-energy X-rays (DEXA), which possess the capability to quantify bone density. Therefore, in the event of any latent issues arising from stress-shielding, employing DEXA to measure bone density ensures timely detection and prevention of potential complications.

4. ANALYSIS OF BIOMECHANICAL SENSORS AND OPTICAL TECHNIQUES FOR BIOMECHANICAL APPLICATIONS

Total hip arthroplasty has proved effective in enhancing the quality of life for many people throughout the world, but to guarantee the best long-term results and patient satisfaction, it is crucial to evaluate the performance of the implant-bone system.

Biomechanical sensors and optical techniques are indispensable equipment for this evaluation, as engineers and researchers can assess the strain distribution, implant stability, and overall biomechanical performance according to the real-time information

these tools provide. The most common sensors for these type of tests are electrical resistance strain gauges (SGs), fiber Bragg grating sensors (FBGSs), linear variable differential transducers (LVDT), and digital image correlation (DIC).

Certain knowledge about their working principles is essential for the proper monitoring of strains or internal movements of the implant. Engineers and researchers may better understand the biomechanics of total hip arthroplasty and improve patient outcomes, implant durability, and overall quality of life by utilizing the potential of these cutting-edge sensor devices.

4.1 Strain Gauges

Strain gauges are mainly used to measure the strains on a material that is under load. For a better understanding of strains, an example will be given. Suppose there is a material that is subjected to tension by a force F (**Figure 60**). Due to the deformations, the material extends to a distance ΔL. The strain is calculated according to the following equation:

$$\varepsilon_{long} = \frac{\Delta L}{L}$$
<div align="right">**Equation 2**</div>

, where L is the original size of the material. In other words, strain is the ratio of the change in length of the material to the original and unaffected length [76], [77], [78].
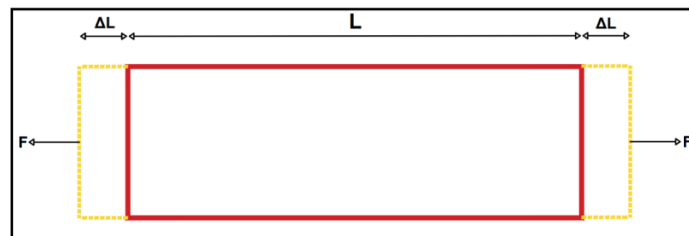
Figure 60: *A hypothetical material under tension which was used as an example for the explanation of strains.*

The type of strain that **Equation 2** calculates refers to longitudinal strains. There are other types of strains such as lateral, shear, and volumetric, and each of them has a different calculating equation. Specifically:

- **Shear strain (ε_{shear})** – Occurs when two opposite faces of an object slide past each other, resulting in distortion of the object (**Figure 61**). The equation that calculates the shear strain is as follows [79]:

$$\boldsymbol{\varepsilon_{shear}} = \tan(\boldsymbol{\theta}) \rightarrow \boldsymbol{\varepsilon_{shear}} = \frac{\boldsymbol{\Delta_x}}{\boldsymbol{L}} \qquad\qquad \textbf{Equation 3}$$

, where $\boldsymbol{\Delta_x}$ is the length of the deformation at its maximum value, and $\boldsymbol{L}$ is the perpendicular length of the object.
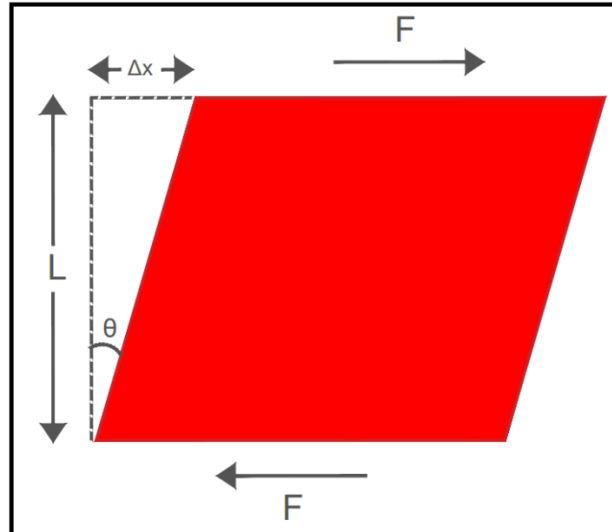
Figure 61: *Representation of an object that has undergone a shear strain.*

- **Volumetric strain** ($\boldsymbol{\varepsilon_{vol}}$) – Is the alteration in volume that an object goes through as a result of compressive or tensile forces. Volumetric strain is defined as the ratio of the object's volume change to its original volume. The equation that describes this is as follows [80]:

$$\boldsymbol{\varepsilon_{vol}} = \frac{\boldsymbol{\Delta V}}{\boldsymbol{V}} \qquad\qquad \textbf{Equation 4}$$

- **Lateral strain** ($\boldsymbol{\varepsilon_{lateral}}$) – Also known as transverse strain, is defined as the ratio of change in lateral dimensions to original lateral dimensions. When an object experiences longitudinal strain due to compressive or tensile forces, it also experiences lateral strain. Poisson's ratio ($\boldsymbol{v}$) describes how an object responds in the lateral direction when experiences longitudinal strain. Thus the calculation of lateral strain is derived from Poisson's formula [81]:

$$v = -\frac{\varepsilon_{lateral}}{\varepsilon_{long}} \rightarrow \varepsilon_{lateral} = -v \times \varepsilon_{long} \qquad \textbf{Equation 5}$$

It can also be calculated if the change in lateral dimensions and the original lateral dimensions of the object are known according to the following equation:

$$\varepsilon_{lateral} = \frac{\Delta d}{d} \qquad \textbf{Equation 6}$$

, where $\boldsymbol{\Delta d}$ is the change in lateral dimension and $\boldsymbol{d}$ is the original lateral dimension.

Strain gauges were first used in bone biomechanics in 1944 by Gurdjian and Lissner, who connected them to a cathode-ray oscilloscope to measure the deformations of the skull at the moment of injury [82]. Since then, strain gauges have been utilized in bone biomechanics, and due to their precision and high-frequency response, they are still regarded as the gold standard in bone strain assessment [83].

4.1.1 Structure

Figure 62 presents the structural elements of a strain gauge. Strain gauges have a relatively straightforward structure, consisting of a thin metallic wire or foil organized in a specific pattern. More specifically [76], [77], [78], [84], [85]:

1) **Metallic Wire or Foil** – It serves as the strain gauge's sensing component. This part of the strain gauge is usually made of Nichrome, Constantan, Isoelastic, and Iridium-Platinum. When put under mechanical strain, these materials demonstrate a predictable change in their electrical resistance. More details about the working principles are in the next subsection.

2) **Carrier Material (Gauge Backing)** – The metallic wire or foil is attached to a carrier material. They provide mechanical support and ease of handling during installation on an object. They also protect the resistive materials of strain gauges because they usually are very sensitive and fragile. Polyimide is the standard backing material and is preferred for most applications, but other materials such as epoxy, and glass fiber-reinforced epoxy can be used as backing materials.

3) **Solder Pads** – Solder pads are used to connect the metallic wire or foil with the lead wires (soldering process).

4) **Lead Wires** – The lead wires are thin conductive wires that provide electrical connections to the strain gauge. They transmit the electrical signals from the strain gauge to the measuring instrument, such as a Wheatstone bridge.
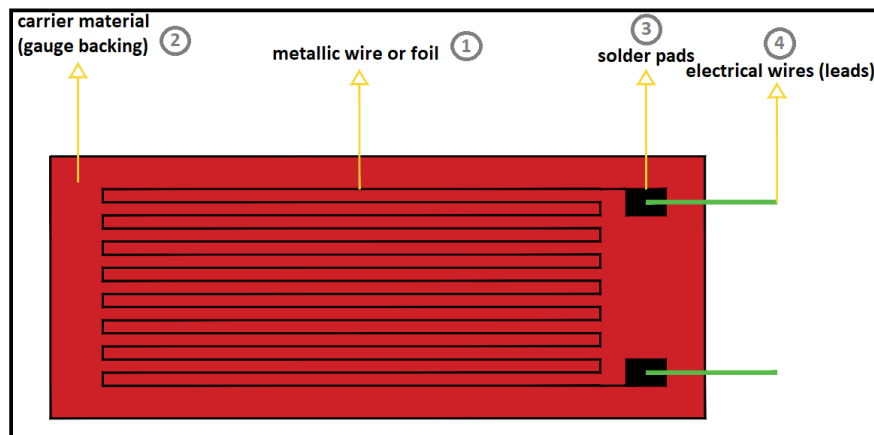
Figure 62: *This Figure illustrates the key structural elements of a strain gauge, a device widely used for measuring mechanical strains in various applications.*

4.1.2 Working Principles

The electrical resistance of a conductor, in this case, the metallic foil or wire of the strain gauge, is proportional to its length and inversely proportional to its cross-section area. The equation that describes this is as follows:

$$R = r \times \frac{L}{A}$$ **Equation 7**

, where **R** is the resistance, **r** is the resistivity, L is the length, and A is the cross-section area of the conductor. A conductor's resistivity is a property of its material that quantifies how strongly it resists the flow of electric current. The difference between resistance and resistivity is that resistivity is an inherent attribute of the material itself, while resistance is dependent on the size and form of the specific conductor. The units of measurement for resistance are ohms (Ω), while the units of measurement for resistivity are ohms-meters ($\Omega \cdot m$) [86], [87].

Suppose, there is a conductor as **Figure 63** shows, which is under tension. In this case, its length will increase and its cross-section area will decrease, resulting in an increase of the resistance R, according to **Equation 7**. On the other hand, when the

conductor is under compression, its length decreases and its cross-section area increases, resulting in a decrease of the resistance R.
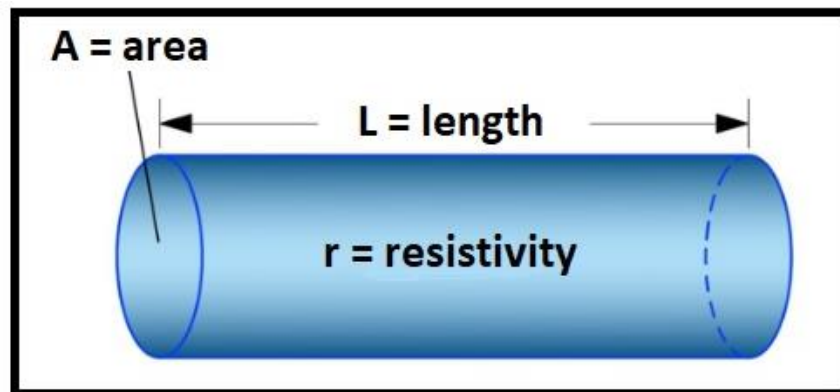
Figure 63: *The present figure shows an electrical conductor marked with the magnitudes used to calculate its electrical resistance. These magnitudes are the cross-section area, the length, and the resistivity* **[85]** *(edited).*

To extract information from the changes in resistance, the strain gauge is usually a part of a Wheatstone bridge circuit. The Wheatstone bridge circuit consists of four electrical resistors and a power source (**Figure 64**). A voltometer is also connected to points D and B to check the balance of the bridge. One of the four resistors is variable meaning that its value of resistance changes (R3), while the rest of the resistors are constant. Usually, resistors R2 and R4 are chosen to have the same resistance value. The Wheatstone Bridge has two states, the balanced and the unbalanced state.

In the balanced state, the potential difference between points D and B is zero, therefore the potential difference between points D and C is the same as the potential difference between points C and B. Now assuming that $I_1, I_2, I_3,$ and I_4 are the intensities of the currents flowing through the resistors R1, R2, R3, and R4, respectively, it follows that:

$$V_{DC} = V_{BC} \rightarrow I_2 \times R2 = I_4 \times R4 \rightarrow I_2 = I_4 \qquad \text{Equation 8}$$

With the same logic, the potential difference between points D and A is the same as the potential difference between points A and B. Thus:

$$V_{DA} = V_{AB} \rightarrow I_1 \times R1 = I_3 \times R3 \qquad \text{Equation 9}$$

Since $V_{DB} = 0$, there is no current passing through points D and B, so:

$$I_1 = I_2 = I_3 = I_4 \qquad \text{Equation 10}$$

Based on the above equations (**Equation 9**, **Equation 10**), the following result is obtained:

R3 = R1   **Equation 11**

To summarize the above, for the bridge to be in a balanced state (the potential difference between points D and B needs to be zero), it must be true that, R3 = R1 and R2 = R4.

The bridge enters the unbalanced state when there is any change in the values of the resistors, even in just one of them. Any change in the resistance values corresponds to a change in the potential difference between points D and B. By measuring this potential difference, one can derive information about the change in resistance that caused it [88].

The strain gauge is represented in the Wheatstone bridge circuit by the variable resistor. The strain gauge's electrical resistance variation modifies the bridge circuit's balance. An output voltage signal corresponding to the applied strain is produced as the bridge circuit loses balance due to the resistance change in the strain gauge. To determine the magnitude and kind of strain encountered by the object, the output voltage signal is processed and examined.
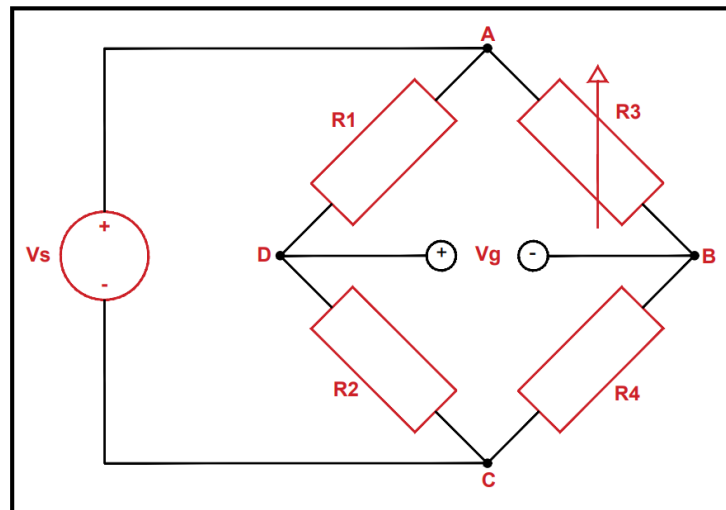
Figure 64: *The Wheatstone bridge circuit.*

The gauge factor (GF), a numerical expression of the strain gauge's sensitivity to strain, is a key parameter. The gauge factor is defined as the ratio of the fractional change in electrical resistance to the fractional change in length [89]:

$$GF = \frac{\frac{\Delta R}{R}}{\frac{\Delta L}{L}} = \frac{\frac{\Delta R}{R}}{\varepsilon}$$
<div align="right">**Equation 12**</div>

The higher the gauge factor, the more sensitive the strain gauge is to strains. **Table 8** shows the gauge factors of the most common materials that are used to construct strain gauges.

Grid Material	Composition	Gauge Factor
Nichrome	80% Ni, 20% Cr	2.0
Constantan	45% Ni, 55% Cu	2.0
Isoelastic	36% Ni, 8% Cr, 0.5% Mo, remaining Mn, Fe and Si	3.5
Iridium - Platinum	5% Ir, 95% Pt	5.10

Table 8: *Gauge factors of the most common materials that are used for the construction of strain gauges* **[77]** *(edited)*.

4.1.3 Bridge Configurations

In the previous subsection it was mentioned that the Wheatstone bridge is necessary for the transformation of the small changes in resistance of strain gauges into measurable voltage outputs. There are many bridge configurations such as quarter bridge, half bridge, and full bridge. Each of these configurations offers different advantages and is used for specific measurements.

4.1.3.1 Quarter Bridge Configuration

In a quarter bridge configuration, the circuit contains only one active strain gauge (in the place of the variable resistor), as **Figure 65** shows below.
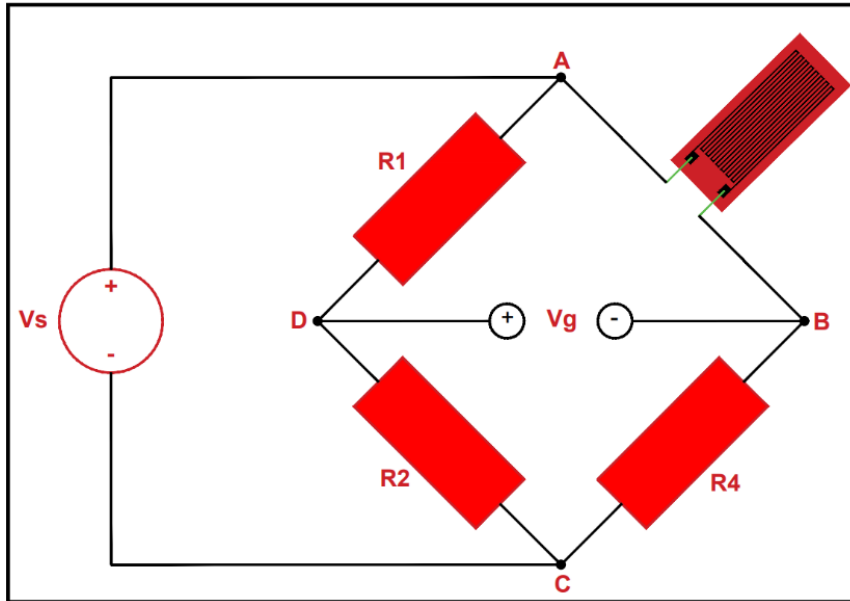
Figure 65: *Quarter bridge configuration circuit with only one strain gauge utilized. Also called simple quarter bridge.*

Since only one strain gauge is utilized, only one kind of strain can be measured. This particular configuration is also called "Simple Bridge Configuration", it is the least sensitive, and is susceptible to mistakes brought on by changes in temperature.

Many external factors and environmental conditions cause temperature changes that affect the measurements that strain gauges capture. One way to solve this problem is to add to the "Simple Bridge Configuration" system a second strain gauge, as **Figure 66** presents. The new system named "Quarter Bridge – Dummy Gauge", has one active and one inactive (dummy) strain gauge. The active strain gauge is placed and aligned according to the direction of the strains that will be measured on the object, while the "dummy" gauge is mounted to the same object but in an area that does not experience mechanical strain. If for example, the object has no strain free areas, then the "dummy" gauge can be mounted on a different object that has the same thermal characteristics as the first object. Both the active and dummy gauges encounter resistance variations when the ambient temperature changes. Since the dummy gauge is not subjected to external strain, its resistance change is primarily due to temperature. By monitoring the resistance change of the dummy gauge, the temperature effect on the Wheatstone bridge can be compensated for [85], [90], [91].
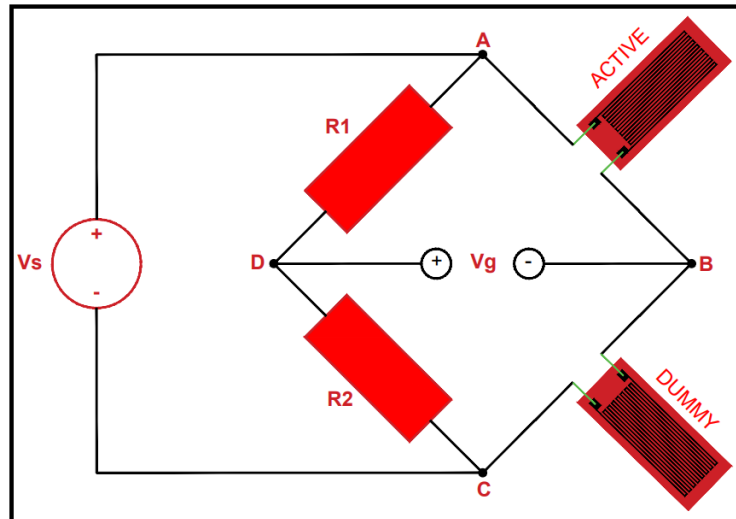
Figure 66*: Quarter bridge configuration with dummy gauge for the elimination of the temperature effects.*

4.1.3.2 Half-Bridge Configuration

Half bridge configurations contain two strain gauges that are both active, as **Figure 67** presents. These configurations are more sensitive to strains than the quarter bridge ones because there are two active strain gauges capturing strain measurements.
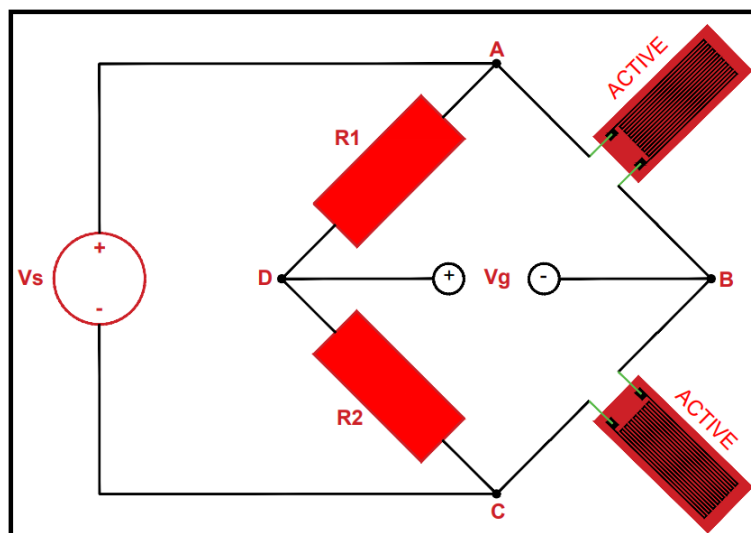
Figure 67*: Half bridge configuration circuit that contains two active strain gauges.*

There are two possible arrangements for the strain gauges in a half-bridge circuit:

1) **Half Bridge with Poisson Gauge** – In section 4.1, it was explained that when an object experiences longitudinal strains it also experiences lateral/transverse strains, and this behavior is described by the Poisson's ratio (v). Thus, this configuration contains one strain gauge transversely oriented, and another longitudinally or

axially oriented (**Figure 68**). Since this configuration can measure the changes in two axes, the number of possible resistance changes increases, and this by extension enhances the output voltage's magnitude. The temperature changes do not affect the measurements too, since it possesses the same ability as the quarter bridge configuration with the "dummy" gauge that was explained in the previous subsection.
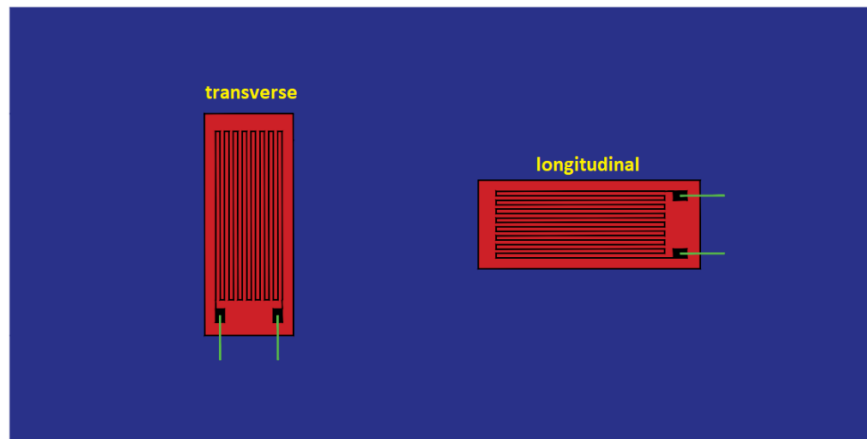
Figure 68: *Orientation for the two active strain gauges in a half-bridge configuration with Poisson gauge* [85] *(edited)*.

2) **Bending Half Bridge** – This configuration contains two active strain gauges that are mounted on an object on two opposite sites (**Figure 69**). This type can measure only bending strains with precision by eliminating the axial measured strains, thus the resistance change due to compression/tension of one strain gauge is negated by the other. Additionally, it eliminates the effect of the temperature change in the same way as it was explained previously.

Figure 69: *Placing the two active strain gauges on two opposite sites for the bending half-bridge configuration* [85] *(edited)*.

4.1.3.3 Full Bridge Configuration

A full bridge circuit utilizes active gauges in place of all resistors, making it highly versatile as it allows for various configurations involving four strain gauges (**Figure 70**). By having all resistances varying, the circuit, the circuit effectively compensates for temperature effects regardless of the chosen type of configuration.
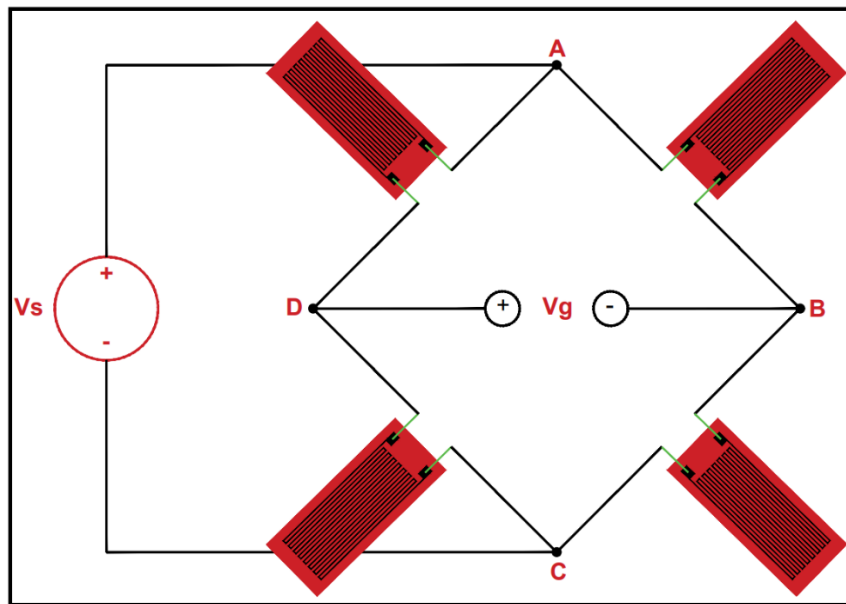
Figure 70: *Full bridge configuration circuit.*

There are many possible full bridge configurations but two of them are going to be analyzed:

1) **Axial and Bending Full Bridge** – An axial and bending full bridge involves placing all four strain gauges on one side of the structure, with an effort to keep them coplanar (Figure 71). Within the bridge, the gauge pairs on one leg are positioned perpendicularly to each other. This arrangement can be seen as two Poisson half-bridge configurations working together, leading to an output signal with double the magnitude of its half-bridge counterpart.

2) **Bending Full Bridge** – This circuit is formed by positioning the strain gauge pairs on opposite sides of the object, aligned in parallel (**Figure 72**). The bending full bridge configuration blends the features of both the Poisson half-bridge and bending half-bridge circuits. It not only eliminates axial strain but also enhances signal sensitivity. As a result, the output signal generated is twice as strong as that produced by a Poisson half bridge.
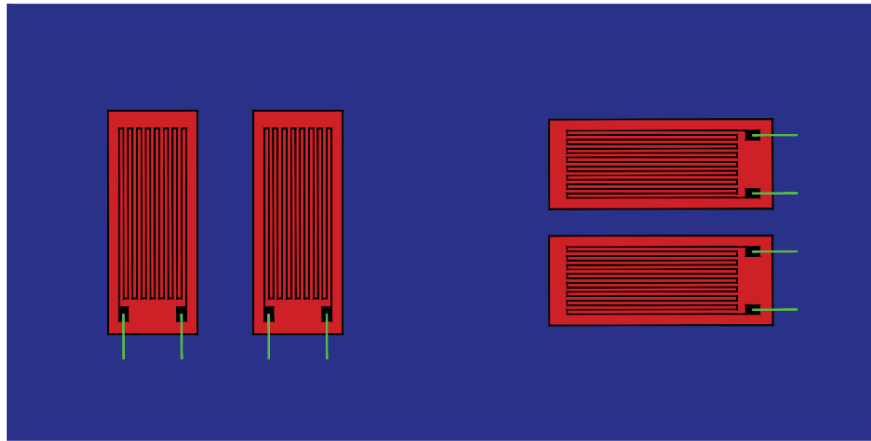
Figure 71: *Axial and bending full bridge configuration* **[85].**
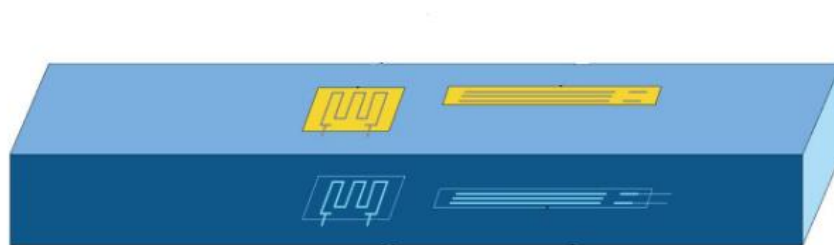
Figure 72: *Bending full bridge configuration* **[85].**

4.1.4 Types of Electrical Resistance Strain Gauges

Another way of classifying electrical resistance strain gauges in addition to bridge configurations, is the arrangement of their resistance material. The most common arrangements are as follows [85]:

1) **Linear** – Linear electrical resistance strain gauges are the most famous among the other types and are designed to assess strain in a single direction. Due to their uncomplicated design (**Figure 62**) and affordability, they are suitable for general applications, including load and fatigue testing. This type can be a part of a quarter, half, or full bridge configuration, as it was explained in the previous subsection.

2) **Tee Rosette** – This type of gauge, also known as 90° rosettes, consists of two measuring elements positioned at right angles to each other in the same carrier material (Figure 73). They find application in situations where the primary directions of strain are already identified or known. They can also be a part of a quarter, half, and full bridge configuration using multiple rosettes.
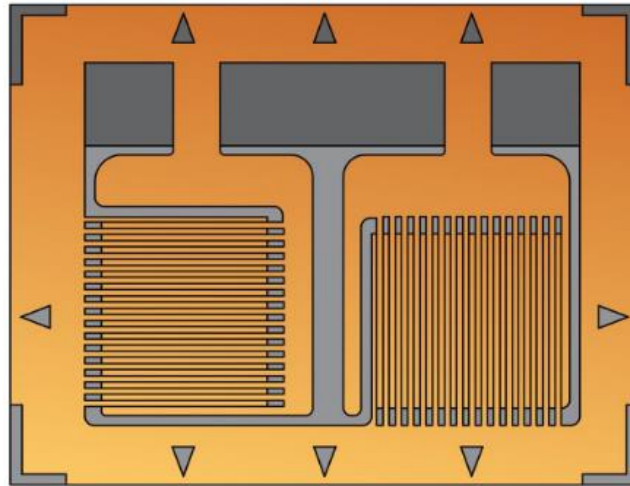
Figure 73: Tee rosette electrical resistance strain gauge [85] (edited).

3) **Rectangular Rosette –** This type consists of three measuring elements positioned at 0°, 45°, and 90° angles to each other (**Figure 74**). They are employed in situations where the principal directions of strain are uncertain or not known at all.
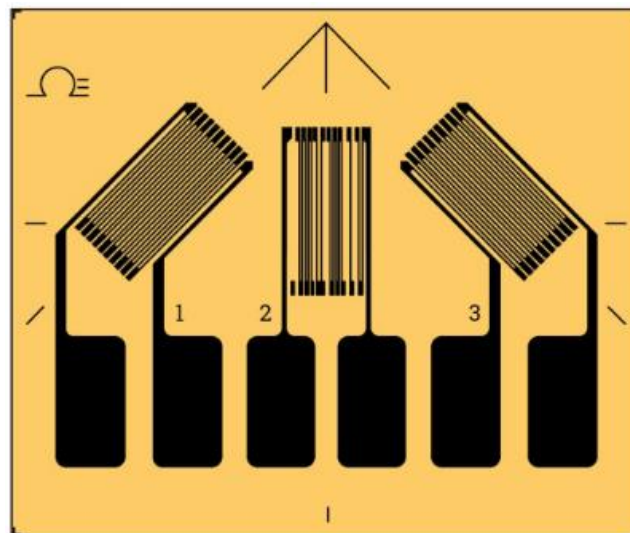
Figure 74: Rectangular rosette electrical resistance strain gauge [85] (edited).

4) **Shear –** Shear electrical strain gauges are utilized to measure shear strain resulting from torque or torsional loading. They can feature either a single or two measuring grids attached to a common carrier (Figure 75). In the case of a single element, it is oriented at a 45° angle to the shaft axis. For a two-grid shear strain gauge, also known as V rosette, the measuring elements are positioned at 45° and 135°.

5) **Diaphragm –** Diaphragm strain gauges are employed for assessing both radial and tangential strain. They are commonly set up in a full bridge configuration with the four measuring elements arranged in circular or linear patterns (**Figure 76**). The

tangential elements are located close to the outer edge of the carrier, while the radial elements are bonded near the center.
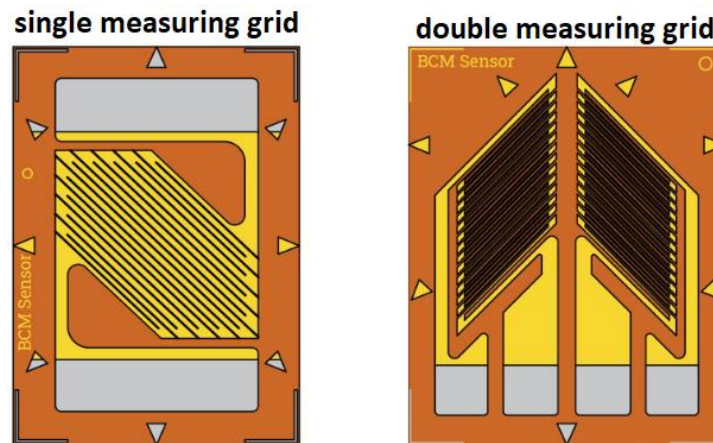
Figure 75: *Shear electrical resistance strain gauge. The left side of the picture shows the strain gauge with one measuring grid while the right side the strain gauge with two measuring grids* **[85]** *(edited).*
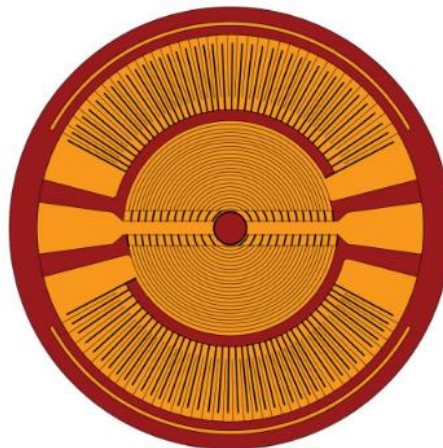
Figure 76: *Diaphragm electrical resistance strain gauge* **[85]** *(edited).*

4.1.5 Signal Conditioning

A successful integration of a sensor into a measurement system requires a variety of steps known as signal conditioning [92]. This entails a number of steps and procedures that convert the sensor's unprocessed output into a signal the measuring system can use. These steps ensure that the sensor's data may accurately contribute to the entire measurement process as well as preparing it for further processing. In essence, signal conditioning is a crucial component of the entire measurement process since it

bridges the gap between the sensor's raw data and the desired output of a measurement system.

The processes involved in signal conditioning are [92]:

1) **Excitation** – Application of a known voltage to the sensor to create response. It can be DC or AC based on the type of sensor that is used. Although some sensors do not require excitation. The voltage that appeared in the previous subsection in Wheatstone bridge configurations represents the voltage excitation (Vs).

2) **Impedance Matching** – The input impedance of the signal conditioning system must match the impedance of the sensor in order to ensure that the signal is accurately and reliably transmitted.

3) **Signal Modification** – This process involves the increase of the signal magnitude (amplification), the removal or correction of any DC-offset, and AC-coupling.

4) **Detection** – In situations where signals are modulated and pose challenges for straightforward information extraction, the "Synchronous Detection" technique is employed. This method involves combining the modulated signal with an unmodulated reference signal that is precisely synchronized with the signal. This synchronization allows for the extraction of information. Alternatively, in certain scenarios, signals do not require synchronization, and information can be directly extracted from the signal (referred to as "Direct Detection").

5) **Linearization** – It is essential to have a clear understanding of how the sensor responds to the measured quantity. This knowledge is crucial for translating the sensor's signal into a meaningful and precise output. Specifically, we aim to convert the sensor signal into a value expressed in units that are relevant to the measured quantity.

6) **Noise Mitigation** – To improve measurement accuracy it is very important to reduce the noise in the output signal. This can be achieved using either low-pass or high-pass filters.

7) **Circuit Protection** – Elctrostatic discharge (ESD) is a threat to numerous electronic parts and circuits found in measurement instruments. The instrument's front-end circuitry incorporates ESD protection components to lessen the chance of damage.

The signal setup for the strain gauges includes; In most cases, a DC excitation voltage is applied to the output of the Wheatstone bridge. However, it's worth noting that AC excitation is not entirely disregarded as it brings several advantages. AC excitation can effectively eliminate offset errors reduce unwanted noise and dimmish any electromagnetic interference [93]. The strain gauge has a high input impedance

meaning that the signal conditioning system must have high impedance too, so the signal can be transmitted properly. It certainly needs signal amplification since the output of the strain gauges is in the order of millivolts/microvolts. As for the detection, is direct and there is no need for linearization. A low-pass filter is also required to reduce the unwanted noise in the measurements [92].

4.1.5.1 Amplification and Noise Reduction

In measurement systems with strain gauges, ensuring accuracy in data acquisition is essential. Consequently, signal amplification and noise reduction become critically important and demand further attention.

When amplifying a measurement system, it is possible that, in addition to amplifying the signal containing the desired information, the amplifier may also amplify any other signals that are generated due to noise. So, it is important to use amplifiers that have specific characteristics like high common-mode rejection (CMR), which are capable of amplifying the desired signal while simultaneously rejecting the interference signals at the system's output.

Instrumentation Amplifiers (in-amps)

Instrumentation amplifiers are often used in industrial and medical environments to handle weak signals while efficiently managing common-mode voltages [94]. For that reason, they are suitable in Wheatstone bridge configurations with strain gauges.

The most classic and common configuration for an instrumentation amplifier is the three-op-amp structure, depicted in **Figure 77**.
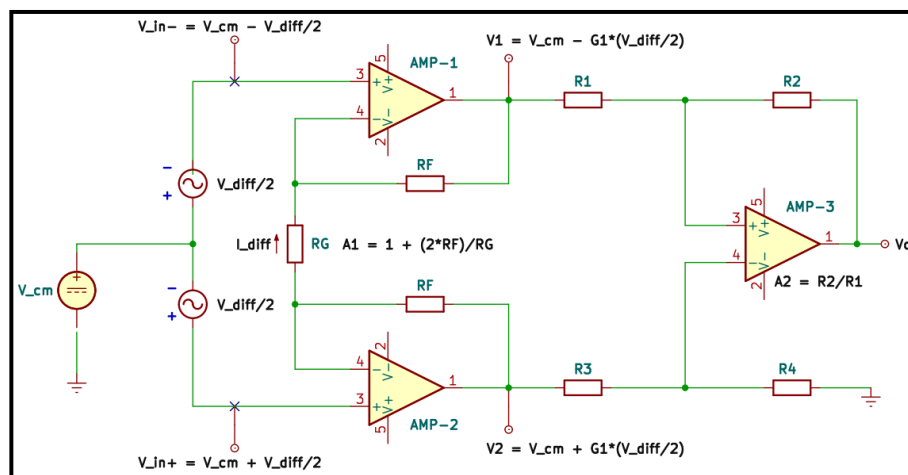
Figure 77: *A classic and common structure (three-op-amp) of an instrumentation amplifier* [94] *(edited)*.

In the in-amp circuit, two op-amps serve as input buffers at the front end. These op-amps, operating with negative feedback, provide a high input impedance that

matches the high output impedance of the strain gauges, ensuring minimal loading of the source signals. At the circuit's end, a differential op-amp stage is employed to eliminate the presence of common-mode voltage in the output signal [94], [95]. To provide a better understanding of the in-amp's principles, a mathematical representation of its operation can be used:

The instrumentation amplifier's inputs are subdivided into a common-mode voltage (V_{cm}) that represents the noise, and a differential voltage (V_{diff}) that represents the signal that contains the desired information. V_{cm} is determined by averaging the inputs (V_{in-}, V_{in+}), while V_{diff} is obtained from the difference between the inputs, as equation 13 and 14 show below, respectively.

$$V_{cm} = \frac{V_{in-} + V_{in+}}{2} \qquad \text{Equation 13}$$

$$V_{diff} = V_{in+} - V_{in-} \qquad \text{Equation 14}$$

Analyzing the above equations, the following results are obtained:

$$V_{in+} = V_{cm} + \frac{V_{diff}}{2} \qquad \text{Equation 15}$$

$$V_{in-} = V_{cm} - \frac{V_{diff}}{2} \qquad \text{Equation 16}$$

The amp-1 and amp-2 apply in the differential voltage at the edges of the resistor RG, thus, it is generated a current I_diff. Using the Ohm's law, I_diff is calculated:

$$I_{diff} = \frac{V\_diff}{RG} \qquad \text{Equation 17}$$

Based on the above, the outputs of amp-1 and amp-2 can be described mathematically as follows:

$$V1 = V_{in-} - I_{diff} \times RF \rightarrow$$
$$\rightarrow V1 = V_{cm} - \frac{V_{diff}}{2} - I_{diff} \times RF \qquad \text{Equation 18}$$

$$V2 = V_{in+} + I_{diff} \times RF \rightarrow \qquad \text{Equation 19}$$

$$\rightarrow V2 = V_{cm} + \frac{V_{diff}}{2} + I_{diff} \times RF$$

Substituting equation 17 into 18 and 19, gives the final form of V1 and V2:

$$V1 = V_{cm} - \frac{V_{diff}}{2} \times (1 + 2 \times \frac{RF}{RG}) \qquad \text{Equation 20}$$

$$V2 = V_{cm} + \frac{V_{diff}}{2} \times (1 + 2 \times \frac{RF}{RG}) \qquad \text{Equation 21}$$

It is observed that the term $\frac{V_{diff}}{2}$ is multiplied by the term $1 + 2 \times \frac{RF}{RG}$, which represents the gain A1. It is also very clear that from equations 20 and 21, only the differential voltage is multiplied while the common-mode voltage remains as is. Finally, the differential amplifier amp-3, calculates the difference between V1 and V2, and then amplifies this difference using gain $2 = \frac{R2}{R1}$. Amp-3 is a unity gain amplifier because in most cases are R1=R3 and R2=R4. The meaning of the third amplifier is to reject completely the common-mode voltage ensuring that will not appear in the output.

One of the primary challenges with instrumentation amplifiers is the limited range of input values in the differential stage at the end of the circuit. Input saturation may happen from common-mode signal coming from close equipment, together with differential DC potentials emerging from signal sources at dissimilar locations. Such an event can result in undesirable consequences. For instance, the output may appear normal, but it might not accurately reflect the required signal.

<u>Operational Amplifiers (op-amps) Configurations</u>

The output signal from the Wheatstone bridge, which contains the crucial information, can be amplified by an instrumentation amplifier with excellent common-mode signal rejection, as it was presented above. However, it is important to keep in mind that instrumentation amplifiers are frequently more expensive than simple operational amplifiers. Alternative amplification circuits that incorporate operational amplifiers have been developed in response to the cost restrictions and can give the same or better performance as the instrumentation amplifiers do.

In comparison to the conventional Wheatstone bridge circuit, the configuration shown in **Figure 78** uses fewer bridge elements and the instrumentation amplifier is replaced by a less expensive operational amplifier.
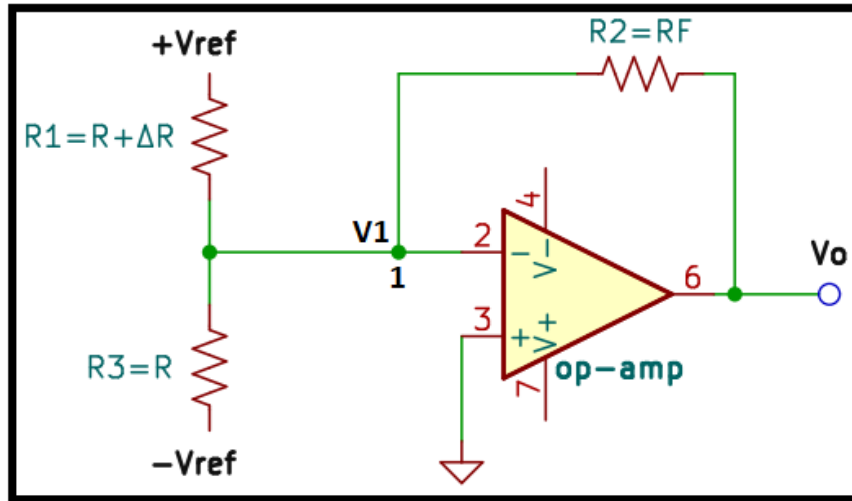
Figure 78: *A less expensive configuration to amplify the Wheatstone's bridge output signal* **[96]** *(edited).*

R1 and R3 are the only resistors left from the wheatstone's bridge original circuit. Resistor R1 represents the strain gauge and ΔR is the change in resistance when the strain gauge operates.

Using the node voltage method at node 1, the voltage output V_O is calculated by the following equation:

$$V1 \times \left(\frac{1}{R1} + \frac{1}{R3} + \frac{1}{R2}\right) - V_{ref} \times \frac{1}{R1} - \left(-V_{ref}\right) \times \frac{1}{R3} - V_O \times \frac{1}{R2} = 0 \rightarrow$$

$$\rightarrow V_O = \frac{RF}{R} \times \frac{\Delta R}{R + \Delta R} \times V_{ref} \qquad \text{Equation 22}$$

The voltage V1 is equal to 0 because the posititve input of the operational amplifier is grounded.

The output voltage signal is amplified four times that of the original Wheatstone bridge's circuit (when ΔR << R). At the same time, the circuit is designed in a way that does not accept the common-mode input signals, that are generally generated by noise. In addition, in this circuit can be adjusted multiple strain gauges without countering any difficulties, as **Figure 79** shows.

By applying the node voltage method again at node 1, the multigauge's circuit output is given by:

$$V_O = \frac{RF}{R} \times \frac{\sum_{i=1}^{n} \Delta R_i}{R + \Delta R} \times V_{ref} \qquad \text{Equation 23}$$
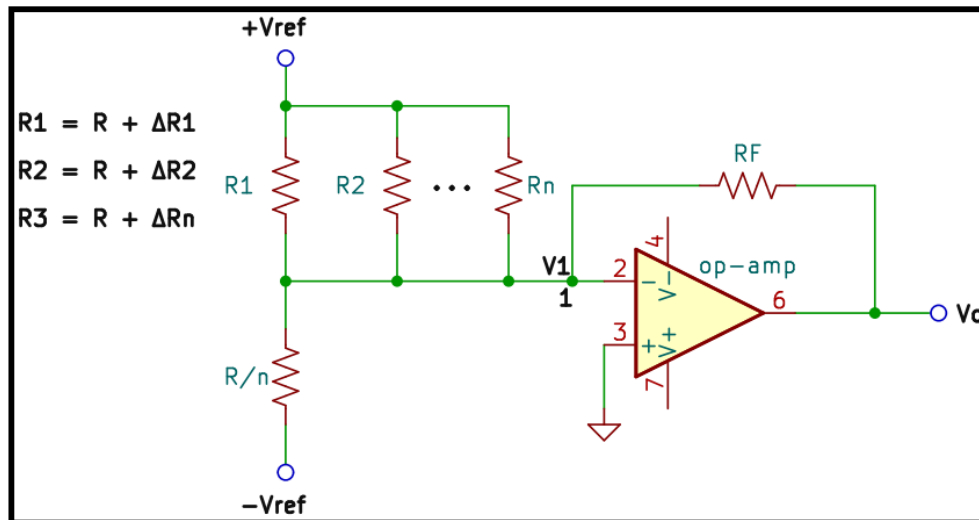
Figure 79: *A multigauge configuration for the circuit of Figure 91* **[96]** *(edited).*

However, this circuit produces a linear output only when the change in resistance ΔR is way smaller than the resistance R (ΔR << R), and uses two reference voltages, which add complexity to the circuit design and increase the chances of errors in implementation.

4.2 Fiber Bragg Grating Sensors (FBGS)

Fiber Bragg Gratings (FBGs) were discovered in 1978 but didn't become commercially available until 1995. Their inclusion as biomechanical sensors into the field of biomechanics occurred in the late 2000s with the purpose of measuring strains at the interface of bone-implant systems [83]. Recently, Fiber Bragg Grating Sensors (FBGS) have garnered significant attention from researchers and engineers due to their remarkable properties. These include their small size, making them ideal for fitting into complex environments without consuming excessive space, their rapid response coupled with high sensitivity for faster and more accurate results, and their immunity to electromagnetic interference-a crucial advantage in environments filled with electrical and optical equipment that could otherwise disrupt measurements.

Additionally, FBGs can also be used for in vivo applications, monitoring various parameters in real-time, thanks to their biocompatibility and nontoxicity characteristics [97], [98], [99]. Probably the biggest benefit of FBGs is their multiplexing capability. This feature makes it possible to measure simultaneously several physical parameters such as strain, temperature, pressure, and vibration with high accuracy. With these capabilities, FBGs become indispensable instruments for clinical diagnoses, treatments,

and biomechanical research. They provide non-invasive and high-resolution monitoring of biomechanical parameter monitoring for a wide range of biomedical applications.

4.2.1 Structure of FBG

The FBG is typically made of a standard single–mode optical fiber that consists of three elements and a small periodic pattern of refractive index changes in its core, as shown in **Figure 80** below. The core is the central region of the optical fiber where light propagates. Surrounding the core is the cladding, which has a slightly lower refractive index than the core, thus it helps confine the light within the core by offering total internal reflection. In more simple words it acts as a barrier, preventing light from escaping the core. The core and the cladding are protected by a polymer coating that offers mechanical strength and protection from environmental factors [100].
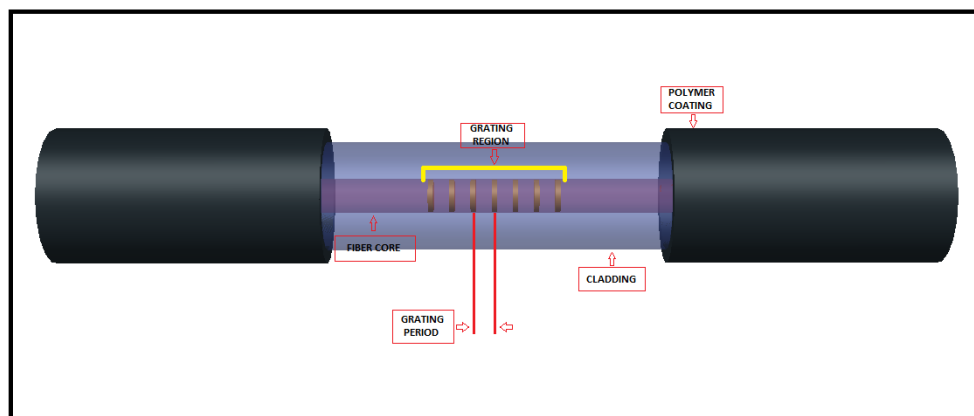
Figure 80: *Structure of Fiber Bragg Grating* **[101]** *(remake).*

The periodic pattern of refractive index changes, also called the "grating" is formed by exposing the core of the fiber to Ultraviolet (UV) light [102]. This specific process of the grating's formation inside the fiber core is called photoinscription. However, photoinscription is beyond the scope of this study and it will not be further analyzed.

4.2.2 Working Principles – Configuration System

A periodic region of different refractive indices is included in the FBG structure, as previously presented. The refractive index is a fundamental property of a material that describes how light propagates through it. It is essentially a measure of how much the speed of light slows down when entering a medium compared to its speed in vacuum. Mathematically it is represented as the ratio of the speed of light in vacuum to the speed of light in matter:

$$n = \frac{c}{u} \hspace{4cm} \text{Equation 24,}$$

where n is the refractive index, c the speed of light in vacuum, and u the speed of light in a medium.

When light changes medium, it also changes speed. This results in the light being reflected or absorbed, depending on the angle of incidence and the details of the materials involved. In the case of FBG, the grating period consists of alternating regions with different refractive indices. When light passes through this grating structure, it interacts with the periodic variation in refractive index. This interaction results in only certain wavelengths being reflected back. The wavelengths that are reflected back must meet the Bragg condition, also known as Bragg's law. Bragg's law is a fundamental principle in physics that describes the behavior of waves, like light, when they encounter a periodic structure. It states that constructive interference occurs when the path length difference of waves scattered by adjacent regions is an integer multiple of the wavelength.

For example, suppose two waves with identical wavelength (λ) and phase (parallel to each other) approach a crystal structure and are scattered by two different atoms, as shown in the figure below.
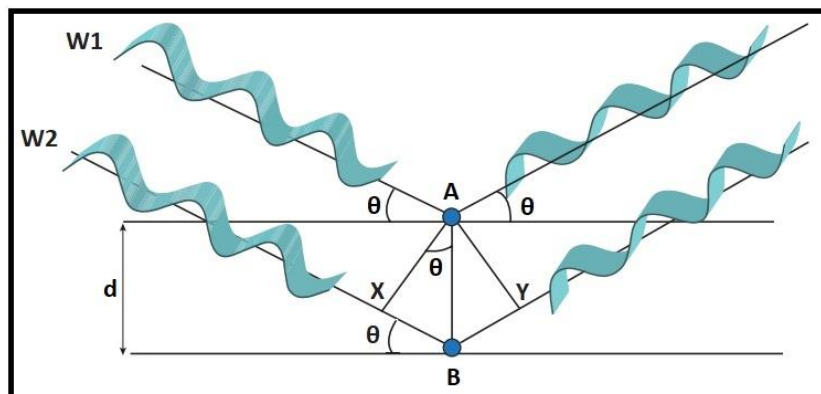
Figure 81: *Example of Bragg's condition with two identical parallel waves* **[103]** *(edited)*.

The second wave (**W2**) crosses an extra distance in relation to the first (**W1**) which is $XB + BY$. This distance will of course be equal to a multiple of the wavelength:

$$XB + BY = n\lambda \hspace{4cm} \textbf{Equation 25}$$

Based on the two right-angled triangles two equations arise:

$$\sin \theta = \frac{XB}{d} \Rightarrow XB = d \times \sin \theta \hspace{3cm} \textbf{Equation 26}$$

$$\sin \theta = \frac{BY}{d} \Rightarrow BY = d \times \sin \theta \qquad \text{Equation 27}$$

Substituting equation 26 and 27 into equation 25:

$$d \times \sin \theta + d \times \sin \theta = n\lambda \Rightarrow 2d \times \sin \theta \qquad \text{Equation 28,}$$
$$= n\lambda$$

where d is the distance between the two atoms, θ is the angle of incidence, and n is the diffraction order. **Equation 28** is called Bragg Condition or Bragg Equation.

Now, if the Bragg condition is met, there will be constructive interference, and the two waves will add together, resulting in a wave with a larger amplitude. In any other case, there will be destructive interference, causing the two waves to diminish each other, creating a smaller wave or even canceling each other out.

In the case of an FBG, when light passes through its structure, only certain wavelengths will be reflected due to the grating, as explained previously. These wavelengths, which satisfy the Bragg condition, will combine to form a new wave with wavelength λ_B, known as the Bragg wavelength. The equation for calculating the Bragg wavelength is:

$$\lambda_B = 2 \times n_{eff} \times \Lambda \qquad \text{Equation 29,}$$

where n_{eff} is the effective refractive index and Λ is the period of the grating. Below is a diagram showing the reflected and the propagated light.
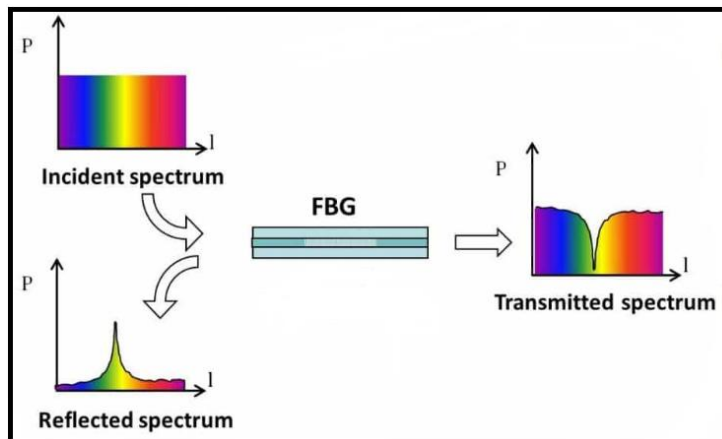
Figure 82: *Fiber bragg grating principle – illustration of reflected and transmitted light* [104].

Any axial strain experienced by the FBG leads to the change of the period of the grating and the effective refractive index, as a result, the reflected Bragg wavelength changes (**Figure 83**). These changes in Bragg wavelength are typically detected and analyzed using optical spectrum analyzers (OSA) and are further processed to produce

the required data. Optical circulators are also used to separate the incident light from the reflected (**Figure 84**).
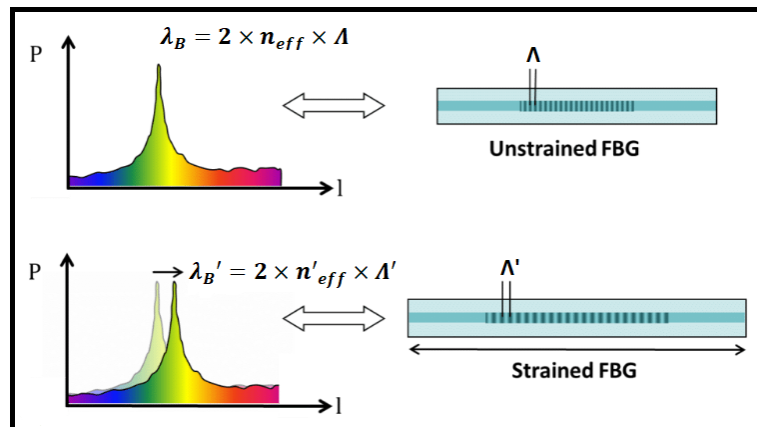
Figure 83: *Bragg wavelength change due to axial strain* **[104]** *(edited).*

However, when using an FBG in practical methods to monitor strains, it also exhibits a high sensitivity to temperature changes. In particular, the Bragg wavelength is affected by both the axial strains and temperature changes at the same time [97]. So, Equation 29, shifts accordingly [105]:

$$\Delta \lambda_B = 2 \times \left[\Lambda \times \frac{\partial n_{eff}}{\partial T} + n_{eff} \times \frac{\partial \Lambda}{\partial T}\right] \times \Delta T + 2 \times \left[\Lambda \times \frac{\partial n_{eff}}{\partial \ell} + n_{eff} \times \frac{\partial \Lambda}{\partial \ell}\right] \times \Delta \ell \qquad \textbf{Equation 30,}$$

where ΔT and $\Delta \ell$ are the temperature change and the FBG length change, respectively. It is understandable that this sensitivity to temperature causes measurement accuracy problems. For that reason, they have been developed discrimination methods that will be discussed in the following undersections.
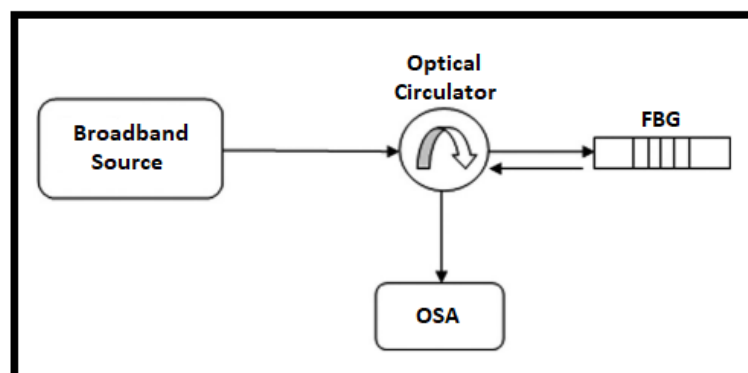
Figure 84: *A simple interrogation setup system for Fiber Bragg Gratings* **[106]** *(edited).*

4.2.3 Types of Fiber Bragg Grating Sensors

FBGs are utilized across numerous fields including telecommunications, biomechanics, and photonics. Obviously these fields evolve as time passes through, and new challenges-demands are brought to the surface. For that reason, it becomes essential to develop various types of FBGs with different characteristics to meet these evolving needs effectively. Over the years there have been developed many types of FBGs to address a wide range of applications while maintaining optimal performance and reliability.

The type of FBG used as an example in the previous subsections to explain the structure and the working principles is the most common one and is called the "Uniform FBG" (UFBG)as the refractive index modulation along the length of the fiber core is uniform (**Figure 80**). The current subsection aims to present the structures of these different types of FBGs as well as their properties.

4.2.3.1 Chirped Fiber Bragg Gratings (CFBGs)

Compared to uniform FBGs, which are designed to have a consistent periodicity of the refractive index, Chriped Fiber Bragg Gratings (CFBGs) have a varying periodicity of the refractive index along the z-axis. This variation can be linear or non-linear, as shown in **Figure 85** below. In such types of FBGs, the Bragg wavelength varies along the length of the grating, meaning each segment of the grating reflects a different spectrum, resulting in a broader overall Bragg wavelength than that reflected by UFBGs.
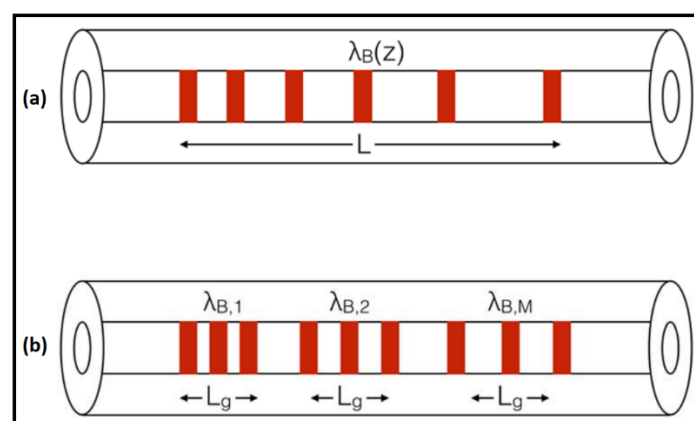
Figure 85: *(a) Linear Chirped FBG, (b) non-linear Chirped FBG* **[107]** *(edited).*

This also means that the overall spectrum is affected by the temperature or/and the strains occurring in each segment of the grating. Therefore, a CFBG sensor can [107]:

1) Detect how the temperature or strain varies along different segments of the grating.

2) Identify local changes, such as small hot spots or sudden changes in strain.

3) Monitor how these local changes progress over time.

4.2.3.2 Tilted Fiber Bragg Gratings (TFBGs)

Tilted Fiber Bragg Gratings (TFBGs) have a similar structure to UFBGs with one key difference: their grating is tilted relative to the fiber axis, instead of being perpendicular (**Figure 86**). This tilt angle allows for a unique interaction between the light propagating in the medium and the grating. As the light travels through the core of the optical fiber, some of it is reflected by the grating, similar to UFBGs. However, due to the inclination of the grating, part of the light is coupled into the cladding, where it propagates. Light in the cladding can interact with the environment because the cladding is closer to the outer surface of the fiber. This interaction makes the cladding modes sensitive to external factors such as changes in the refractive index of the surrounding medium.
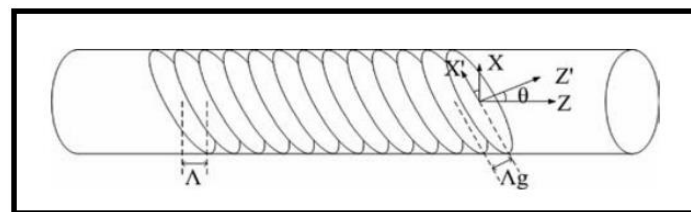
Figure 86: *Structure of the Tiltted Fiber Bragg Grating* **[108]**.

In addition to the primary Bragg wavelength peak, there are additional peaks in the transmission spectrum due to the light coupling into the cladding modes [109]. These peaks are highly sensitive to changes in the refractive index of the cladding. Consequently, measurements from a TFBG are derived from monitoring and analyzing both the reflected light and the transmitted light, providing detailed and sensitive environmental sensing. **Figure 87** shows the transmission and reflection spectra of a UFBG and a TFBG. In a TFBG the Bragg wavelength is calculated as follows:

$$\lambda_B = \frac{2 \times n_{eff} \times \Lambda_g}{\cos(\theta)} \qquad \qquad \textbf{Equation 31}$$

,where Λ_g is the periodicity of the tilted grating and (θ) is the tilt angle of the grating planes.
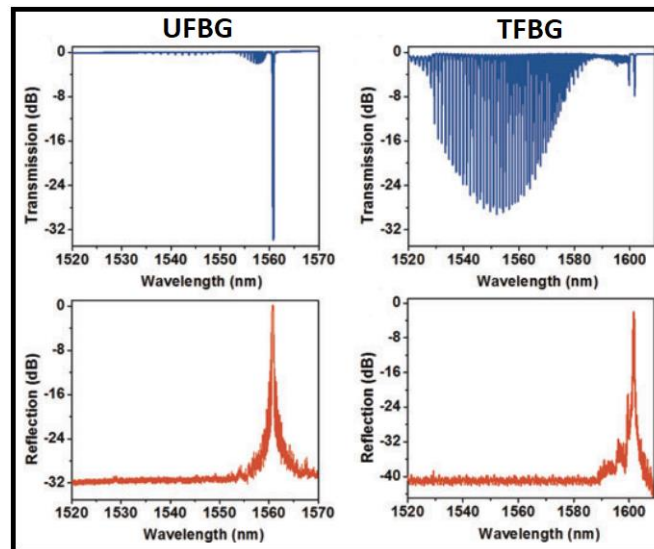
Figure 87: *Transmission and reflection spectrum of a UFBG (left part of image) and a TFBG (right part of image)* **[110]** *(edited)*.

4.2.3.3 Phase Shifted Fiber Bragg Gratings (PS-FBGs)

PS-FBGs or πFBGs are a specialized type of FBG that introduces a discrete phase shift within the grating structure (**Figure 88**). The size of the phase shift can assume different values, such as $\pi/2$, π, $3\pi/2$ and so on [111]. This phase shift results in the creation of a narrow transmission window within the broader reflection spectrum of the FBG. In other words, the phase shift disrupts the periodicity in such a way that a specific wavelength, which would otherwise be reflected back, is allowed to pass through.
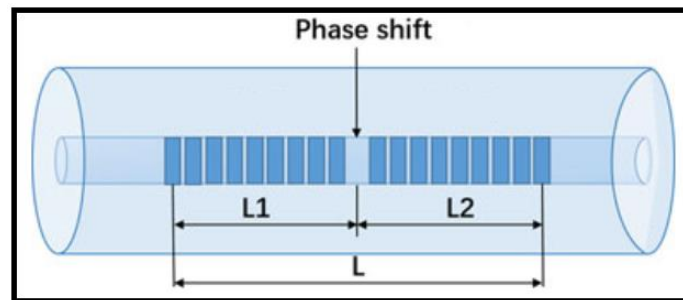
Figure 88: *Structure of a Phase Shifted Fiber Bragg Grating* **[112]** *(edited)*.

Thus, the reflection spectrum contains a narrow dip (**Figure 89**) that significantly impacts its sensitivity and measurement capabilities. Any slight changes at the grating result in a noticeable change in the position and characteristics of the narrow dip, and this alteration can be used to obtain precise measurements. Researchers successfully use this property of a PS-FBG sensor to create methods for high-resolution dynamic strain measurements [111].
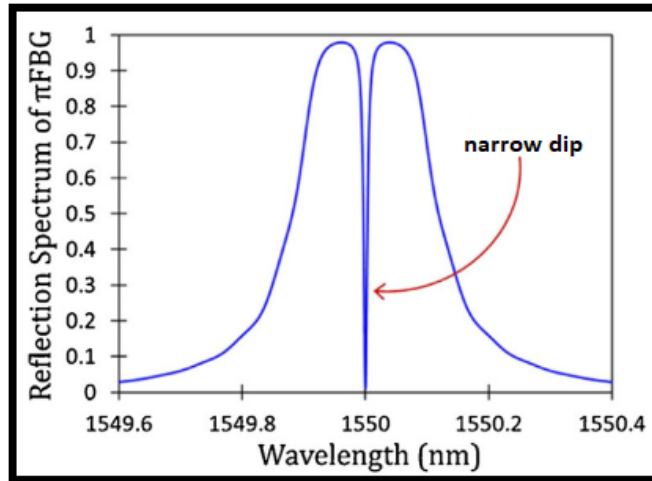
Figure 89: *The reflection spectrum of a PS-FBG. The y-axis in the graph represents the reflection coefficient or reflectivity of the PS-FBG (0 = no reflection and 1 = total reflection)* **[111]** *(edited).*

4.2.4 Discrimination Methods for Temperature and Strain

In 4.2.2 it was mentioned that FBGs can be both sensitive to temperature and strain at the same time. In many scenarios in which precise strain measurement is required, like monitoring the strains on cadavers, the influence of temperature raises a variety of serious problems in the integrity of the data acquired from the FBG sensor. For that reason over the years, there have been developed discrimination methods that help detect and separate the temperature from the strain measurements.

4.2.4.1 Reference FBG Method

This method requires two completely identical FBGs, where one will be used to monitor the strains, while the other as a reference component for the temperature. In order for this method to be effective, both of the FBGs must exist in the same thermal environment and the reference FBG must be strain-free. The schematic diagram of this method is presented in **Figure 90**.
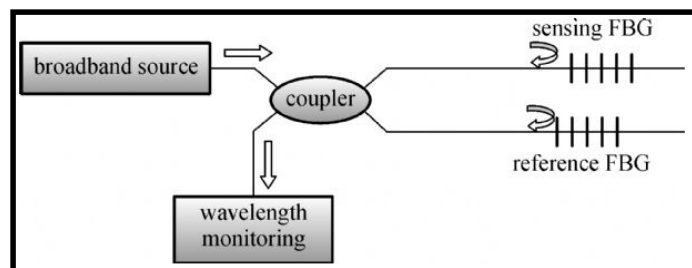
Figure 90: *Schematic diagram of the reference FBG method for the discrimination of temperature and strain* **[113]** *(edited).*

The purpose of the reference FBG is to monitor the temperature that causes the strain error in the other FBG's measurements. In that way, it is possible to subtract the

wavelength shift caused by temperature variations from the wavelength shift obtained with the strain FBG [114].

This method is considered to be the most easy to implement and cost-effective than the others, however raises a challenge because it requires two identical FBGs, which is extremely hard to construct in the first place.

4.2.4.2 Dual Wavelength Superimposed FBGs Method

The implementation of a dual-wavelength superimposed FBG can be considered as another way to discriminate strain and temperature. This special FBG has two different gratings inscribed at the same region in the core of the optical fiber. Suppose the wavelength shifts in strain and temperature have linear behavior, the Bragg wavelength shift ($\Delta\lambda_B$) with the respect to the change in strain ($\Delta\varepsilon$) and temperature (ΔT) can be calculated as follows:

$$\Delta\lambda_B = \aleph \times \Delta\varepsilon + \Re \times \Delta T \qquad \textbf{\textcolor{blue}{Equation 32}}$$

, where $\aleph$ and $\Re$ are the strain and temperature sensitivities of the FBG, respectively [114].

From **Equation 32** it is clear that the strain is not directly dependent on temperature. In a superimposed FBG, there are two wavelengths as said previously, thus **Equation 32** can be transformed into the following matrix:

$$\begin{bmatrix} \Delta\lambda_{B1} \\ \Delta\lambda_{B2} \end{bmatrix} = \begin{bmatrix} \aleph 1 & \Re 1 \\ \aleph 2 & \Re 2 \end{bmatrix} \begin{bmatrix} \Delta\varepsilon \\ \Delta T \end{bmatrix} \qquad \textbf{\textcolor{blue}{Equation 33}}$$

, where 1 and 2 denote the two distinct wavelengths [114].

By measuring the wavelength shifts with strain and temperature one at a time, it is possible to determine the values of $\Delta\varepsilon$ and ΔT. Once the change in strain and temperature is determined, they can be used to discriminate the measurements.

4.2.4.3 Different Cladding-Diameter FBGs Method

This method follows the same concept as the dual-wavelength superimposed FBGs method. Two FBGs with the same grating but with different cladding diameters are joined together, thus a scenario is created where the response to strain and temperature is different for each FBG. Because the two FBGs have different cladding diameters, the extent of the wavelength shifts will differ for each FBG due to their different sensitivities to strain and temperature. The change in temperature and strain can be obtained by **Equation 32** in the same way as described in 4.2.4.2. The schematic of the two FBGs that are joined together is presented in Figure 91 below. This technique is easy to implement just as the method with the reference FBG, however, the structure of

this composed sensor raises problems at the point where the two different claddings are joined together. These problems refer to the low mechanical strength and the light that can be lost at the junction where the two optical fibers are fused together [114].
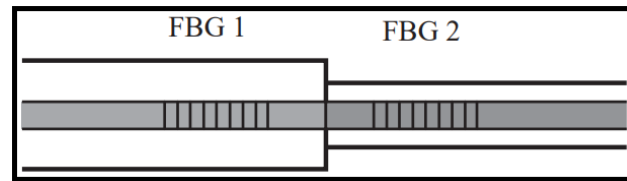
Figure 91: *Schematic of the two joined FBGs with different cladding diameters* **[114]** *(edited).*

4.3 Linear Variable Displacement Transducers

A linear variable differential transducer (LVDT) is an electromechanical sensor used to measure linear displacements with extremely high accuracy. In the field of biomechanics, it can be used in cadaver studies to monitor the displacements of an implant inside a femoral bone during a mechanical test. This allows the integrity and quality of the implant, as well as the surgical technique, to be evaluated.

The structure and the design of LVDT sensors are simple and do not require high-cost components. **Figure 92** presents the structure of the LVDT sensor, and **Figure 93** depicts the equivalent circuit. It consists of a primary coil C1, two identical secondary coils C2-C3, and a core that has the ability to move freely on the inside.
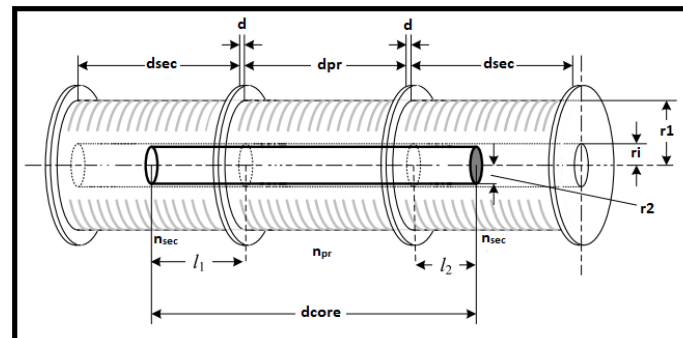
Figure 92: *Structure of the LVDT sensor* **[115]** **(edited).**

The basic principle of LVDT operation relies on electromagnetic induction. If an excitation signal $U_{pr} = V_{pr} \times \sin(\omega_{pr}t)$ is applied to the primary coil, it creates a magnetic field around which induces an alternating voltage in the two secondary coils [116], where U_{pr} is the instantaneous value of the voltage at time t, V_{pr} is the maximum or peak value of the voltage, ω_{pr} is the angular frequency, and t is the time variable. Now, by using the mutual inductance principle and Faraday's law of electromagnetic induction, the voltage that is induced to the secondary coils C2 and C3 is [117]:

$$U_{sec1} = \frac{2 \times \pi^2 \times \omega_{pr} \times U_{pr} \times n_{pr} \times n_{sec} \times (2l_2 + d_{pr})}{10^7 \times d_{sec} \times d_{core} \times Z_{pr} \times \ln(r_2 / r_1)} \times l_1^2 \qquad \textbf{Equation 34}$$

$$U_{sec2} = \frac{2 \times \pi^2 \times \omega_{pr} \times U_{pr} \times n_{pr} \times n_{sec} \times (2l_1 + d_{pr})}{10^7 \times d_{sec} \times d_{core} \times Z_{pr} \times \ln(r_2 / r_1)} \times l_2^2 \qquad \textbf{Equation 35}$$

, where n_{pr} and n_{sec} are the numbers of the turns of the primary and secondary coils, respectively, l_1 and l_2 represent the distances that the core has penetrated into the secondary coils C2 and C3, respectively, d_{pr}, d_{sec} and d_{core} are the lengths of the primary and secondary coils and the moving core, respectively, Z_{pr} is the impedance of the primary coil and r_1 and r_2 are the radius of the secondary coils and the moving core, respectively.
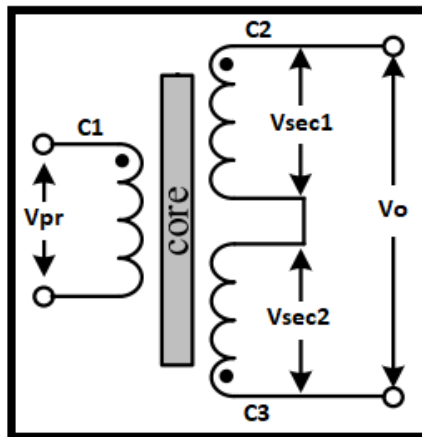
Figure 93: *The equivalent circuit of the LVDT sensor* **[115]** *(edited).*

The secondary coils are connected in opposite directions as shown in **Figure 93** and the output voltage is:

$$U_o = U_{sec1} - U_{sec2} \qquad \textbf{Equation 36}$$

The position of the movable core affects the magnetic coupling between the primary and secondary coils. When the core is at the center, the voltages induced in both secondary coils are equal and opposite, resulting in zero output voltage. When it moves away from the center it causes an imbalance in the magnetic coupling, resulting in a differential voltage that is proportional to the displacement of the core. In that way, it is possible to track any movements, even the tiny ones of an object.

4.4 Digital Image Correlation

For many decades biomechanical sensors like strain gauges (SGs) were the primary tool for monitoring strains. These sensors can still provide precise and reliable measurements today. However, in objects with extremely complex shapes, where even tiny regions are important to monitor, these conventional sensors cannot adequately cope [118]. The introduction of optical techniques to the biomechanical field has revolutionized the way strains can be monitored and studied. Optical techniques have already shown to engineers and researchers that they can be used to identify the properties of various materials [119] even those with anisotropic behavior [120], such as bone tissue.

Digital Image Correlation (DIC) is one of the optical techniques that gained a lot of attention recently due to its ability to identify strains in complex objects with extremely high precision. This technique is so reliable and accurate that the data provided from experimental procedures can be used to study musculoskeletal biomechanics [121] and validate Finite Element (FE) models [42].

DIC is a non-contact technique that relies on the process of digital images to analyze the changes in an object's surface pattern during mechanical tests.

The implementation of DIC's technique can be described as a series of steps, each serving a specific purpose within the overall process [122]. The first step is to prepare the surface of the desired specimen that will be mechanically tested. This preparation leads to the creation of a speckle pattern on the specimen's surface which provides a unique signature that can be tracked across multiple images. The speckle pattern can be applied by painting the specimen's surface with white color and then spraying it with black to create this random pattern (Figure 94 (b)). The next step of DIC's process involves the calibration of the system. This includes the positioning of the camera/s and the determination of the measurement volume, which can be achieved by capturing images of a unique calibration plate (Figure 94 (a)).

After the calibration of the system and before the mechanical test begins, it is required to obtain an image of the specimen, which will be used as reference data. The process of the mechanical test then begins and images of the deformed specimen are captured. A special software based on correlation algorithms is used to match subsets of the reference image with subsets of the deformed images. This step identifies the displacement of each pixel between images. By comparing the displacements of

multiple spots, the software calculates the displacement field of the entire surface and produces the strain map.
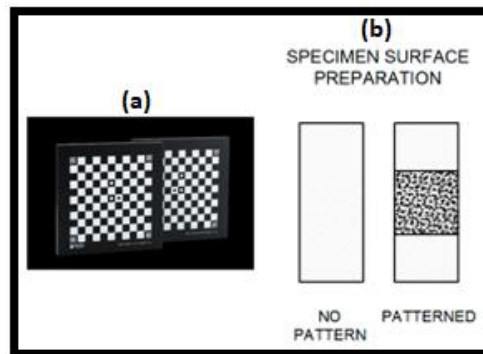
Figure 94: *(a) presents the calibration plate that is used at the beginning of the DIC's process [123], (b) illustration of the speckle pattern that is sprayed on the surface of the tested specimen* **[122]** *(edited).*

The process of DIC can be considered simple and easy to implement. It does not require physical contact with the material, avoiding potential damage or interference, as well as saving time preparing the surface for other biomechanical sensors that require physical contact. In addition, its ability to provide full-filed measurements with high accuracy compared to conventional sensors which cannot cope with the entire surface of the specimen, makes it a valuable tool for biomedical applications, as it provides the means for the entire field to evolve.

5. EXPERIMENTAL PHASE

This experimental phase involves constructing a special mechanical system (loading setup) designed to replicate the primary forces exerted on the human hip joint. The goal is to accurately simulate the conditions experienced by the hip during static-compressive tests and capture the strain distributions of each specimen. The specimens that are going to be used in this experiment are two human cadaveric femoral bones, one intact and one implanted with a prosthetic stem.

To ensure precise measurement and analysis, the strain and force monitoring will be conducted using advanced techniques and transducers such as digital image correlation and load cells. Each specimen will undergo a strict testing protocol, where it will be mechanically tested and monitored five different times. This repetition ensures consistency and reliability in the data that will be collected, allowing for a thorough comparison between the intact and implanted femurs. The results of these tests will provide valuable insight into the mechanical behavior of the femur and the integrity of the implant, under compressive forces.

Because this experimental process involves cadaveric specimens, it is understandably demanding and challenging. Therefore, preparing the proper equipment and materials is vital for the experiment's success. The necessary equipment and materials are as follows:

1) Cadaveric human femoral specimens.
2) Femoral implants designed specifically for the cadaveric specimens.
3) A loading setup to simulate the main hip forces.
4) Load cells to monitor the abductor's force.
5) A digital image correlation system to monitor strains.
6) A press machine to apply the necessary force.
7) Proper software to process the acquired data from the DIC system.

Cadaveric Specimens and Femoral Implant

Two cadaveric femoral bones from a single male donor (left and right femurs) were chosen for mechanical testing under compressive static load. The right femur remained intact and did not show any alterations in its appearance. The left femur was operated on, and a femoral stem was implanted. Both specimens and the implant are shown in the figures below. The cadaveric specimens were initially obtained and processed by 3Ψ Ltd and Akmelogi S.m.p.c. The implant is a patient-specific design constructed through a series of steps by the same companies that provided the specimens.

Figure 95: *Cadaveric specimens used for the experimental procedure. (a) is the left and implanted femur, and (b) is the right intact femur.*
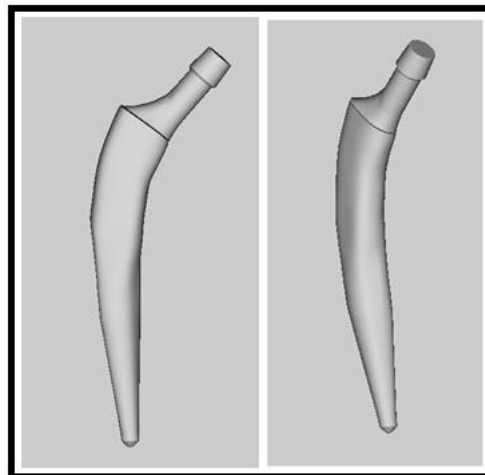
Figure 96: *The patient-specific implant that was manufactured using advanced algorithms and additive manufacturing techniques by 3Ψ Ltd and Akmelogi S.m.p.c.*

An MRI of the selected femur was obtained, and its 3D geometry was generated. Using special algorithms that account for the complex shape and measurements of the human femur, the precise 3D schematic of the implant was created. Finally, using additive manufacturing techniques, the implant was printed. The implant is made of a titanium alloy with the required percentage of porosity to reduce its weight.

The loading setup

The design and construction of the loading setup are crucial steps in the experimental process. The precision of the forces exerted on the specimen directly impacts the accuracy and realism of the measurements and it will determine the effectiveness of the experimental phase.

In Chapter 2, the main forces of the hip joint at a simplified 2D frontal plane were explained, and based on that, the loading setup should be designed in such a way as to account for the following magnitudes and features:

1) The force generated by the body weight.
2) The counterforce generated by the abductors.
3) The joint reaction force.
4) The lever arms of the body force and the abductor force.
5) The angles at which the joint force and abductor force are exerted.
6) Space for a load cell to measure the abductors force.

Considering the above, a makeshift system out of plastic was constructed, and a test was immediately conducted to evaluate its performance. The system layout is illustrated in **Figure 97** below.
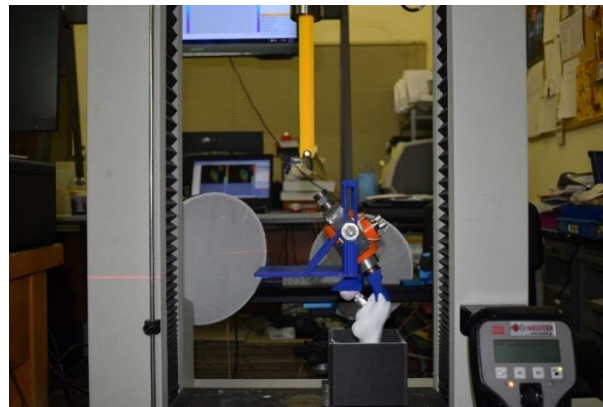
Figure 97: *The makeshift system adjusted to the universal testing machine (provided by 3Ψ Ltd and Akmelogi S.m.p.c.).*

From **Figure 98**, (1) is the surface that is being forced by the press through the yellow extension (6). The length of (1) serves also as the lever arm of the body force. The load cell is screwed into the (2). The sides of (2) can move on the vertical axis and are able to rotate for the adjustment of the position and the angle of the load cell. (3) is the load cell which is a transducer that converts force into measurable electrical output. The upper part of (4) is screwed to the back of the load cell, while the lower part is attached to the greater trochanter. (5) is attached to the femoral head and to the lower part of component (1) so that the force can be applied. (4) and (5) are the components that transfer correctly the forces from the press to the desired points of the femur. According to Cristofolini et.al., the angles at which the joint force and the abductor's force are applied to the hip joint are 18° and 29°, respectively (**Figure 99**). Thus (2), (3), (4), and

(5) were constructed and positioned accordingly. In addition, the system layout ensures that the moment arm of the abductor force always maintains the desired constant length.
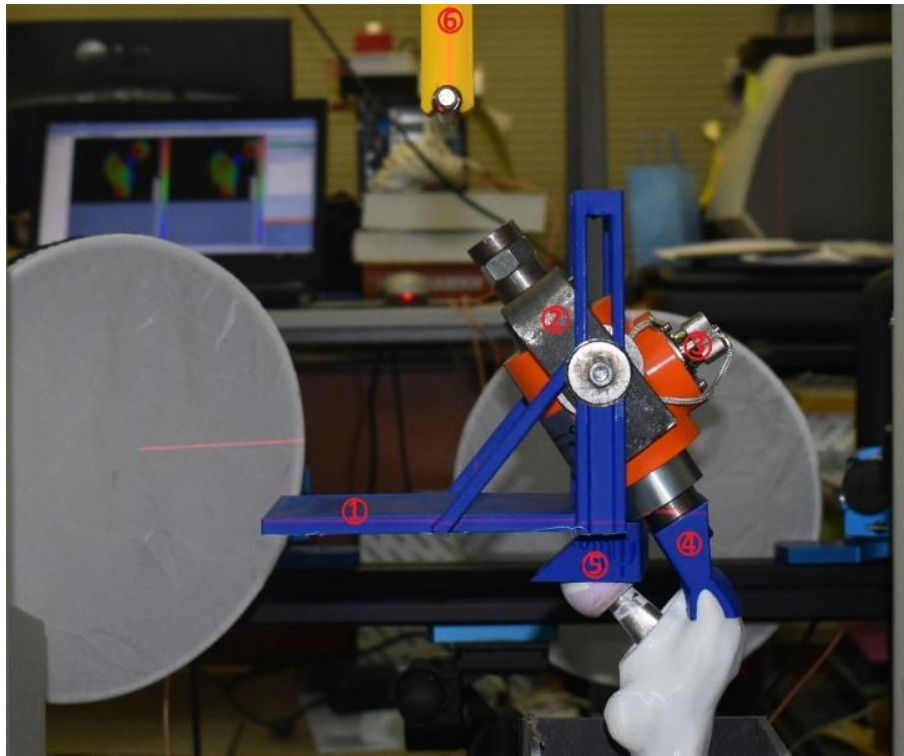
Figure 98: A closer look at the parts of the loading setup.

The press was calibrated (table 1 shows the settings of the press in detail) and an artificial femur was used to conduct this test. During the test, the following were observed:

- The pin which is placed at the end of component (6), has a relatively large surface. The body force must be applied to a small point on the surface of (1).

- Component (1) is very thin and was bending during the test.

- Because most parts are made of plastic, their elasticity caused the system positioning and adjusting problems, as well as stability complications. It should be mentioned here that in the official experiments, all the components will be made of metal, and these problems hopefully will be eliminated. The reason for evaluating the system with plastic components is that they are faster and less costly to manufacture than metal components.

- It was also observed that the surface of component (5) resting on the bottom of the plate (1) did not make good contact.

- Component (4) broke during the experiment. The dotted line in **Figure 100** shows the point from which it broke off.
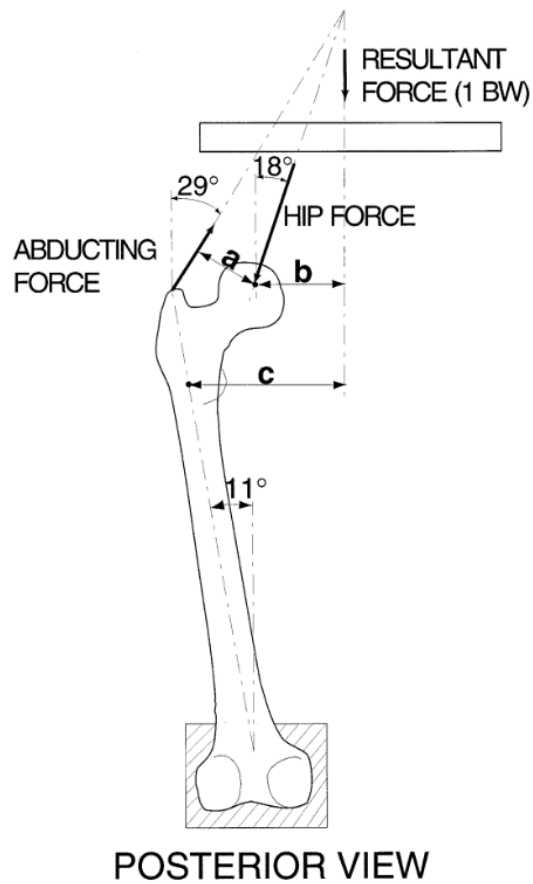
Figure 99: *A schematic diagram that presents the forces and their angle applied to the hip joint* [46].

Pretest	Value	Unit
Width	12.700	mm
Thickness	3.175	mm
Platen Separation	50.800	mm
Test Rate	0.2	mm/s
Strain End Point	10.000	mm/mm
Data Acquisition Rate	1.0	Hz

Table 9: *Universal testing machine settings.*

Based on the above observations and problems, the following proposals were made to improve the system:

- The length of (6) will be reduced by 5cm and the pin at its end will be replaced by a component with a smaller surface area to allow better precision of the body force. The thickness of (1) will be increased to resist the bending forces.

- The top part of (5) will change shape to better apply to the bottom of the plate.

- The side parts of (2) should be suitably shaped so that the load cell can be placed and adjusted more easily.

- Component's (4) design should be altered in that way to mitigate the chance of breaking again and to adapt better on the great trochanter.

- Component (3) can be reduced in size by using a smaller load cell, thereby preserving space and making the system more user-friendly.
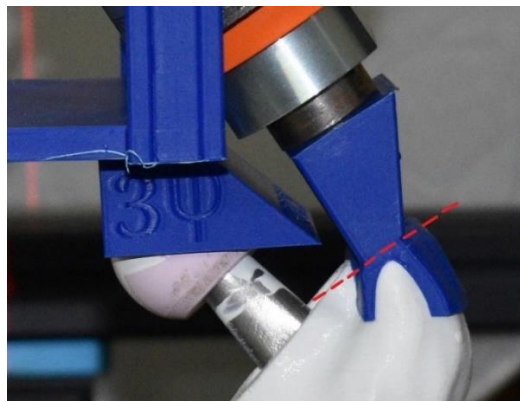
Figure 100: *Component's (4) point of break.*

The system was then redesigned, incorporating the suggested changes, producing its final form. The upgraded system is shown in **Figure 101**. All components were 3D printed using a metal 3D printer to achieve high accuracy of their complex shapes. The materials were specifically selected based on the experiment's demands, requiring high strength, resistance to oxidation due to cadaveric specimens, and good corrosion resistance. These characteristics led to the selection of stainless-steel 17-4 PH, and a plastic with high carbon content, which meet all these criteria and are more cost-effective than many other alloys and materials.

The redesigned system has a more stable and robust structure which eliminates the problems of positioning and adjusting. All components are optimized to fit perfectly with the femur, minimizing the micromotions between the femur-setup system, and the use of a smaller type of load cell was also taken into account, freeing up useful space.
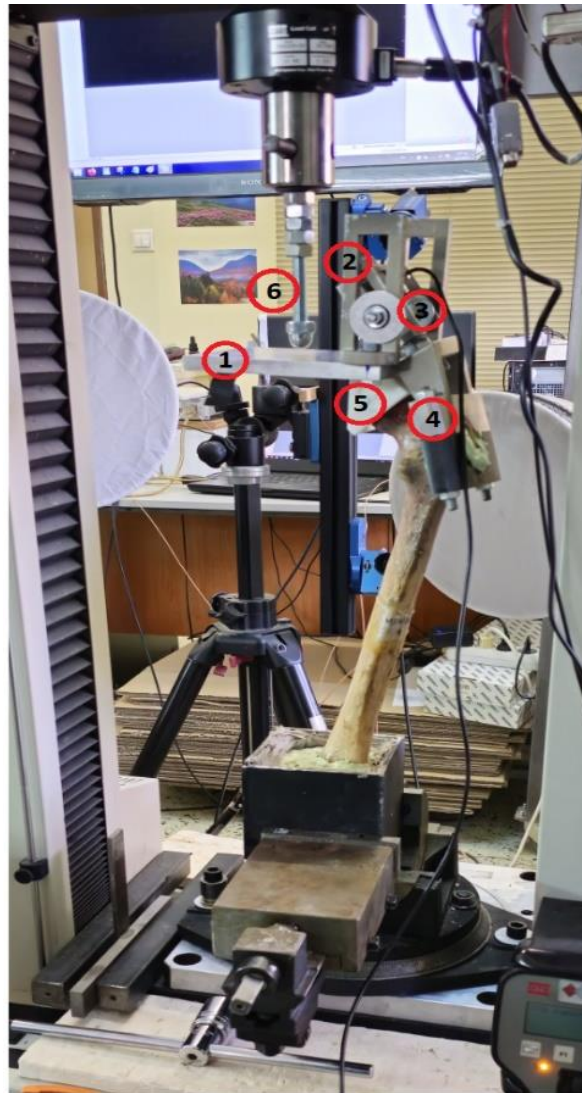
Figure 101: *The final upgraded mechanical system (provided by 3Ψ Ltd and Akmelogi S.m.p.c.)*

As an extend of this work, another type of loading setup was also designed for a wider use. The aim of building this prototype system is to have a robust structure so that it can be used in both static and dynamic load applications. The system's layout appears in the figures below with a more complicated structure, a larger number of components, and a bigger size than the first system. The joint force can be multiple times the body weight during various activities, like jogging and running. To simulate these conditions in a lab, the loading setup must be able to withstand such heavy and repetitive loads continuously. For that reason, the main component which is a 4cm x 4cm x 40cm pure iron rod, was initially chosen to be in such a large size, so the system can sustain not just static loads but also dynamic loads for a long period of time without showing any fatigue or deformation.
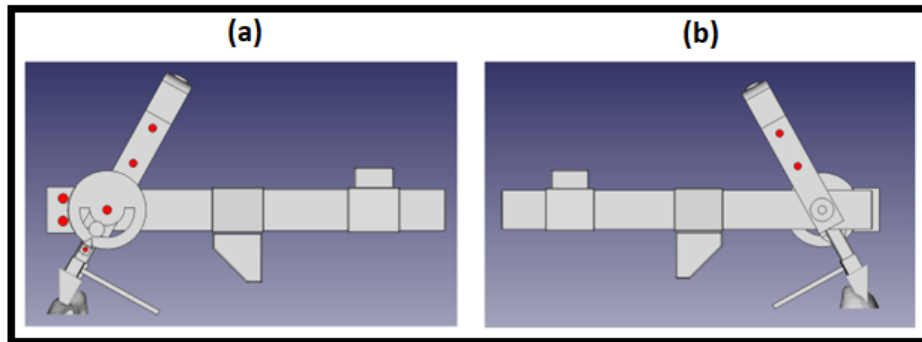
Figure 102: *The system's layout – (a) front view, (b) back view.*
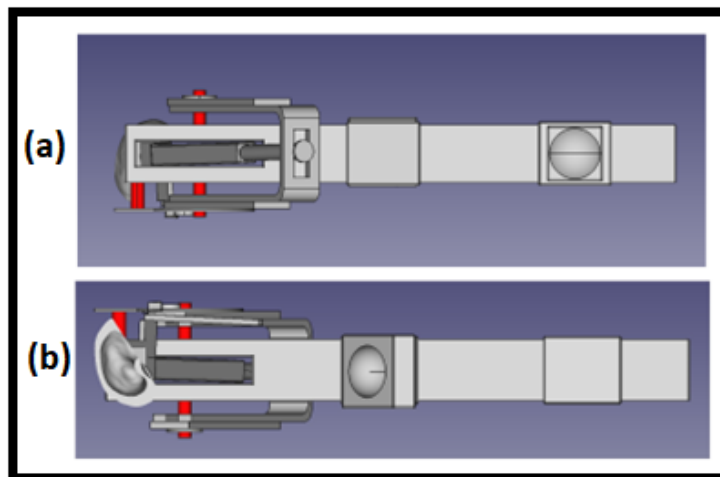
Figure 103: *The system's layout – (a) top view, (b) bottom view.*
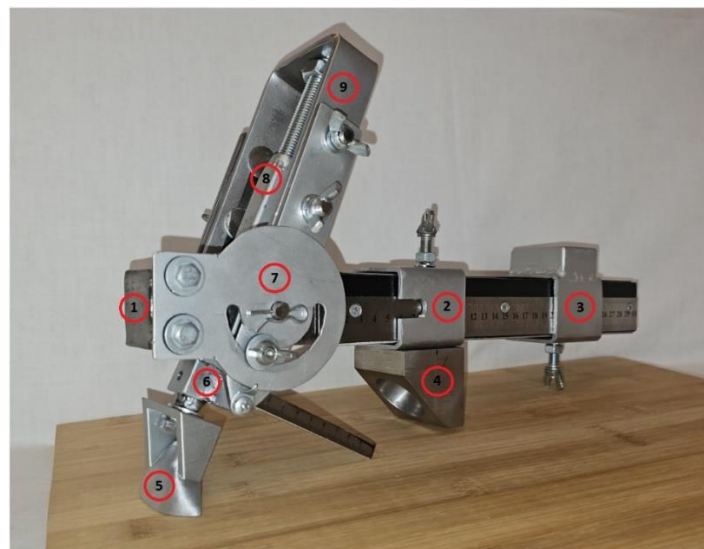
Figure 104: *The second type of setup system that was designed for the experiment.*

The rod (1) is the strong base of the system, where all the components are connected. At the surface of the rod, there is a 30cm ruler to adjust the components' position. (2) is a moveable component, which can move along the axis of the rod adjusting the

position of (4). (3) is also a moveable component that has the ability to move in the same directions as (2). Its distance from the femoral head represents the lever arm of the body weight. On its upper side, a hemispherical point has been created for the mechanical press, so that the contact is made correctly. (4) is a specially designed socket for the artificial femoral heads. The socket has a fixed angle of 18°, so that the joint force is exerted correctly and its position at the vertical axis can also be adjusted by inserting these special square tiles (**Figure 105**) between (2) and (4). (5) is created based on the shape of the great trochanter to fit perfectly. (6) is a ruler that attaches to (8) and is used to measure the lever arm of the abductor's force. After the measurement, it can be removed so it won't bother during any kind of experiment. (7) is a protractor that helps adjust the angle at which the abductor's force is exerted at the great trochanter. (8) is a 1.5cm x 1.5cm rod that adjusts the position of (5) and (6) on the vertical axis. On its bottom and top there have been inserted coupling nuts to allow components (5) and (9) to be attached to it using bolts. (9) is a base where the load cell is placed and secured. It has the ability to extend and shorten its height, thus giving the opportunity to use many different sizes of load cells. The bolt that appears on top of (9), in reality, represents the load cell. The load cell is secured with one bolt at the top of (9) and with a stud bolt (a solid bar with a circular cross-section that is fully threaded) on top of (8).

The entire system, except for components (4), (5), and (7), was constructed using recycled iron objects and hand tools. Component (7) was chosen to be made of aluminum because it was easier to create the elliptic void needed for the rotation and angle adjustment of the abductor's force. Initially, iron was considered for this component, but the lack of special tools and machines made it feasible. Components (4) and (5) have a very unique and complex shape, which is understandable that using conventional tools it was impossible to construct them. **3Ψ Ltd and Akmelogi S.m.p.c.** designed, 3D printed and provided these two components. They are made out of stainless-steel with a small percentage of porosity so as to reduce weight.

After construction, the system components underwent further processing. First, their surfaces were sanded smoothly to remove residues. Then, they were cleansed with a nitro solvent to eliminate any remaining liquids. A special primer for metal surfaces was then applied to improve paint adhesion. The components were painted with an anti-rust paint and finally finished with a metal varnish to protect the paint from environmental factors. For obvious reasons, (4) and (5) did not require further processing after their construction.

Figure 105: *The special square tiles that can be used to adjust the position of (4) at the vertical axis.*

While building the system, a challenge arose in terms of "locking" the components into place. Initially, hex bolts with regular nuts and flat washers were used. However, since the system will be used not only in static but in dynamic load projects too, vibrations will cause loosening, leading to unwanted movement of the components. To eliminate this issue, specific hardware was selected. Lock nuts, which have an in-built mechanism (usually nylon) to prevent loosening by creating friction against the bolt threads, were chosen. Lock washers were also selected; their split and slight twist create a spring-like effect, generating tension that helps prevent the bolt or nut from rotating. In that way, it is certain that the components will remain in the desired place.

All the necessary features have been integrated successfully into this system. That includes the lever arms, the forces, and the angles. At the same time, the system has a very strong, robust structure with excellent control of the movement of its components, resisting any kind of strain and vibration. The extra surface treatment of the parts also gives the system resistance to environmental factors and oxidation. Another significant advantage of this system is its cost-effectiveness. The materials and tools required for its construction are inexpensive, making it an economical choice for various applications. However, its reliability for experimental use is still debatable, because there haven't been any experiments to test its integrity.

Experimental process

The first specimen that was mechanically tested was the intact femur. Component (4) (**Figure 101**) was attached to the great trochanter of the specimen using PMMA to ensure that would remain in place during the experiment. At the same time, the base of the femur was also embedded in PMMA at an angle of 11° (based on **Figure 99**) as shown in the figure below.
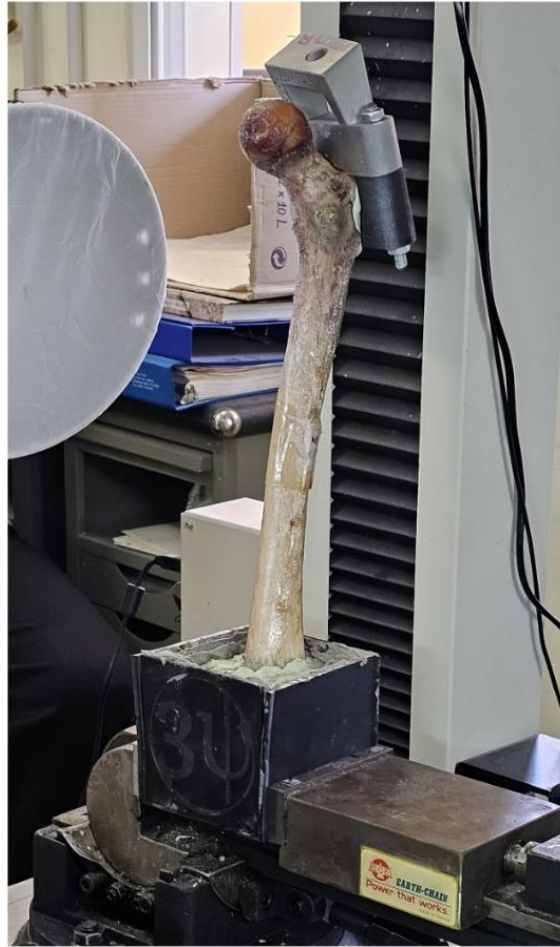
Figure 106: *Attachment of component (4) at the great trochanter and embodiment of the intact femur with PMMA.*

The loading setup was then placed on the femur and the whole system was attached to the press. A preload of 45N was required to stabilize the setup-femur system in place. The load cell was placed at component (3) and connected directly to its recording device to monitor the abductors force. The system was calibrated based on the donor's information, ensuring that the lever arms of the abductor's force and the body force have the correct lengths (lever arm of abductors force 44.5mm and lever arm of body weight's force 69mm), as well as for the angles of the forces. The press was set with the same settings that were used in the test experiment for the evaluation of the makeshift setup (**Table 9**).

The DIC system that was used for this experiment is presented in Figure 107. It uses two cameras to capture the deformations of the femur at two different planes. Specifically, one camera captures the deformations at the horizontal plane while the other at the vertical plane. The DIC system was calibrated using the same process that was described in detail in 4.4. The maximum loads to be applied to the bone are also

determined based on the donor's information. Thus, the maximum values of the body force and the abductor's force are, 800N and 1200N (1.5 x Bodyweight force), respectively.
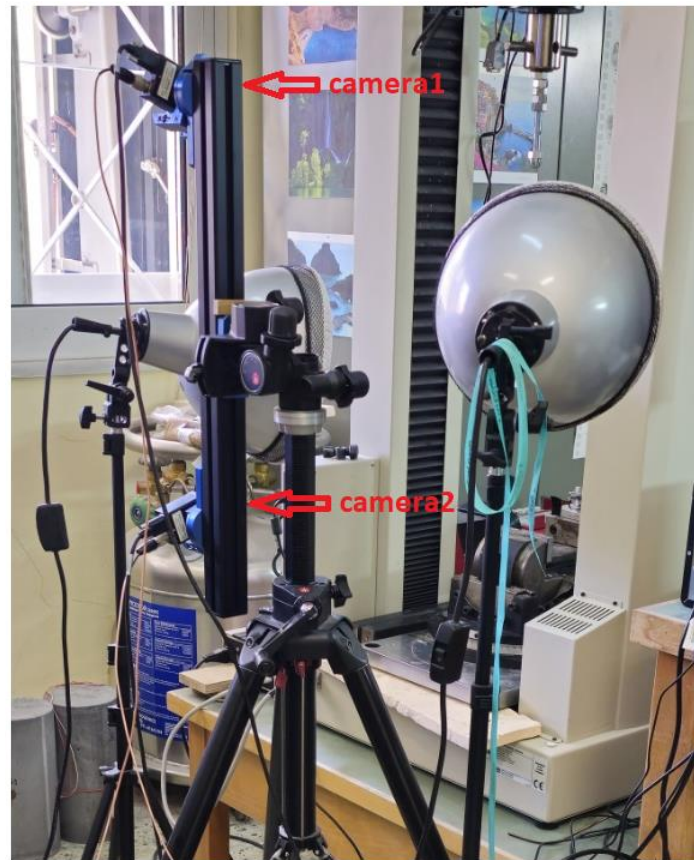
Figure 107: *Setup of the DIC system.*

After preparing and calibrating the experimental setup (**Figure 101**), the specimen was ready for static-compressive forces. In the first attempt, the femur was loaded, reaching a maximum body force of 810N and an abductor's force of 1210N. The femur sustained the maximum load for 3 continuous minutes without exhibiting any damage or cracks. The loading setup demonstrated excellent performance, with all components remaining in place throughout the entire loading period.

The femur was subjected to four additional loading cycles, achieving the desired forces, and both the femur and setup system performed well. Data captured by the Digital Image Correlation (DIC) system was processed using specialized software called "Istra 4D". The table below summarizes the maximum forces achieved and the performance of the system during the five loads. Displacement data obtained from DIC and graphs from the press are presented further below.

Table 10: *Summary of the maximum loads and the performance of the intact femur and loading setup during the experimental procedure.*

	Maximum Body Force	Maximum Abductor's force	Load Retention (3 mins)	Loading setup performance
First attempt	≈810N	≈1210N	Successful	No unwanted displacements of the components
Second attempt	≈807N	≈1207N	Successful	No unwanted displacements of the components
Third attempt	≈810N	≈1210N	Successful	No unwanted displacements of the components
Fourth attempt	≈810N	≈1210N	Successful	No unwanted displacements of the components
Fifth attempt	≈810N	≈1210N	Successful	No unwanted displacements of the components

First Attempt – Intact femur
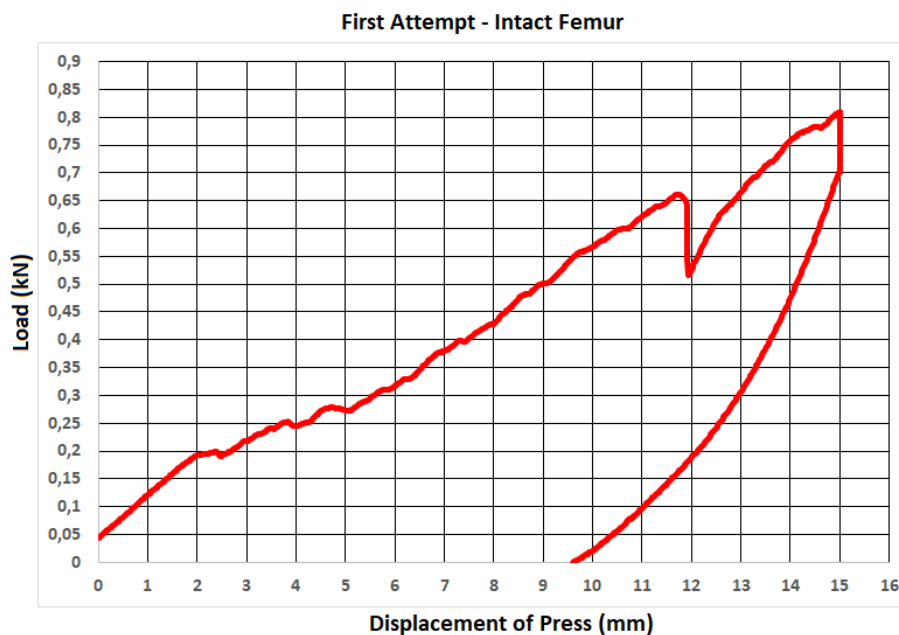
Figure 108: *Development of the load as a function of the vertical displacement of the press – First attempt intact femur.*

Figure 109: *First attempt – Displacements of the femur under static-compressive load on x-axis (a) and on y-axis (b).*

Second attempt – Intact femur

Figure 110: *Development of the load as a function of the vertical displacement of the press – Second attempt intact femur.*

Figure 111: *Second attempt – Displacements of the femur under static-compressive load on x-axis (a) and on y-axis (b).*

Third Attempt – Intact femur

Figure 112: *Development of the load as a function of the vertical displacement of the press – Third attempt intact femur.*

Figure 113: *Third attempt – Displacements of the femur under static-compressive load on x-axis (a) and on y-axis (b).*

Fourth Attempt – Intact Femur

Figure 114: *Development of the load as a function of the vertical displacement of the press – Fourth attempt intact femur.*
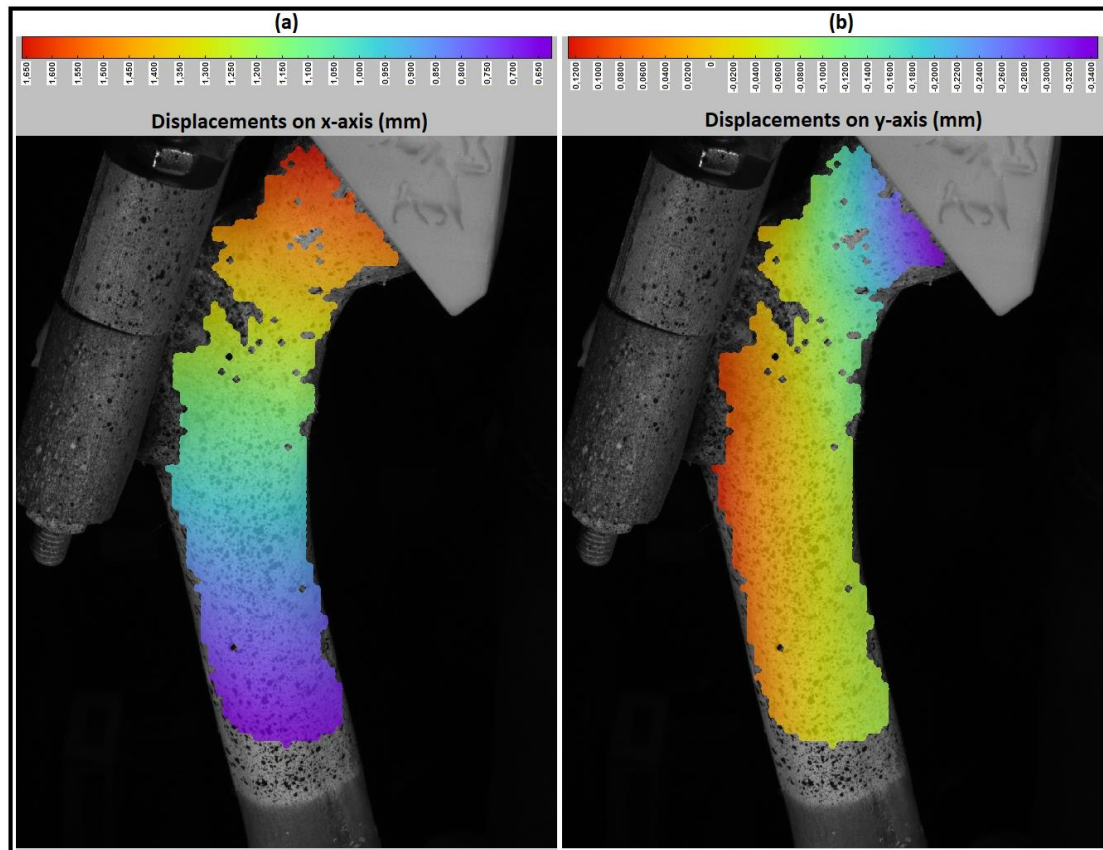
Figure 115: *Fourth attempt – Displacements of the femur under static-compressive load on x-axis (a) and on y-axis (b).*

Fifth Attempt – Intact Femur
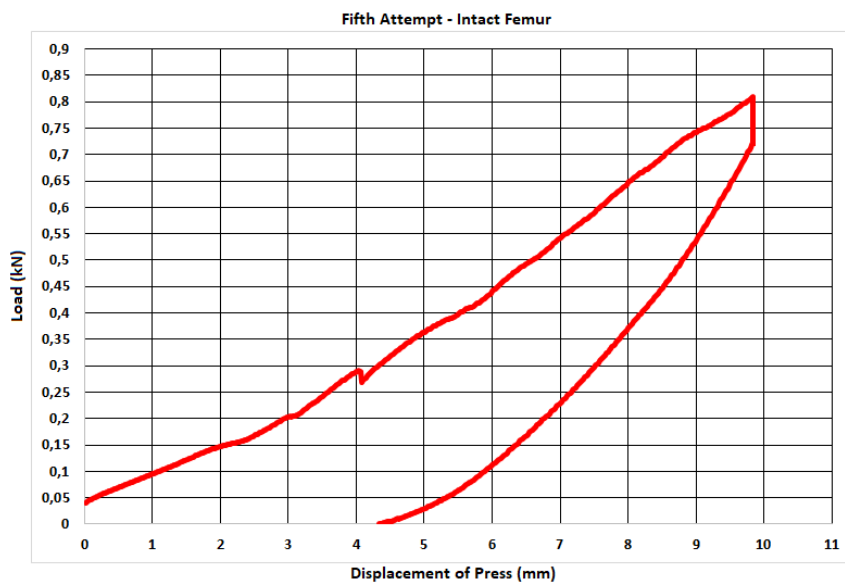
Figure 116: *Development of the load as a function of the vertical displacement of the press – Fifth attempt intact femur.*
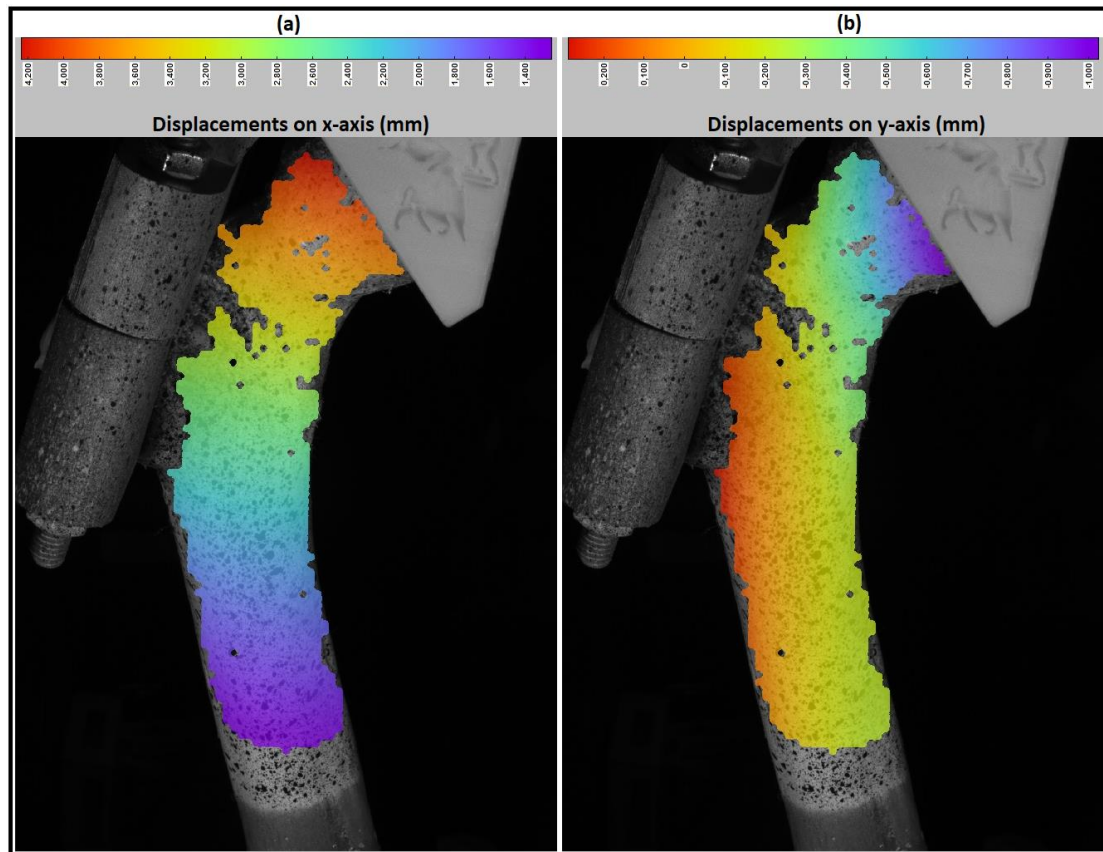
Figure 117: *Fifth attempt – Displacements of the femur under static-compressive load on x-axis (a) and on y-axis (b).*

After the mechanical evaluation of the intact femur, the operated specimen was prepared in the same manner for the experiment. It was adjusted to the loading setup and the press, and the equipment was calibrated again (**Figure 118**). Because this specimen has an implant, the lever arm of the body and abductor's forces changed to 52mm and 33.5mm, respectively.

An unexpected event occurred during the preparation of this specimen. The component placed on the great trochanter was secured with PMMA, as previously mentioned, to ensure it remained in place throughout the experiment. However, due to the rapid polymerization of PMMA and the closed structure of the part being placed, the femur at that point developed a high temperature exceeding 80 degrees Celsius, causing damage to the bone (**Figure 119**). Bone tissue is damaged at temperatures of 50 degrees Celsius and above, a phenomenon known as thermal osteonecrosis [124]. Despite this issue, the experiment continued without further adaptability problems in the experimental setup.
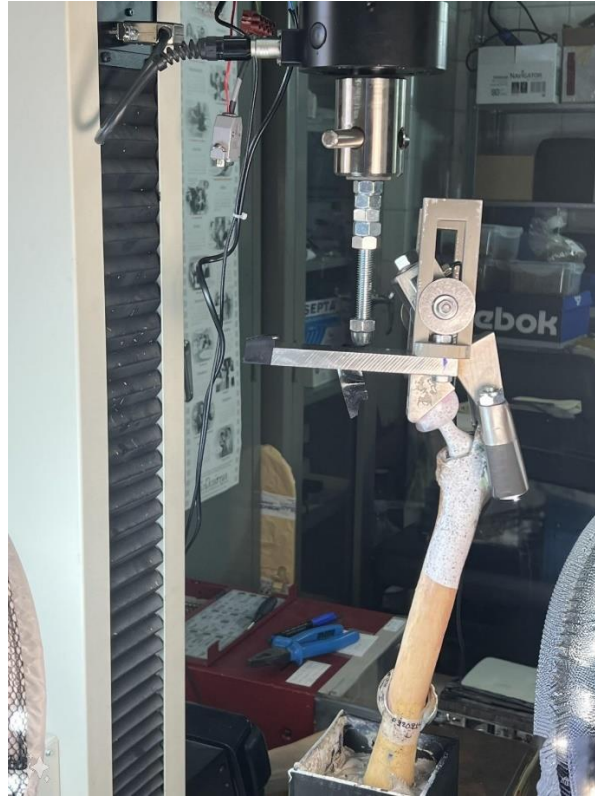
Figure 118: *The adjustment of the operated femur with the femoral stem to the press.*

Figure 119: *This figure presents the damage at the great trochanter done by the excessive temperature that was developed by the polymerization of the PMMA.*

The first two attempts were stopped because the press extension exerting force on the system collided with the load cell. The first attempt stopped at 482N and the second at 500N. To continue the experiment, the load cell was removed, and the specimen was loaded a third time. However, the third attempt was stopped at 385N because the component in the great trochanter came out of position because a small area of the great trochanter was shattered. This was expected due to the previous damage to the greater trochanter. At this point, the experimental procedure was halted, as the implanted stem could no longer adapt to the loading setup. Below is the development of the load on the specimen during the three attempts. Since the maximum load was not reached, the DIC results for the implanted femur cannot be compared with those of the intact femur.
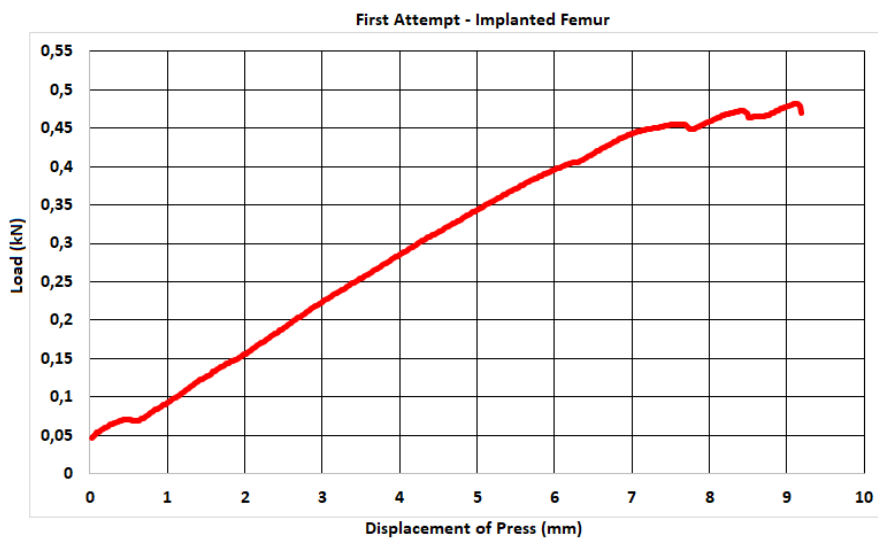
Figure 120: *Development of the load as a function of the vertical displacement of the press – First attempt implanted femur.*
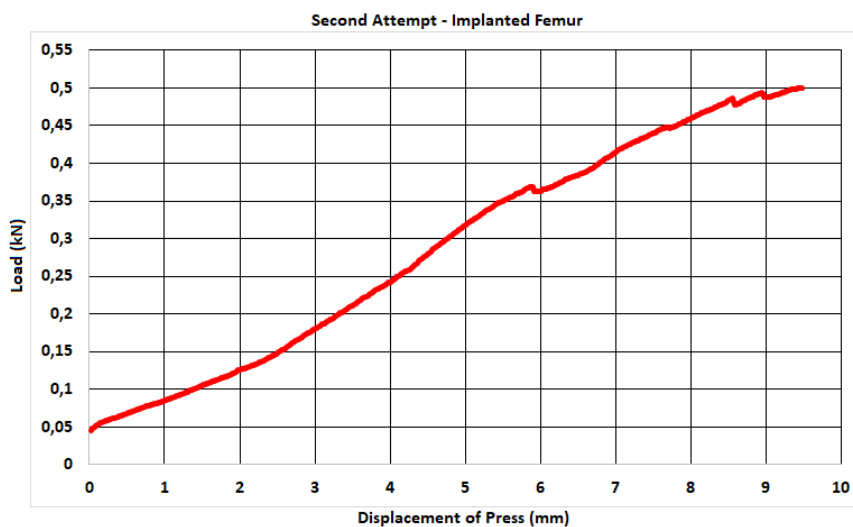
Figure 121: *Development of the load as a function of the vertical displacement of the press – Second attempt implanted femur.*
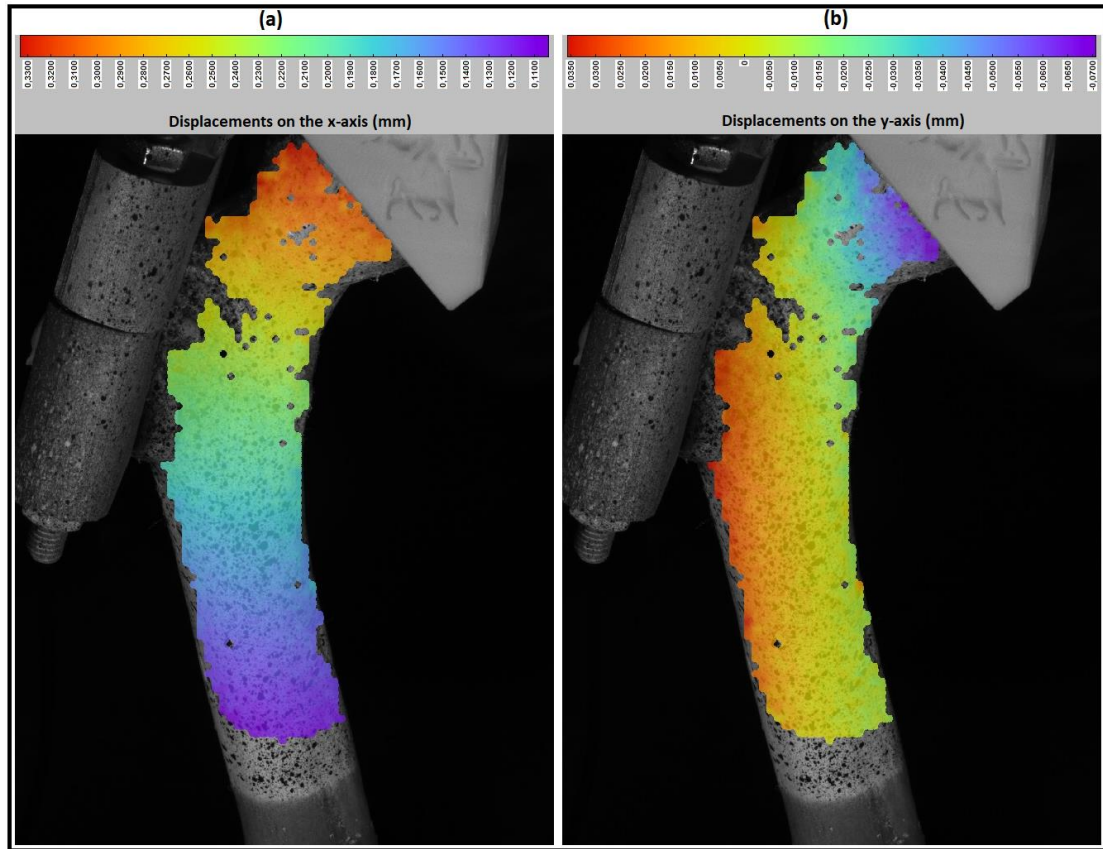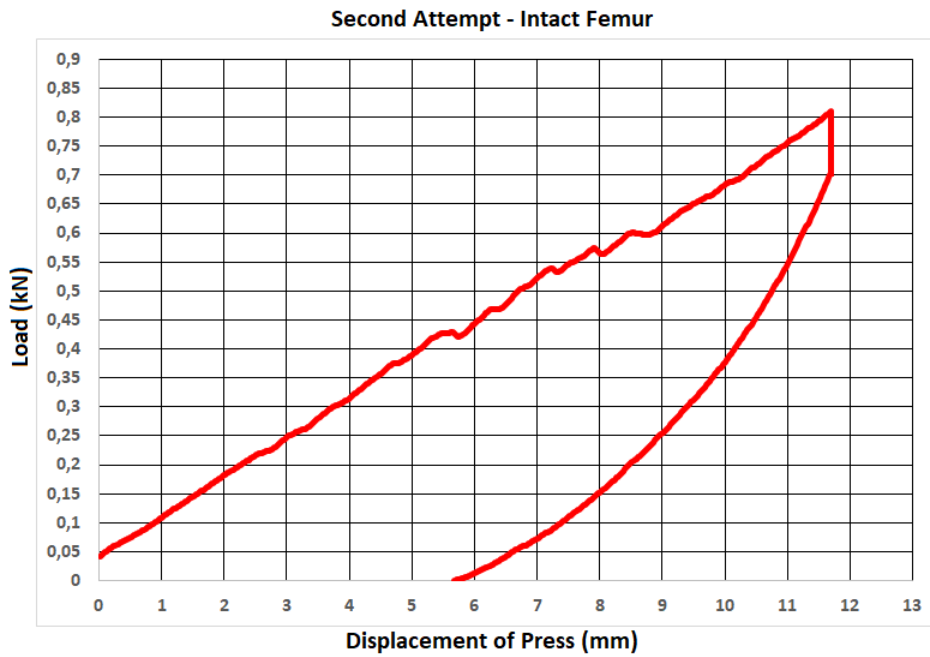
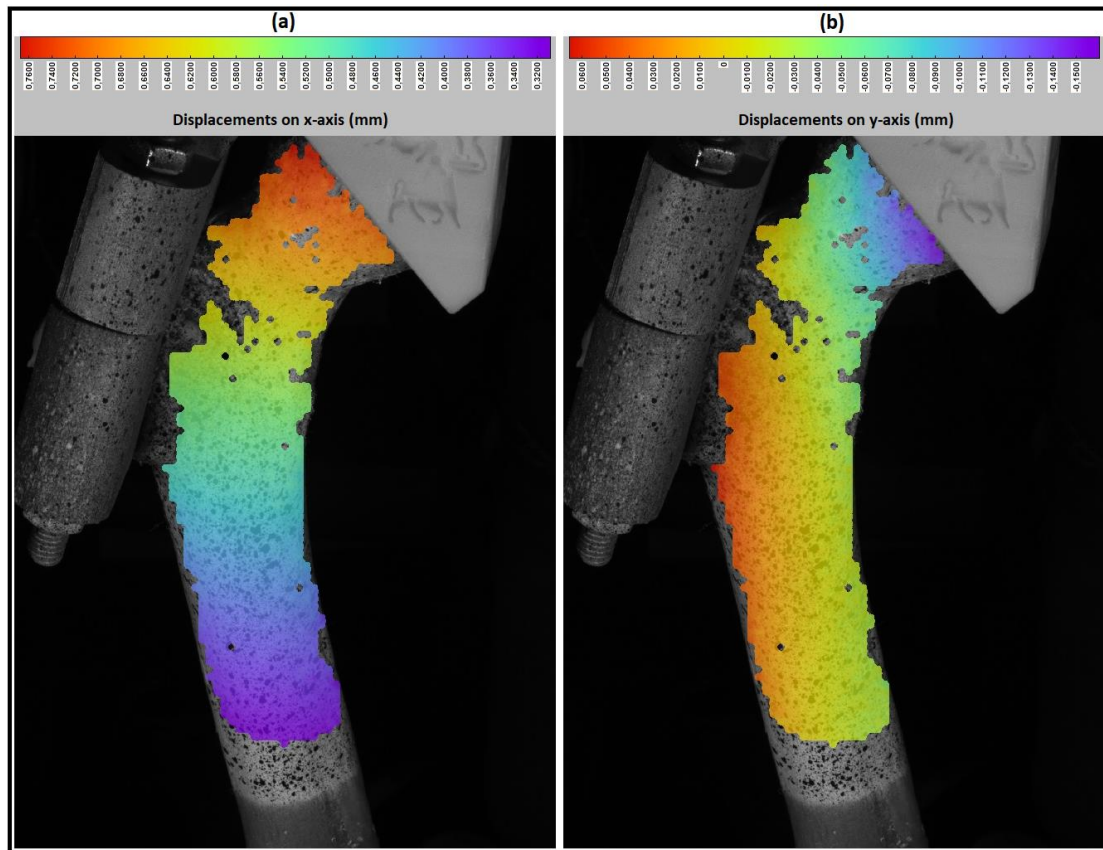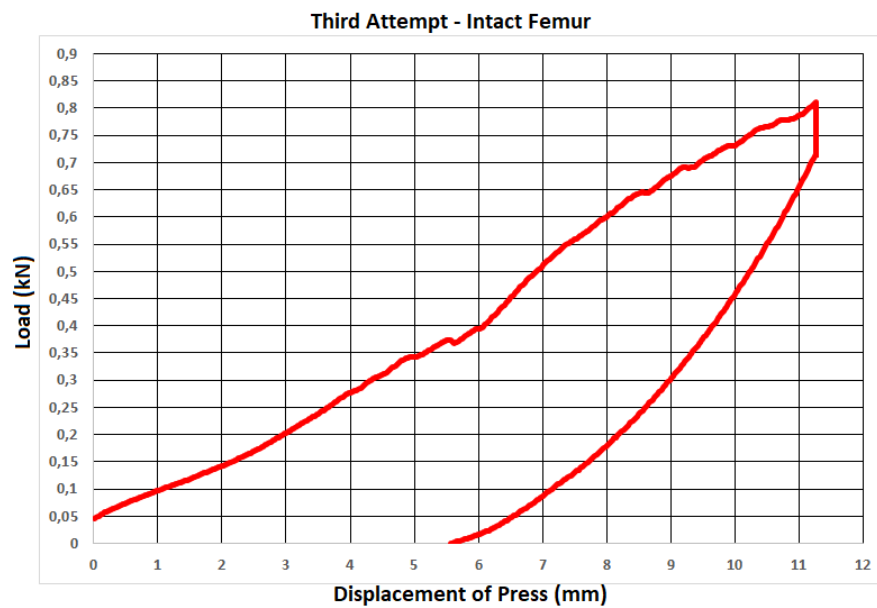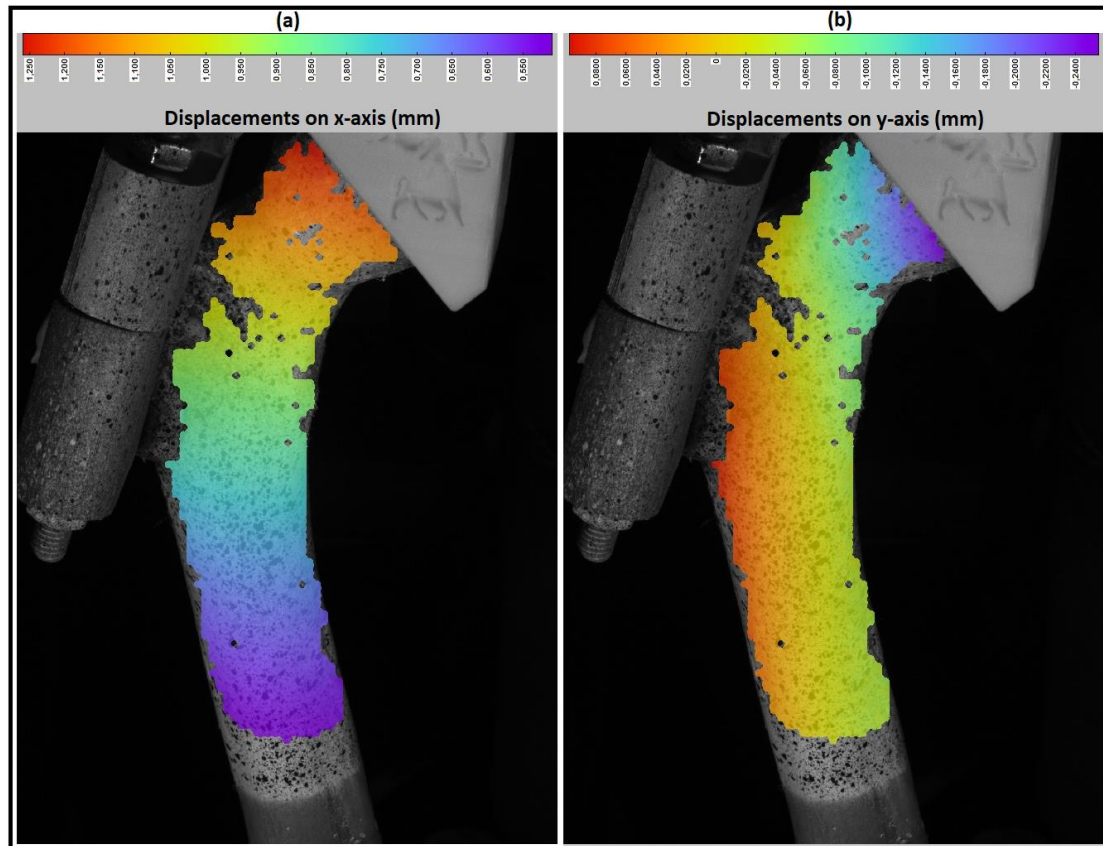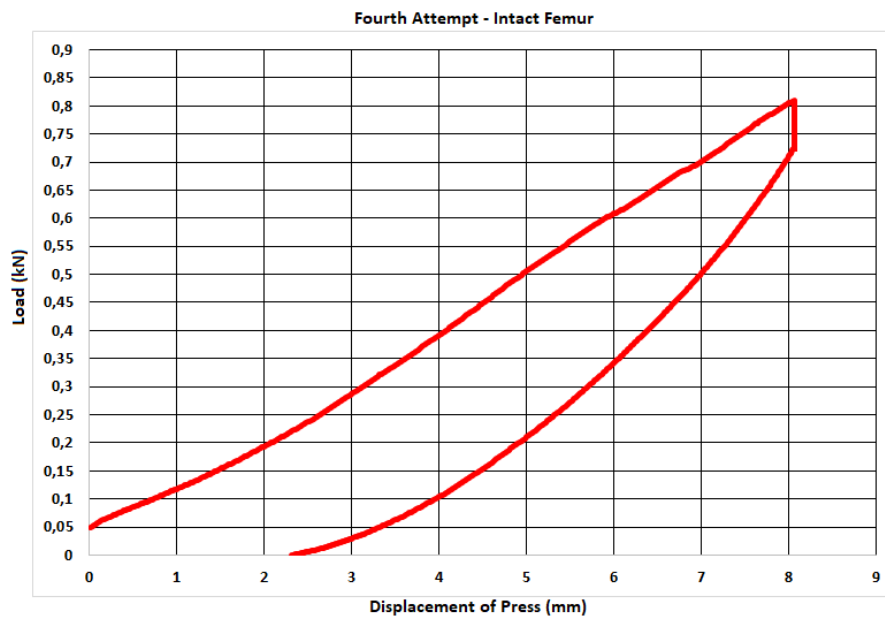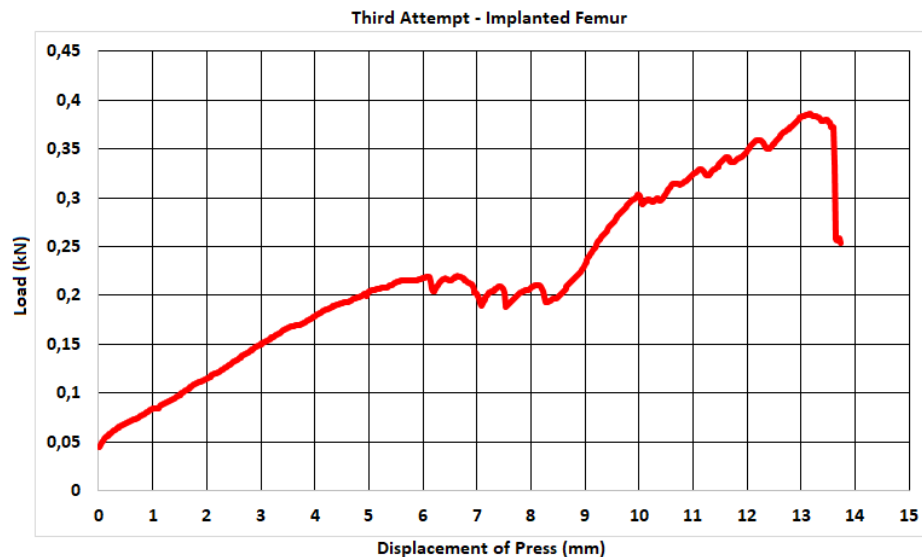**Figure 122**: *Development of the load as a function of the vertical displacement of the press – Third attempt implanted femur.*

For the intact femur, the graphs generated by the press software show an almost linear behavior during the loading phase, which was expected. However, within the same region of the graphs, there are minute, sudden dips. These points are critical because they can indicate significant changes in the material's behavior under load, unwanted displacements of the system's components, or calibration-measurement errors.

Since there were no observable fractures or cracks in the femur during the five attempts, it is debatable whether the material's behavior caused these dips. At the same time, the system performed excellently, with no slippage or misalignment of the components in the testing setup that could cause a temporary reduction in the measured load. Therefore, the most likely cause of these dips is measurement errors, though further investigation is needed to confirm this hypothesis.

The DIC results for the intact femur show that on the x-axis, the highest strain values are concentrated near the top, close to the superior neck where the compressive load is applied. The vertical strains on the y-axis appear to be the highest at the back of the medial diaphysis and under the great trochanter. These regions are expected to have the highest strains because, as the femoral head is subjected to load, the neck experiences more tensile (superior part) and compressive (inferior part) forces on the x-axis, while the medial diaphysis experiences more tensile (back part) and compressive (front part) forces on the y-axis. The same results were presented in the theoretical part of this work (Chapter 2), where other experimental works were

discussed, including a wide range of applications such as cadaver studies, numerical simulations, and composite femurs.

For the implanted femur, the only available data is from the press software, as the DIC results could not provide comparative characteristics with the intact femur, since the load did not reach its maximum value. For the first two attempts, linear behavior was observed until the point the experiment stopped. However, the graph from the third attempt shows a unique behavior with multiple dips. This graph is not linear, which is expected since a small part of the great trochanter was shattered. The micromotions of the great trochanter's component caused the system to lose load bearing capacity while the press continued to apply pressure.

6. CONCLUSION AND DISCUSSION

The present scientific venture involved the evaluation of the mechanical properties of cadaveric specimens by simulating a realistic environment of human joint forces. Working with cadaveric specimens requires tremendous focus, a lot of preparation, and profound knowledge to ensure the experiment's effectiveness and success. To meet these demands, the theoretical part of this work referenced multiple scientific fields that are crucial for its completion.

The historical context of THA in chapter 1, was essential for enriching the understanding of current practices and offering valuable lessons for future advancements. The evolution of contemporary THA was then discussed, highlighting significant technological achievements and techniques, such as additive manufacturing, robots, and extended reality. Engineers and researchers must continue to advance these factors to ensure the ongoing success of THA, especially given the projected increase in THA procedures in the coming years. Without continuous innovation, the implant industry and the medical facilities may struggle to meet future demands.

Understanding hip biomechanics and how strains are distributed in the femur under load was the next critical step in this work. The biomechanical field is directly linked to the success of this experiment; the better this field is understood, the more accurately hip conditions can be simulated. A two-dimensional schematic showing the main forces at the hip on a frontal plane was used to explain the balance of the hip during a single-leg stance. The magnitudes of the body force and the abductor's force are influenced by their lever arms and the angles at which they are exerted on the femur. The construction of the loading setup in the experimental phase was based on this 2D schematic. Although a realistic 3D schematic involves more forces, including contributions from ligaments and other muscles, simplified models have been proven to offer realistic insights into moments and forces [125]. Perhaps as an extension of this work, a more detailed and complex model could be explored for even greater accuracy.

Understanding strain distribution on the femur was also crucial. This part of the research involved reviewing other studies, including cadaver experiments, numerical simulations, and tests on composite femurs. This created a database that served as an evaluation tool for the reliability of the experiment's results.

At the same time, significant attention was given to solids engineering. Understanding the mechanical properties and behavior of biomaterials and bone tissue is a key element of research. The anisotropic nature of bone tissue makes it challenging

to understand its behavior and mechanical properties, which in turn complicates the production of biomaterials for implant construction. The design of implants requires selecting materials with appropriate mechanical properties, such as a low Young's modulus to ensure correct stress distribution and prevent the stress-shielding effect. Modern biomaterials, such as titanium alloys, exhibit excellent mechanical properties and, when combined with additive manufacturing techniques, can produce effective implants with complex shapes. However, implants are still far from replicating bone tissue to a high degree, necessitating ongoing research in biomaterials and implant design and construction.

The theoretical part also analyzed biomechanical sensors and techniques that provide strain distribution and displacement data for the implant-bone system. Some of these tools have been foundational in the biomechanical field for decades, while others have emerged recently with advanced capabilities due to rapid technological development. Digital Image Correlation stands out among these tools, offering superior strain monitoring capabilities compared to other sensors. Its ability to capture even at the smallest points the deformations across multiple planes makes it indispensable in current experiments, which is why it was used in the present work.

All of the above created a foundation on which the experimental procedure was constructed. The experimental phase was divided into two main parts. The first part was a critical step, specifically focused on designing and constructing a mechanical system capable of accurately replicating the forces acting on the hip joint. The more accuracy achieved, the more reliable the experimental results would be. As explained in Chapter 5, the system needed to possess specific features based on the previously presented two-dimensional schematic of the hip joint.

During the first part of the experimental phase, the first system was successfully constructed and tested, incorporating all necessary features, such as the body force, abductor's force, the lever arms of both forces and their respective angles. The system was made from stainless steel and a high-carbon plastic, materials chosen for their excellent mechanical properties, including good mechanical strength, corrosion, and oxidation resistance. These materials ensured that the system could be used in multiple load applications without showing damage or wear, and their cost-effectiveness made the system economical to create.

The system performed excellently during all load tests, with no unwanted movements of its components. A small defect was observed at the component that

attaches to the great trochanter, which led to the shattering of the implanted femur's great trochanter. This issue arose because the component's closed design caused high temperatures during the application of PMMA, resulting in bone damage. To avoid future complications, this component could be redesigned with a more open form or multiple openings to dissipate heat during PMMA polymerization, reducing the risk of bone damage. In addition, a small adjustment to the position of the load cell needs to be considered so that in future experiments will not collapse with the extension of the press, as it happened during the mechanical evaluation of the implanted femur. Despite these two issues, the system proved to be a reliable tool for evaluating the mechanical behavior of cadaver specimens.

The second system created was an extension of the current work and served as a prototype. This system was specifically designed for dynamic load applications. Its large size, robust, and stable structure enable it to sustain massive repetitive loads without deformation or fatigue. The design allowed easy adjustment of magnitudes, such as lever arms and angles, and employed special hardware to "lock" components in the desired positions, ensuring no unwanted movements during dynamic tests. Most components were created using recycled iron objects and hand tools, making the system very economical.

Surface treatment of the components provided resistance to oxidation and protection from environmental factors. However, in its current state, the system requires optimization before it can be used in experiments. Since it was constructed using hand tools, the precise sizes and distances of the components were not entirely accurate achieved. Advanced manufacturing techniques, such as additive manufacturing, should be used to create its components accurately. Additionally, the primary material used was iron, which, while strong, is susceptible to oxidation. Although surface treatments were applied to prevent oxidation, this is only a temporary solution. Friction from the movement of components during system calibration will eventually wear down the protective layers. Therefore, materials resistant to oxidation, such as stainless-steel or titanium alloys, should be used for the system's manufacture.

Moreover, the system's structure is relatively large and heavy, weighing approximately 10kg, which could create stability and adjustment problems. Optimization should focus on reducing the size and weight without compromising mechanical strength and structural robustness.

The second part of the experimental process involved the mechanical testing of the specimens. The intact femur reached the maximum load in all five attempts. As presented in Chapter 5, the press graphs showed the development of the load in the femur as a function of the displacement of the press, displaying a linear behavior, which was expected. The only issue observed in these graphs was sudden dips, which raised concerns. These dips indicate a reduction in load while the press continues to apply pressure, which is unusual. Possible factors, causing this behavior include fragments and cracks in the femur, misalignments, and displacements of the loading setup components, or calibration-measurement errors.

As explained during the experimental phase, there were no observable cracks or fragments on the femur, and the system demonstrated excellent performance without unwanted movements of its components. Without further investigation, the only reasonable cause for these dips appears to be measurement errors caused by noise. The DIC results for the intact femur showed the biggest strain concentration at the medial diaphysis and the femoral neck. Comparing these results with the studies presented in Chapter 2, these findings can be considered reliable. Thus, the specimen was well-prepared, and the system correctly replicated the forces.

For the implanted femur, due to the damage at the great trochanter, the maximum load could not be achieved. However, from the limited data collected from the first two attempts, the implant-bone system exhibited a linear behavior to the intact femur, this is insufficient to evaluate the integrity of the implant fully. Given the limitations inherent in cadaver specimens, it would not be possible to re-evaluate the implanted femur.

These complications and errors should be considered valuable lessons for future studies. Understanding the potential challenges and limitations encountered in this experiment can guide improvements in both experimental design and methodology. Future research should focus on optimizing the loading setups and addressing measurement noise to enhance the accuracy and reliability of the results. Additionally, further investigation into the behavior of implanted femurs under load, considering the damage and constraints observed, will be crucial for advancing the knowledge in this field.

7. REFERENCES

[1]   S. Affatato, "The history of total hip arthroplasty (THA)," in *Perspectives in Total Hip Arthroplasty*, Elsevier, 2014, pp. 3–18. doi: 10.1533/9781782420392.1.3.

[2]   A. Fontalis, J.-A. Epinette, M. Thaler, L. Zagra, V. Khanduja, and F. S. Haddad, "Advances and innovations in total hip arthroplasty," *SICOT-J*, vol. 7, p. 26, 2021, doi: 10.1051/sicotj/2021025.

[3]   K. Markatos *et al.*, "Hallmarks in the History and Development of Total Hip Arthroplasty," *Surg Innov*, vol. 27, no. 6, Art. no. 6, Dec. 2020, doi: 10.1177/1553350620947209.

[4]   S. R. Knight, R. Aujla, and S. P. Biswas, "Total Hip Arthroplasty - over 100 years of operative history," *Orthopedic Reviews*.

[5]   K. A. Ezzet and J. C. McCauley, "Use of Intraoperative X-rays to Optimize Component Position and Leg Length During Total Hip Arthroplasty," *The Journal of Arthroplasty*, vol. 29, no. 3, pp. 580–585, Mar. 2014, doi: 10.1016/j.arth.2013.08.003.

[6]   W. E. Contributors, "What Is a Resection Arthroplasty?," WebMD. Accessed: Apr. 21, 2023. [Online]. Available: https://www.webmd.com/osteoarthritis/resection-arthroplasty

[7]   P. F. Gomez and J. A. Morcuende, "Early Attempts at Hip Arthroplasty," *Iowa Orthop J*, vol. 25, pp. 25–29, 2005.

[8]   R. A. Brand, M. A. Mont, and M. M. Manring, "Biographical Sketch: Themistocles Gluck (1853-1942)," *Clinical Orthopaedics & Related Research*, vol. 469, no. 6, pp. 1525–1527, Jun. 2011, doi: 10.1007/s11999-011-1836-8.

[9]   C. J. Cullingworth, *Charles White ... a Great Provincial Surgeon and Obstetrician of the Eighteenth Century*. Glaisher, 1904.

[10]   J. Van Houcke, V. Khanduja, C. Pattyn, and E. Audenaert, "The History of Biomechanics in Total Hip Arthroplasty," *IJOO*, vol. 51, no. 4, Art. no. 4, Aug. 2017, doi: 10.4103/ortho.IJOrtho_280_17.

[11]   B. M. Wroblewski, "Professor Sir John Charnley (1911-1982)," *Rheumatology*, vol. 41, no. 7, Art. no. 7, Jul. 2002, doi: 10.1093/rheumatology/41.7.824.

[12]   R. A. Brand, "Biographical Sketch: Sir John Charnley MD, 1911–1982," *Clin Orthop Relat Res*, vol. 468, no. 12, Art. no. 12, Dec. 2010, doi: 10.1007/s11999-010-1547-6.

[13]   D. McMinn and J. Daniel, "History and modern concepts in surface replacement," *Proc Inst Mech Eng H*, vol. 220, no. 2, pp. 239–251, Feb. 2006, doi: 10.1243/095441105X68944.

[14]   J. T. Evans, J. P. Evans, R. W. Walker, A. W. Blom, M. R. Whitehouse, and A. Sayers, "How long does a hip replacement last? A systematic review and meta-analysis of case series and national registry reports with more than 15 years of follow-up," *The Lancet*, vol. 393, no. 10172, Art. no. 10172, Feb. 2019, doi: 10.1016/S0140-6736(18)31665-9.

[15]   P. Söderman, H. Malchau, and P. Herberts, "Outcome of Total Hip Replacement," *Clinical Orthopaedics*, no. 390, Art. no. 390, 2001.

[16]   P. Schmitz, B. Gueorguiev, I. Zderic, C. Pfeifer, M. Nerlich, and S. Grechenig, "Primary stability in total hip replacement: A biomechanical investigation," *Medicine*, vol. 96, no. 42, Art. no. 42, Oct. 2017, doi: 10.1097/MD.0000000000008278.

[17]   C. Kenney, S. Dick, J. Lea, J. Liu, and N. A. Ebraheim, "A systematic review of the causes of failure of Revision Total Hip Arthroplasty," *Journal of Orthopaedics*, vol. 16, no. 5, Art. no. 5, Sep. 2019, doi: 10.1016/j.jor.2019.04.011.

[18]   C. J. Dy, K. J. Bozic, T. J. Pan, T. M. Wright, D. E. Padgett, and S. Lyman, "Risk Factors for Early Revision After Total Hip Arthroplasty: Early Revision After THA: Risk Factors," *Arthritis Care & Research*, vol. 66, no. 6, Art. no. 6, Jun. 2014, doi: 10.1002/acr.22240.

[19] H. Matsuoka, H. Nanmo, S. Nojiri, M. Nagao, and Y. Nishizaki, "Projected numbers of knee and hip arthroplasties up to the year 2030 in Japan," *Journal of Orthopaedic Science*, vol. 28, no. 1, pp. 161–166, Jan. 2023, doi: 10.1016/j.jos.2021.09.002.

[20] I. N. Ackerman *et al.*, "The projected burden of primary total knee and hip replacement for osteoarthritis in Australia to the year 2030," *BMC Musculoskelet Disord*, vol. 20, no. 1, p. 90, Dec. 2019, doi: 10.1186/s12891-019-2411-9.

[21] J. J. Callaghan, R. D. Crowninshield, A. S. Greenwald, J. R. Lieberman, A. G. Rosenberg, and D. G. Lewallen, "Symposium: Introducing Technology into Orthopaedic Practice: How Should It Be Done?: *," *JBJS*, vol. 87, no. 5, p. 1146, Dec. 2005, doi: 10.2106/JBJS.E.00116.

[22] J. M. Burnham, F. Meta, V. Lizzio, E. C. Makhni, and K. J. Bozic, "Technology assessment and cost-effectiveness in orthopedics: how to measure outcomes and deliver value in a constantly changing healthcare environment," *Curr Rev Musculoskelet Med*, vol. 10, no. 2, pp. 233–239, Jun. 2017, doi: 10.1007/s12178-017-9407-6.

[23] R. Vaishya, M. M. Scarlat, and K. P. Iyengar, "Will technology drive orthopaedic surgery in the future?," *International Orthopaedics (SICOT)*, vol. 46, no. 7, pp. 1443–1445, Jul. 2022, doi: 10.1007/s00264-022-05454-6.

[24] N. Cevallos, B. Zukotynski, D. Greig, M. Silva, and R. M. Thompson, "The Utility of Virtual Reality in Orthopedic Surgical Training," *Journal of Surgical Education*, vol. 79, no. 6, pp. 1516–1525, Nov. 2022, doi: 10.1016/j.jsurg.2022.06.007.

[25] "Utility of Augmented Reality and Virtual Reality in Spine Surgery: A Systematic Review of the Literature | Elsevier Enhanced Reader." Accessed: Apr. 29, 2023. [Online]. Available: https://reader.elsevier.com/reader/sd/pii/S1878875021011694?token=0BC6D98AE35 7B4FA9272C72E298A3DA82D7868BA097DA3E17BD84BD325062DB44362FEC1AB55D5 BB0118AB9EA3507E68&originRegion=eu-west-1&originCreation=20230429132931

[26] K. B. Trauner, "The Emerging Role of 3D Printing in Arthroplasty and Orthopedics," *The Journal of Arthroplasty*, vol. 33, no. 8, Art. no. 8, Aug. 2018, doi: 10.1016/j.arth.2018.02.033.

[27] P. Tack, J. Victor, P. Gemmel, and L. Annemans, "3D-printing techniques in a medical setting: a systematic literature review," *BioMed Eng OnLine*, vol. 15, no. 1, Art. no. 1, Dec. 2016, doi: 10.1186/s12938-016-0236-4.

[28] A. Fontalis, B. Kayani, J. W. Thompson, R. Plastow, and F. S. Haddad, "Robotic total hip arthroplasty: past, present and future," *Orthopaedics and Trauma*, vol. 36, no. 1, pp. 6–13, Feb. 2022, doi: 10.1016/j.mporth.2021.11.002.

[29] "Company Achievements – Think Surgical." Accessed: May 03, 2023. [Online]. Available: https://thinksurgical.com/about/company-achievements/

[30] P. Kouyoumdjian, J. Mansour, C. Assi, J. Caton, S. Lustig, and R. Coulomb, "Current concepts in robotic total hip arthroplasty," *SICOT-J*, vol. 6, p. 45, 2020, doi: 10.1051/sicotj/2020041.

[31] M. S. Hepinstall, "Robotic Total Hip Arthroplasty," *Orthopedic Clinics of North America*, vol. 45, no. 4, pp. 443–456, Oct. 2014, doi: 10.1016/j.ocl.2014.06.003.

[32] B. Kayani, S. Konan, A. Ayuob, S. Ayyad, and F. S. Haddad, "The current role of robotics in total hip arthroplasty," *EFORT Open Reviews*, vol. 4, no. 11, pp. 618–625, Nov. 2019, doi: 10.1302/2058-5241.4.180088.

[33] "Figure 5 ROBODOC, first FDA approved robot (26). (A) Early ROBODOC…," ResearchGate. Accessed: May 03, 2023. [Online]. Available: https://www.researchgate.net/figure/ROBODOC-first-FDA-approved-robot-26-A-Early-ROBODOC-prototype-B-latest-ROBODOC_fig5_317947879

[34] "Discover a day in the life of a Mako Product Specialist," Stryker Careers Blog. Accessed: May 03, 2023. [Online]. Available: https://www.strykercareersblog.com/post/stryker-spotlight-mako-product-specialists

[35] "TSolution One® – Think Surgical." Accessed: May 03, 2023. [Online]. Available: https://thinksurgical.com/products-and-services/tsolution-one/

[36] J. Moya-Angeler, "Current concepts on osteonecrosis of the femoral head," *WJO*, vol. 6, no. 8, Art. no. 8, 2015, doi: 10.5312/wjo.v6.i8.590.

[37] K. N. Malizos, A. H. Karantanas, S. E. Varitimidis, Z. H. Dailiana, K. Bargiotas, and T. Maris, "Osteonecrosis of the femoral head: Etiology, imaging and treatment," *European Journal of Radiology*, vol. 63, no. 1, Art. no. 1, Jul. 2007, doi: 10.1016/j.ejrad.2007.03.019.

[38] C. G. Zalavras and J. R. Lieberman, "Osteonecrosis of the Femoral Head: Evaluation and Treatment," *Osteonecrosis of the Femoral Head*, vol. 22, no. 7, Art. no. 7, 2014.

[39] P. Kumar, R. K. Sen, S. Aggarwal, and K. Jindal, "Common hip conditions requiring primary total hip arthroplasty and comparison of their post-operative functional outcomes," *J Clin Orthop Trauma*, vol. 11, no. Suppl 2, pp. S192–S195, Mar. 2020, doi: 10.1016/j.jcot.2019.02.009.

[40] D. P. Byrne, K. J. Mulhall, and J. F. Baker, "Anatomy & Biomechanics of the Hip," *TOSMJ*, vol. 4, no. 1, pp. 51–57, Jan. 2010, doi: 10.2174/1874387001004010051.

[41] G. G. Polkowski and J. C. Clohisy, "Hip Biomechanics," *Sports Medicine and Arthroscopy Review*, vol. 18, no. 2, p. 56, Jun. 2010, doi: 10.1097/JSA.0b013e3181dc5774.

[42] Y. Katz and Z. Yosibash, "New insights on the proximal femur biomechanics using Digital Image Correlation," *Journal of Biomechanics*, vol. 101, p. 109599, Mar. 2020, doi: 10.1016/j.jbiomech.2020.109599.

[43] A. Latif Aghili, A. Moazemi Goudarzi, A. Paknahad, M. Imani, and A. Abouei Mehrizi, "Finite Element Analysis of Human Femur by Reverse Engineering Modeling Method," *Indian Journal of Science and Technology*, vol. 8, no. 13, Jul. 2015, doi: 10.17485/ijst/2015/v8i13/47884.

[44] J. Elfar, S. Stanbury, R. M. G. Menorca, and J. D. Reed, "Composite Bone Models in Orthopaedic Surgery Research and Education," *J Am Acad Orthop Surg*, vol. 22, no. 2, pp. 111–120, Feb. 2014, doi: 10.5435/JAAOS-22-02-111.

[45] L. Cristofolini, Viceconti Marco, Cappello Angelo, and Toni Aldo, "MECHANICAL VALIDATION OF WHOLE BONE COMPOSITE FEMUR MODELS".

[46] L Cristofolini, and M Viceconti "Towards the standardization of *in vitro* load transfer investigations of hip prostheses," *The Journal of Strain Analysis for Engineering Design*, vol. 34, no. 1, Art. no. 1, Jan. 1999, doi: 10.1243/0309324991513579.

[47] S. P. Väänänen, S. Amin Yavari, H. Weinans, A. A. Zadpoor, J. S. Jurvelin, and H. Isaksson, "Repeatability of digital image correlation for measurement of surface strains in composite long bones," *Journal of Biomechanics*, vol. 46, no. 11, Art. no. 11, Jul. 2013, doi: 10.1016/j.jbiomech.2013.05.021.

[48] E. F. Morgan, G. U. Unnikrisnan, and A. I. Hussein, "Bone Mechanical Properties in Healthy and Diseased States," *Annual Review of Biomedical Engineering*, vol. 20, no. 1, pp. 119–143, 2018, doi: 10.1146/annurev-bioeng-062117-121139.

[49] D. T. Reilly and A. H. Burstein, "The elastic and ultimate properties of compact bone tissue," *Journal of Biomechanics*, vol. 8, no. 6, pp. 393–405, Jan. 1975, doi: 10.1016/0021-9290(75)90075-5.

[50] M. J. Mirzaali *et al.*, "Mechanical properties of cortical bone and their relationships with age, gender, composition and microindentation properties in the elderly," *Bone*, vol. 93, pp. 196–211, Dec. 2016, doi: 10.1016/j.bone.2015.11.018.

[51] N. J. Hallab and J. J. Jacobs, "Orthopedic Applications," in *Biomaterials Science*, Elsevier, 2013, pp. 841–882. doi: 10.1016/B978-0-08-087780-8.00073-5.

[52] A. S. M. Croitoru, B. A. Pacioga, and C. S. Comsa, "Personalized hip implants manufacturing and testing," *Applied Surface Science*, vol. 417, pp. 256–261, Sep. 2017, doi: 10.1016/j.apsusc.2017.02.185.

[53] J. Vander Sloten, L. Labey, R. Van Audekercke, J. Helsen, and G. Van Der Perre, "The development of a physiological hip prosthesis: the influence of design and materials," *J Mater Sci: Mater Med*, vol. 4, no. 4, Art. no. 4, Jul. 1993, doi: 10.1007/BF00122200.

[54] A. Rohlmann, U. Mössner, G. Bergmann, G. Hees, and R. Kölbel, "Effects of stem design and material properties on stresses in hip endoprostheses," *Journal of Biomedical Engineering*, vol. 9, no. 1, Art. no. 1, Jan. 1987, doi: 10.1016/0141-5425(87)90104-X.

[55] L. C. Zhang, E. C. S. Kiat, and A. Pramanik, "A Briefing on the Manufacture of Hip Joint Prostheses," *AMR*, vol. 76–78, pp. 212–216, Jun. 2009, doi: 10.4028/www.scientific.net/AMR.76-78.212.

[56] M. H. Elahinia, M. Hashemi, M. Tabesh, and S. B. Bhaduri, "Manufacturing and processing of NiTi implants: A review," *Progress in Materials Science*, vol. 57, no. 5, pp. 911–946, Jun. 2012, doi: 10.1016/j.pmatsci.2011.11.001.

[57] "Open Knowledge Wiki - What is Graphite." Accessed: Aug. 25, 2023. [Online]. Available: https://nucleus.iaea.org/sites/graphiteknowledgebase/wiki/Guide_to_Graphite/What%20is%20Graphite.aspx

[58] "Δινορεύματα." Accessed: Aug. 25, 2023. [Online]. Available: https://www.hellenicaworld.com/Science/Physics/gr/Dinorevmata.html

[59] "Vacuum Induction Melting and Casting," AZoM.com. Accessed: Aug. 25, 2023. [Online]. Available: https://www.azom.com/article.aspx?ArticleID=1505

[60] Anandh Subramaniam, "Vacuum Arc Melting Unit." Indian Insitute of Technology Kanpur, Department of Materials Science and Engineering (MSE), Aug. 26, 2023. [Online]. Available: https://home.iitk.ac.in/~anandh/lab/Arc_Melting.pdf

[61] P. Rudling *et al.*, "Impact of manufacturing changes on Zr alloy in-pile performance," 2009.

[62] "Powder Metallurgy | Serena Inc." Accessed: Aug. 27, 2023. [Online]. Available: http://serena.co.in/powdermetallurgy.html

[63] "Technologies and Applications || KOBE STEEL, LTD." Accessed: Aug. 28, 2023. [Online]. Available: //www.kobelco.co.jp/english/products/ip/technology/hip.html

[64] J. R. C. Dizon, A. H. Espera, Q. Chen, and R. C. Advincula, "Mechanical characterization of 3D-printed polymers," *Additive Manufacturing*, vol. 20, pp. 44–67, Mar. 2018, doi: 10.1016/j.addma.2017.12.002.

[65] "Osteoblasts & Osteoclasts: Function, Purpose & Anatomy," Cleveland Clinic. Accessed: Aug. 29, 2023. [Online]. Available: https://my.clevelandclinic.org/health/body/24871-osteoblasts-and-osteoclasts

[66] A. Carter, K. Popowski, K. Cheng, A. Greenbaum, F. S. Ligler, and A. Moatti, "Enhancement of Bone Regeneration Through the Converse Piezoelectric Effect, A Novel Approach for Applying Mechanical Stimulation," *Bioelectricity*, vol. 3, no. 4, Art. no. 4, Dec. 2021, doi: 10.1089/bioe.2021.0019.

[67] C. Yang, J. Ji, Y. Lv, Z. Li, and D. Luo, "Application of Piezoelectric Material and Devices in Bone Regeneration," *Nanomaterials*, vol. 12, no. 24, Art. no. 24, Dec. 2022, doi: 10.3390/nano12244386.

[68] B. I. Oladapo, S. O. Ismail, J. F. Kayode, and O. M. Ikumapayi, "Piezoelectric effects on bone modeling for enhanced sustainability," *Materials Chemistry and Physics*, vol. 305, p. 127960, Sep. 2023, doi: 10.1016/j.matchemphys.2023.127960.

[69] A. A. Al-Tamimi, C. Peach, P. R. Fernandes, A. Cseke, and P. J. D. S. Bartolo, "Topology Optimization to Reduce the Stress Shielding Effect for Orthopedic Applications," *Procedia CIRP*, vol. 65, pp. 202–206, 2017, doi: 10.1016/j.procir.2017.04.032.

[70] A. H. Glassman, J. D. Bobyn, and M. Tanzer, "New Femoral Designs: Do They Influence Stress Shielding?," *Clinical Orthopaedics & Related Research*, vol. 453, pp. 64–74, Dec. 2006, doi: 10.1097/01.blo.0000246541.41951.20.

[71] P. Jana, S. Ray, D. Goldar, N. Kota, S. K. Kar, and S. Roy, "Study of the elastic properties of porous copper fabricated via the lost carbonate sintering process," *Materials Science and Engineering: A*, vol. 836, p. 142713, Mar. 2022, doi: 10.1016/j.msea.2022.142713.

[72] J. C. Wang, "Young's modulus of porous materials," *J Mater Sci*, vol. 19, no. 3, pp. 801–808, Mar. 1984, doi: 10.1007/BF00540451.

[73] K. K. Phani and S. K. Niyogi, "Young's modulus of porous brittle solids," *J Mater Sci*, vol. 22, no. 1, pp. 257–263, Jan. 1987, doi: 10.1007/BF01160581.

[74] B.-K. Jang and H. Matsubara, "Influence of porosity on hardness and Young's modulus of nanoporous EB-PVD TBCs by nanoindentation," *Materials Letters*, vol. 59, no. 27, pp. 3462–3466, Nov. 2005, doi: 10.1016/j.matlet.2005.06.014.

[75] M. Kanayama, B. W. Cunningham, C. J. Haggerty, K. Abumi, K. Kaneda, and P. C. McAfee, "In vitro biomechanical investigation of the stability and stress-shielding effect of lumbar interbody fusion devices," *Journal of Neurosurgery: Spine*, vol. 93, no. 2, Art. no. 2, Oct. 2000, doi: 10.3171/spi.2000.93.2.0259.

[76] "Measuring Strain with Strain Gages." Accessed: Jul. 24, 2023. [Online]. Available: https://www.ni.com/en-us/shop/data-acquisition/sensor-fundamentals/measuring-strain-with-strain-gages.html

[77] "Resistance strain gauge: Principle and Types | Sensors and Transducers | Teachics." Accessed: Jul. 24, 2023. [Online]. Available: https://teachics.org/sensors-and-transducers/strain-gauge-principle-types/

[78] "Understanding the Fundamentals of Strain Gauge," Bestech Australia. Accessed: Jul. 24, 2023. [Online]. Available: https://www.bestech.com.au/strain/understanding-fundamentals-strain-gauge/

[79] https://www.facebook.com/pratik.ambukar.9, "Shear Strain: Definition, Formula, Diagram, Units, Examples." Accessed: Jul. 31, 2023. [Online]. Available: https://mechcontent.com/shear-strain/

[80] "Volumetric Strain: Definition, Formula [GATE Notes]." Accessed: Jul. 31, 2023. [Online]. Available: https://byjusexamprep.com/volumetric-strain-i

[81] J. X. J. Zhang and K. Hoshino, "Chapter 6 - Mechanical transducers: Cantilevers, acoustic wave sensors, and thermal sensors," in *Molecular Sensors and Nanodevices (Second Edition)*, J. X. J. Zhang and K. Hoshino, Eds., in Micro and Nano Technologies. , Academic Press, 2019, pp. 311–412. doi: 10.1016/B978-0-12-814862-4.00006-5.

[82] E. S. Gurdjian and H. R. Lissner, "Mechanism of Head Injury as Studied by the Cathode Ray Oscilloscope Preliminary Report," *Journal of Neurosurgery*, vol. 1, no. 6, pp. 393–399, Nov. 1944, doi: 10.3171/jns.1944.1.6.0393.

[83] L. Grassi and H. Isaksson, "Extracting accurate strain measurements in bone mechanics: A critical review of current methods," *Journal of the Mechanical Behavior of Biomedical Materials*, vol. 50, pp. 43–54, Oct. 2015, doi: 10.1016/j.jmbbm.2015.06.006.

[84] "Strain Gage: Materials." Accessed: Jul. 25, 2023. [Online]. Available: https://www.efunda.com/designstandards/sensors/strain_gages/strain_gage_selection_matl.cfm

[85] "Strain Gauge: What Is It? How Is It Used? Types, Application." Accessed: Jul. 25, 2023. [Online]. Available: https://www.iqsdirectory.com/articles/load-cell/strain-gauge.html

[86] W. Storr, "Resistivity and Electrical Conductivity," Basic Electronics Tutorials. Accessed: Jul. 27, 2023. [Online]. Available: https://www.electronics-tutorials.ws/resistor/resistivity.html

[87] "Resistivity | Definition, Symbol, & Facts | Britannica." Accessed: Jul. 27, 2023. [Online]. Available: https://www.britannica.com/science/resistivity

[88] Ε. ΠΑΠΑΝΑΣΤΑΣΙΟΥ, "ΓΕΦΥΡΑ WHEATSTONE, ΗΛΕΚΤΡΟΝΙΚΟ ΘΕΡΜΟΜΕΤΡΟ." Jul. 27, 2023. [Online]. Available: https://www.med.auth.gr/sites/default/files/news-attachments/wheatstone-_ilthermometro-2021.pdf

[89] "Strain Gauge Measurement - A tutorial." NATIONAL INSTRUMENTS, Jul. 27, 2023. [Online]. Available: http://elektron.pol.lublin.pl/elekp/ap_notes/ni_an078_strain_gauge_meas.pdf

[90] ueidaq, "Temperature Effects in Strain Measurement," Data Acquisition Systems Engineering. Accessed: Jul. 31, 2023. [Online]. Available: https://ueidaq.wordpress.com/2014/01/03/temperature-effects-in-strain-measurement/

[91] "Strain Gauges | Electrical Instrumentation Signals | Electronics Textbook." Accessed: Jul. 28, 2023. [Online]. Available: https://www.allaboutcircuits.com/textbook/direct-current/chpt-9/strain-gauges/

[92] J. L. Schmalzel and D. A. Rauth, "Sensors and signal conditioning," *IEEE Instrumentation & Measurement Magazine*, vol. 8, no. 2, pp. 48–53, Jun. 2005, doi: 10.1109/MIM.2005.1438844.

[93] K. Kalita, N. Das, P. K. Boruah, and U. Sarma, "Design and Uncertainty Evaluation of a Strain Measurement System," *MAPAN*, vol. 31, no. 1, pp. 17–24, Mar. 2016, doi: 10.1007/s12647-015-0155-z.

[94] T. Kugelstadt, "Getting the most out of your instrumentation amplifier design," *Op Amps*, 2005.

[95] K. Charles and C. Lew, "A Designer's Guide to Instrumentation Amplifiers, 3rd Edition".

[96] B. Maundy and S. J. G. Gift, "Strain Gauge Amplifier Circuits," *IEEE Transactions on Instrumentation and Measurement*, vol. 62, no. 4, pp. 693–700, Apr. 2013, doi: 10.1109/TIM.2013.2246904.

[97] E. Al-Fakih, N. A. Abu Osman, and F. R. Mahamd Adikan, "The Use of Fiber Bragg Grating Sensors in Biomechanics and Rehabilitation Applications: The State-of-the-Art and Ongoing Research Topics," *Sensors*, vol. 12, no. 10, Art. no. 10, Sep. 2012, doi: 10.3390/s121012890.

[98] V. Mishra *et al.*, "Fiber Bragg grating sensor for monitoring bone decalcification," *Orthopaedics & Traumatology: Surgery & Research*, vol. 96, no. 6, Art. no. 6, Oct. 2010, doi: 10.1016/j.otsr.2010.04.010.

[99] N. Afsarimanesh, S. C. Mukhopadhyay, and M. Kruger, "Sensing technologies for monitoring of bone-health: A review," *Sensors and Actuators A: Physical*, vol. 274, pp. 165–178, May 2018, doi: 10.1016/j.sna.2018.03.027.

[100] E. and M. S. OFS, "Fiber Optics: Understanding the Basics." Accessed: May 15, 2024. [Online]. Available: https://www.photonics.com/Articles/Fiber_Optics_Understanding_the_Basics/a25151

[101] "FBG Technology | fibre Bragg grating | Smart Fibres." Accessed: May 15, 2024. [Online]. Available: https://www.smartfibres.com/technology

[102] C. S. Baldwin, "Optical Fiber Strain Gages," in *Springer Handbook of Experimental Solid Mechanics*, W. N. Sharpe, Ed., in Springer Handbooks. , Boston, MA: Springer US, 2008, pp. 347–370. doi: 10.1007/978-0-387-30877-7_14.

[103] D. D. Le Pevelen, "Small Molecule X-Ray Crystallography, Theory and Workflow," in *Encyclopedia of Spectroscopy and Spectrometry (Second Edition)*, J. C. Lindon, Ed., Oxford: Academic Press, 2010, pp. 2559–2576. doi: 10.1016/B978-0-12-374413-5.00359-6.

[104] "FBG Principle," FBGS. Accessed: May 16, 2024. [Online]. Available: https://fbgs.com/technology/fbg-principle/

[105] A. Najafzadeh *et al.*, "Application of Fibre Bragg Grating Sensors in Strain Monitoring and Fracture Recovery of Human Femur Bone," *Bioengineering*, vol. 7, no. 3, Art. no. 3, Aug. 2020, doi: 10.3390/bioengineering7030098.

[106] J. Sahota, N. Gupta, and D. Dhawan, "Fiber Bragg grating sensors for monitoring of physical parameters: A comprehensive review," *Optical Engineering*, vol. 59, p. 1, Jun. 2020, doi: 10.1117/1.OE.59.6.060901.

[107] D. Tosi, "Review of Chirped Fiber Bragg Grating (CFBG) Fiber-Optic Sensors and Their Applications," *Sensors*, vol. 18, no. 7, Art. no. 7, Jul. 2018, doi: 10.3390/s18072147.

[108] J. Qi, "A comparison study of the sensing characteristics of FBG and TFBG," *Sensor Review*, vol. 33, no. 1, pp. 68–79, Jan. 2013, doi: 10.1108/02602281311294360.

[109] X. Dong, H. Zhang, B. Liu, and Y. Miao, "Tilted fiber Bragg gratings: Principle and sensing applications," *Photonic Sens*, vol. 1, no. 1, pp. 6–30, Mar. 2011, doi: 10.1007/s13320-010-0016-x.

[110] J. Albert, L. Shao, and C. Caucheteur, "Tilted fiber Bragg grating sensors," *Laser & Photonics Reviews*, vol. 7, no. 1, pp. 83–108, Jan. 2013, doi: 10.1002/lpor.201100039.

[111] S. Deepa and B. Das, "Interrogation techniques for π-phase-shifted fiber Bragg grating sensor: A review," *Sensors and Actuators A: Physical*, vol. 315, p. 112215, Nov. 2020, doi: 10.1016/j.sna.2020.112215.

[112] X. Liu, X. Shu, and H. Cao, "Proposal of a Phase-Shift Fiber Bragg Grating as an Optical Differentiator and an Optical Integrator Simultaneously," *IEEE Photonics J.*, vol. 10, no. 3, pp. 1–7, Jun. 2018, doi: 10.1109/JPHOT.2018.2824661.

[113] J. Chen, B. Liu, and H. Zhang, "Review of fiber Bragg grating sensor technology," *Front. Optoelectron. China*, vol. 4, no. 2, Art. no. 2, Jun. 2011, doi: 10.1007/s12200-011-0130-4.

[114] Y. Zhao and Y. Liao, "Discrimination methods and demodulation techniques for fiber Bragg grating sensors," *Optics and Lasers in Engineering*, vol. 41, no. 1, Art. no. 1, Jan. 2004, doi: 10.1016/S0143-8166(02)00117-3.

[115] W. Petchmaneelumka, W. Koodtalang, and V. Riewruja, "Simple Technique for Linear-Range Extension of Linear Variable Differential Transformer," *IEEE Sensors Journal*, vol. 19, no. 13, Art. no. 13, Jul. 2019, doi: 10.1109/JSEN.2019.2902879.

[116] A. Rerkratn, A. Luangpol, W. Petchmaneelumka, and V. Riewruja, "Position signal detector for linear variable differential transformer," *Energy Reports*, vol. 6, pp. 603–607, Dec. 2020, doi: 10.1016/j.egyr.2020.11.181.

[117] S. Mishra, G. Panda, and D. Das, "A Novel Method of Extending the Linearity Range of Linear Variable Differential Transformer Using Artificial Neural Network," *Instrumentation and Measurement, IEEE Transactions on*, vol. 59, pp. 947–953, May 2010, doi: 10.1109/TIM.2009.2031385.

[118] L. Grassi *et al.*, "Elucidating failure mechanisms in human femurs during a fall to the side using bilateral digital image correlation," *Journal of Biomechanics*, vol. 106, p. 109826, Jun. 2020, doi: 10.1016/j.jbiomech.2020.109826.

[119] J. Karlsson, T. Sjögren, A. Snis, H. Engqvist, and J. Lausmaa, "Digital image correlation analysis of local strain fields on Ti6Al4V manufactured by electron beam melting," *Materials Science and Engineering: A*, vol. 618, pp. 456–461, Nov. 2014, doi: 10.1016/j.msea.2014.09.022.

[120] D. S. Zhang and D. D. Arola, "Applications of digital image correlation to biological tissues," *JBO*, vol. 9, no. 4, Art. no. 4, Jul. 2004, doi: 10.1117/1.1753270.

[121] I. Levadnyi, J. Awrejcewicz, Y. Zhang, and Y. Gu, "Comparison of femur strain under different loading scenarios: Experimental testing," *Proc Inst Mech Eng H*, vol. 235, no. 1, pp. 17–27, Jan. 2021, doi: 10.1177/0954411920951033.

[122] J. Górszczyk, K. Malicki, and T. Zych, "Application of Digital Image Correlation (DIC) Method for Road Material Testing," *Materials*, vol. 12, no. 15, Art. no. 15, Jul. 2019, doi: 10.3390/ma12152349.

[123] Dantec-admin, "New Calibration Target Portfolio for DIC!," Dantec Dynamics | Precision Measurement Systems & Sensors. Accessed: Jun. 22, 2024. [Online]. Available: https://www.dantecdynamics.com/new-calibration-target-portfolio-for-dic/

[124] C. Timon and C. Keady, "Thermal Osteonecrosis Caused by Bone Drilling in Orthopedic Surgery: A Literature Review," *Cureus*, vol. 11, no. 7, p. e5226, doi: 10.7759/cureus.5226.

[125] D. E. Lunn, A. Lampropoulos, and T. D. Stewart, "Basic biomechanics of the hip," *Orthopaedics and Trauma*, vol. 30, no. 3, pp. 239–246, Jun. 2016, doi: 10.1016/j.mporth.2016.04.014.